FZR-415

Katia Parodi

On the feasibility of dose quantification with in-beam PET data in radiotherapy with ^{12}C and proton beams

FZR **Forschungszentrum Rossendorf**

Katia Parodi

On the feasibility of dose quantification with in-beam PET data in radiotherapy with ^{12}C and proton beams

ZZR Forschungszentrum
Rossendorf

On the feasibility of
dose quantification with in-beam PET data
in radiotherapy with ^{12}C and proton beams

Dissertation

zur Erlangung des akademischen Grades

Doctor rerum naturalium

(Dr. rer. nat.)

vorgelegt

der Fakultät Mathematik und Naturwissenschaften

der Technischen Universität Dresden

von

Katia Parodi, Laur. Fisica (Genova, I)

geboren am 9. April 1975

in Genua, Italien

*To my family for their love and support*

Contents

1 Introduction

1.1 Radiation therapy with ion beams

Nowadays in the European Union 58 % of all cancer patients are diagnosed at the stage of a localised primary tumour and about 40 % can be successfully cured by means of surgery (22 %), radiotherapy (12 %) and a combination of the two modalities (6 %) [Gad94, Ver94, Sch96]. However, current local or loco-regional tumour treatments still fail for 18 % of all patients, corresponding to about 280 000 deaths per year in Europe. Since surgery is commonly considered to have reached the limits of its potential for cancer curing, there is a strong clinical demand for improving radiotherapy techniques.

More than 100 years of experience from the first therapeutic trial with X-rays in 1896 [Hal94] have shown that the clinical results of radiotherapy are improved when a high dose of radiation with enhanced biological effectiveness is precisely delivered to the tumour while sparing as much as possible the surrounding healthy tissue and critical organs [Wam89]. Over the last 5 decades external radiotherapy with photon and electron beams has increased the conformity of the dose applied to the tumour by replacing traditional sources like X-ray tubes (energy $\leq 200\,\mathrm{keV}$) or radioactive isotopes e.g. ^{60}Co (average photon energy of $1.25\,\mathrm{MeV}$) by modern high-energy $(4 - 20\,\mathrm{MeV})$ linear accelerators delivering irradiation from several directions. The latest most innovative technique yielding highly conformal dose delivery is intensity modulated radiotherapy (IMRT) [Web01], which uses dynamic geometrical field shaping in order to produce a spatially non-uniform photon flux for each of the several beam portals applied to the patient. Despite these advances and the promising results of the very modern and not yet widely used but rapidly growing IMRT technique, the therapeutic effectiveness of conventional electromagnetic radiation is intrinsically constrained by its physical and radiobiological properties. The unfavourable depth dose profile and the lateral scattering (very pronounced for electrons) restrict the achievable physical selectivity for high precision irradiation of deep-seated tumours growing in close vicinity to critical organs. The low biological effectiveness is inadequate for the treatment of radioresistant tumours, despite all attempts to improve radiation response by means of coadjuvants like hypoxic cell sensitisers or local hyperthermia [Hal94].

Heavy charged particles like protons and heavier ions (^{4}He $- ^{16}$O nuclei) can overcome the limitations of conventional electromagnetic radiation due to the more selective energy deposition in depth (figure 1–1). Ions heavier than protons additionally offer a further reduced lateral scattering and an increased biological effectiveness especially in the region of the sharp dose maximum [Kra00]. The first proposal to use accelerated protons and potentially light ions for therapy because of their superior depth dose distribution dates back to 1946 [Wil46]. However, it took a rather long time to see ion therapy applied in a hospital environment. Most of the therapy units were based on nuclear physics accelerators, like the pioneering and no more active one at Lawrence Berkeley Laboratory (LBL), USA, where proton and heavier ion treatment was started in 1954 (p), 1957 (He) and 1975 (Ar, Si, Ne) [Tob58, Chu93, Cast94], as well as the Harvard Cyclotron Laboratory (HCL), USA, which has the longest and most extensive experience in proton therapy since 1961 [Sis01]. The first dedicated hospital-based facilities have been the Loma Linda University Medical Center (LLUMC), USA, operating proton therapy since 1990 [Cou94], and the Heavy Ion Medical Accelerator in Chiba (HIMAC), Japan, which took up heavy-ion treatment in 1994 after the shutdown of the LBL accelerator in 1993 [Kan99] and replaced the Berkeley neon ions by carbon ions, which seem to offer an optimal compromise between physical selectivity and enhanced biological effectiveness [Bla94]. Since then new proposals and facilities have been fast growing worldwide [Sis01], especially in Japan [Yam01]. However, due to the higher complexity and costs of heavy ion therapy, they have been mostly addressed to proton therapy, which still offers better physical selectivity but not superior biological effectiveness than conventional

1
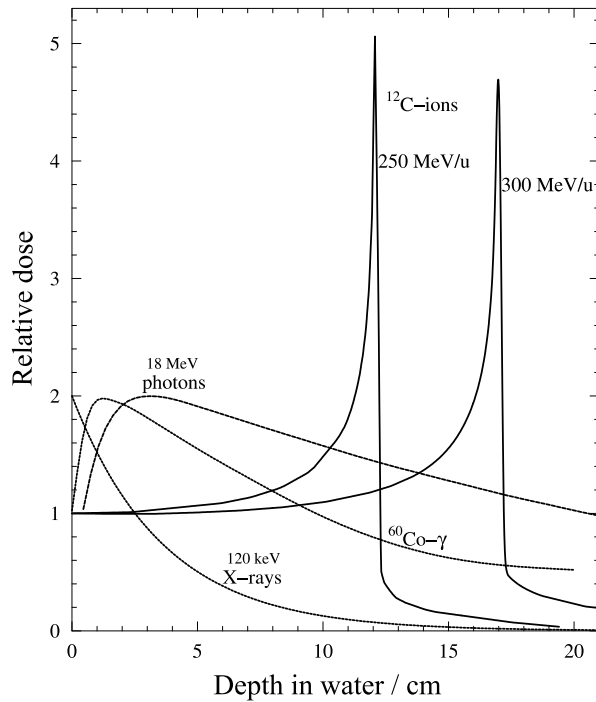
Figure 1–1: *Comparison of dose depth profiles of photons from different radiation sources with carbon ions in water [Kra00]. Variation of the ion energy allows the sharp dose maximum to be precisely located within the tumour.*

radiation [Lin95]. Moreover, the principles of the beam delivery in clinical use at all the hospital-based ion therapy centres are based upon highly reliable but not optimal passive devices (e.g. scattering foils, absorbers, collimators and boli) for shaping the beam and conforming the irradiation to the target volume. An improved tumour-conformity by shaping the beam via magnetic deflection has been only partially realised by means of the spot scanning technique at the experimental proton therapy facility at the Paul Scherrer Institute (PSI), Switzerland [Ped95]. Hence, the full potential of ion therapy has not been yet completely exploited.

The German pilot project of an experimental carbon ion therapy unit running at the Gesellschaft für Schwerionenforschung Darmstadt (GSI) since December 1997 [Cre01a] represents the worldwide first and still unique attempt to fully exploit the heavy ion advantages and demonstrate the safe and routine clinical application of novel techniques. The three most advanced innovations are: (*i*) three-dimensional (3D) conformal beam delivery based on 2D intensity controlled raster scanning in combination with active energy variation from the accelerator [Hab93], (*ii*) radiobiologically oriented inverse treatment planning [Krä00a, Krä00b] and (*iii*) in-situ therapy monitoring by means of positron emission tomography (PET) [Eng99a]. Supported by the promising clinical results never observed before [Deb00], the participating institutions of the GSI pilot project (GSI Darmstadt, German Cancer Research Centre Heidelberg – DKFZ, Radiological University Clinic Heidelberg and Research Centre Rossendorf – FZR) have made a proposal for a hospital-based ion beam facility to be built in Heidelberg, Germany [Gro98]. This centre will deliver particles from protons up to oxygen ions in order to investigate the clinical impact of different ion beam modalities with a large number of patients. On the basis of the GSI experience the Heidelberg project represents also a model for the other five dedicated ion beam facilities proposed in Austria, France, Italy, Spain and Sweden, according to the ENLIGHT (European Network for Research in Light Ion Therapy) coordination activity recently promoted by the participating countries together with ESTRO (European Society for Therapeutic Radiology and Oncology) and CERN (Conseil Européen pour la Recherche Nucléaire). The presented work contributes

to the GSI and Heidelberg projects and addresses the problem of local dose quantification from PET data as well as the possible extension of in-beam PET monitoring to other projectiles than carbon ions, starting with the lightest: the protons.

1.2   Monitoring of ion beam therapy by positron emission tomography (PET)

The higher physical selectivity of ion therapy demands higher precision in the monitoring of the applied treatment, especially in delicate clinical situations. The complete stopping of the ions in the patient prevents the application of electronic portal imaging methods used in conventional radiotherapy [Ant02]. The potential benefit from the favourable dose depth profile (figure 1–1) requires accurate estimation of the ion range in the inhomogeneous patient tissue which determines the position of the dose peak. Slight errors may result in severe underdosage of the tumour volume and overdosage of the surrounding critical structures. The treatment planning algorithms rely on calibrations of X-ray computerised tomography (CT) data leading to $1\% - 3\%$ uncertainties in range calculations [Che79, Scha98, Jäk01a]. During fractionated therapy additional unpredictable range deviations can occur because of minor inaccuracies in the positioning of the patient or local anatomical changes with respect to the information of the planning X-ray CT, typically acquired several days before starting the therapy. Despite the introduction of safety margins around the target volume allowing for range uncertainties [Che79, Jäk01b], tools for the visualisation of the particle distribution within the patient during the irradiation are strongly desirable. Presently PET is the only technically feasible method for this purpose.

For heavy ions the application of positron emission imaging to measure the end-of-range of a β^+-radioactive beam (e.g. ^{19}Ne) injected to the patient in a low-dose exposure prior to the therapeutic irradiation with the stable isotope (e.g. ^{20}Ne) was proposed in Berkeley at the end of the 1970s [Tob77]. Using this approach a very accurate ($< 1\,\mathrm{mm}$) range verification is obtainable due to the strong similarity in the penetration properties of the radioactive and stable ion beam. For this reason a planar coincidence γ-ray camera for 2D imaging was constructed and installed directly at the treatment site at LBL [Lla84]. Despite the first promising tests, the system has been never used in clinical routine because of the too high detector activation probably caused by secondary particles produced in the passive beam shaping devices [Lla88]. Based on this experience at HIMAC a commercial PET scanner was chosen in order to monitor off-line (i.e. at a remote diagnostic site) the "autoactivation" [Tob71] of the stable therapeutic ^{12}C beam after the treatment [Tom94]. Due to the reaction cross sections and the time interval of about 5 min between the irradiation end and the PET scan almost only ^{11}C nuclei produced in projectile and target fragmentation reactions are imaged [Tom97]. Range information is deduced from the pronounced activity peak formed by the ^{11}C projectile fragments stopping shortly before the end point of the primary ^{12}C ions [Tom94]. At GSI the first and still unique tomographic in-beam positron camera was realised by FZR [Paw96, Paw97]. The limited angle double head system employing commercial detector components allows to monitor the dose application simultaneously to the ^{12}C ion tumour irradiation [Eng99b]. The 3D imaging capability fulfills the requirement to verify not only the ion range (deduced from the ^{11}C projectile fragments) but also the extremely conformal lateral dose deposition (mainly deduced from the target fragments) achieved by the novel raster scan system. The on-line solution avoids to lose the significant β^+-activity contribution from short-lived emitters (mainly ^{15}O and ^{10}C) as well as to introduce possible changes of the patient position during the transport to a remote PET scanner. Recently an in-beam planar positron camera has been developed and installed at the new secondary beam course of HIMAC in order to check the range of a low-intensity ^{11}C pencil-like beam delivered to the patient before applying the entire treatment with the same radioactive ions [Kana02]. However, this 2D imaging system resembling the LBL approach will be combined with an

off-line commercial PET scanner for volumetric acquisition [Kana02].

For protons the applicability of PET techniques to range control and therapy monitoring is more challenging, due to the lack of projectile fragmentation. Similar considerations apply also to light ions with $Z < 6$ (He, Li, Be, B) which produce no or only insufficient amounts of β^+-radioactive projectile fragments. Pioneering and very preliminary investigations on the potential of 2D on-line imaging of β^+-emitting target fragments (mainly ^{11}C, ^{15}O and ^{10}C) induced by proton irradiation of phantoms and animals were carried out in Brookhaven at the end of the 1970s [Ben75, Ben78]. Starting from the beginning of the 1990s the topic was again addressed in preliminary phantom experiments using an on-line two-dimensional array of scintillating detectors of low spatial resolution operated in coincidence as well as a commercial off-line PET system [Lit93, Lit99]. In the same years simulation studies [Del94] as well as off-line PET measurements after proton irradiation of phantoms [Paa93, Oel96] and even of one patient [Vyn93] were done by various groups. Despite the common agreement on the potential usefulness of PET imaging for proton therapy monitoring, no definitive conclusion on the clinical feasibility and effectiveness was drawn. The lack of activation in the few last millimetres of penetration due to the energy threshold of about $15 - 20$ MeV for the proton induced nuclear reactions as well as the poor spatial correlation between β^+-activity and dose depth profile were recognised as a nontrivial complication for the extraction of range information and dose localisation [Oel96]. Nowadays PET has not yet been exploited in clinical routine for quality assurance of proton therapy. Alternative approaches using radiographic imaging of high-energy transmitted protons [Mof75, Han81] for indirect range verification prior to the therapeutic irradiation have been explored and are currently under clinical development at PSI [Schn95]. However, on-line PET techniques still offer the unique and very appealing advantage of direct verification of the applied treatment without any additional radiation exposure of the patient beyond the therapeutic dose.

1.3 Aim and outline of the thesis

This thesis contributes to the three topics listed in the following:
- dose quantification from in-beam PET data,
- random coincidences during in-beam PET data acquisition,
- applicability of in-beam PET to the monitoring of proton therapy.

They aim at the further development and improvement of the in-beam PET method, already in clinical use for quality assurance of carbon ion tumour therapy at the experimental treatment unit at GSI Darmstadt, and they also address the preparation of the equipment for the planned dedicated ion beam cancer therapy facility at Heidelberg.

The first issue responds to the main medical demand on quantification of local dose deviations in case of detection of discrepancies between planned and applied treatment by means of PET, as already observed during the clinical experience of in-beam PET monitoring of carbon ion therapy at GSI. The developed approach for a PET guided dose quantification is however limited in feasibility and accuracy by the technical capabilities of the in-beam positron camera currently in use at GSI. The increase of counting statistics represents a critical issue for this problem. Hence, the second topic deals with basic investigations on the physical reason for the high in-beam noise significantly reducing the amount of valuable events recorded by the positron camera simultaneously to the dose application. This understanding is in fact the necessary basis for an improved and dedicated data acquisition scheme for the novel tomographic in-beam PET scanner to be developed and installed at the planned ion beam facility of Heidelberg [Cre01b]. This next generation in-beam positron camera is primarily intended for the quality assurance of carbon ion therapy as a continuation of the GSI activity. However, beams of protons, ^{4}He (or ^{3}He) and ^{16}O nuclei will be delivered to the same

treatment site. Therefore, this work has also initiated the investigation on the possible extension of PET imaging to these projectiles, starting from the protons as the lightest and most thoroughly investigated ion relevant for therapy. This latter topic can have a more general impact due to the larger number of patients treated with protons ($\simeq 30\,000$) than with heavier ions ($\simeq 3\,500$) worldwide [Sis01]. With respect to the former investigations of previous groups, more definitive conclusions on the clinical feasibility and usefulness of PET monitoring in proton therapy are sought on the basis of the clinical experience in the PET control of carbon ion therapy at GSI as well as the experimental availability of the unique 3D in-beam PET scanner installed there.

The thesis is organised as follows. The second chapter reviews the physical rationale of ion therapy and briefly describes the carbon ion therapy pilot project at GSI Darmstadt, with more emphasis on the clinical implementation and results of in-beam PET monitoring. The third chapter shows the implemented solution for local dose quantification from in-beam PET data acquired at GSI and its clinical impact. The fourth chapter addresses the problem of random coincidences during in-beam PET acquisition and presents the experimental evidence for the failure of standard random correction techniques due to the typical microstructure of the beam extracted from a synchrotron. Chapter 5 contains the promising simulation study and comprehensive phantom experiments carried out at GSI which support a favourable application of in-beam PET to the quality assurance of proton therapy. The conclusions and outlook are summarised and discussed in the last chapter.

2 Tumour therapy with ion beams

2.1 The physical basis of ion beam therapy

The goal of radiotherapy with external beams is to deliver a dose distribution precisely localised in the tumour volume and with sufficient biological effectiveness in order to inactivate the tumour cells, whereas sparing as much as possible the surrounding healthy tissue and critical structures as well as the entrance skin.

As already pointed out in the original proposal of R. R. Wilson [Wil46], the main argument for particle therapy is the superior physical selectivity due to the relatively low energy deposition, i.e. dose, in the entrance channel (*plateau*) and a steep increase and fall-off towards the end of the ion path. The resulting sharp and narrow – few millimetres wide – maximum, well known as Bragg-peak in memorial of W. H. Bragg [Brag04], can be accurately adjusted in depth by proper selection of the ion energy. This allows to concentrate a higher dose in a deep-seated tumour and keep at the same time the radiation burden to the healthy tissue in front of and beyond the tumour lower than it would be possible in conventional radiotherapy with photons and electrons. Hence, the characteristic Bragg-curve is also referred to as *inverse* dose depth profile in contrast to the energy deposition of conventional photon radiation, having a maximum close ($\leq 3\,\mathrm{cm}$ in water) to the entrance followed by an exponential decay (figure 1–1). Besides the favourable depth properties, the dose delivered by ions is well confined in space also in the lateral dimension due to the low angular scattering which decreases with increasing ion charge and mass number [Lin95]. However, in most practical clinical cases extended tumour volumes demand the very well localised dose distribution of mono-energetic pencil-like (i.e. of small cross section and low divergence) ion beams to be widened in both longitudinal and lateral direction. The longitudinal modification is accomplished by a proper superimposition of several Bragg-peaks of different depth, i.e., ion energy (figure 2–1) obtained either via passive energy degraders or active energy variation from the accelerator. A lateral spread of the dose distribution is achieved either by broadening the transverse beam profile by means of scattering systems or by exploiting lateral magnetic deflection of
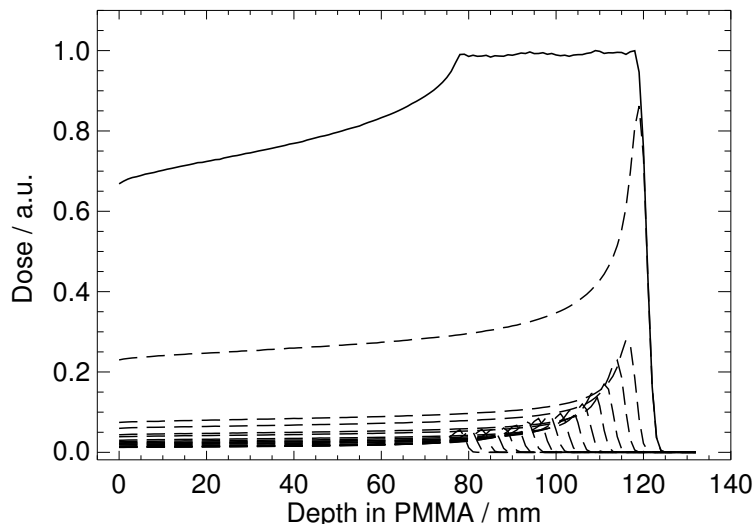
Figure 2–1: *One-dimensional spread-out Bragg-peak (solid line) calculated on the basis of the FLUKA [Fas01a, Fas01b] simulation code by stopping 17 pencil-like proton beams of different energies and intensities (dashed lines) in organic plastic.*

well-focussed pencil-like beams [Chu93]. From figure 2–1 it is evident that the overlap of several Bragg-peaks leads to a reduction of the peak to plateau dose ratio with respect to the single mono-energetic case. However, the resulting dose depth distribution well known as "spread-out Bragg-peak" (SOBP) is still by far better than that for conventional radiation. Moreover, the entrance dose can be reduced further without changing the tumour dose by exploiting multifield irradiation techniques (i.e. delivering several portals from different directions).

In addition to the excellent physical properties, ions heavier than protons exhibit also an increased biological effectiveness towards the end of their path in comparison to reference radiation, mostly $250\,\mathrm{kV_p}$ X-rays or ^{60}Co γ-rays. The reason is the higher ionisation density at the microscopic scale along the individual heavy ion tracks in the Bragg-peak region [Kra97]. At the cellular level this results in the production of clustered and complex DNA (deoxyribonucleic acid) damages more difficult to repair than those due to an exposure to sparsely ionising radiation (e.g. photon and electrons). Furthermore, the lethal cell damages induced by high Z ions are mainly due to direct ionisation processes rather than mediated by radical production. This leads to an almost unchanged radiation response under oxic and anoxic conditions [Alp98], which makes heavy ions more effective in the treatment of radioresistant hypoxic tumours which do not respond strong enough to conventional radiation [Lin95]. All these radiobiological properties can be exploited in order to enhance the radiation damage selectively in the target volume when using the appropriate ion type. In particular, carbon ions seem to offer the greatest ratio of tumour to entrance biological effectiveness [Bla94, Kra00] in combination with a high physical precision. However, according to the aim of this work only the relevant electromagnetic and nuclear interactions underlying the physical properties of therapeutic ion beams will be described. In fact, despite the initial proposals to use positron emission imaging also for studying metabolic and perfusion processes of radioactive isotopes injected in the patient [Lla84], the clinically implemented PET monitoring of heavy ion therapy has been limited to the control of the primary particle range and the localisation of the delivered dose with respect to the treatment plan. Hence, radiobiological issues and functional information on the tumour response to the therapy have not been yet accessed by the non-conventional application of PET techniques to quality assurance of heavy ion therapy. The same is expected for the extension of PET monitoring to proton therapy, where radiobiological considerations are not yet taken into clinical account. Furthermore, recent investigations have shown an increase of the biological effectiveness of protons only for energies lower than $1\,\mathrm{MeV}$ [Bel89], which is well below the energy thresholds for the production of positron emitters to be imaged by PET.

2.1.1   The stopping of ions in matter

In the energy interval of clinical relevance ranging from about $70-500\,A\mathrm{MeV}$ (A – mass number) initial kinetic energy down to rest, ions lose and transfer most of their energy to the traversed medium in Coulomb inelastic collisions with atomic electrons. The rate of average energy loss per unit path length is known as electronic stopping power and is well described above about $1\,A\mathrm{MeV}$ by the Bethe-Bloch formula [Bet30, Blo33]:

$$-\frac{\mathrm{d}E}{\mathrm{d}x} = 2\pi r_e^2 m_e c^2 N_{e^-} \frac{Z^2}{\beta^2} \left[\ln\left(\frac{2m_e\,c^2\,W_{\max}\,\beta^2}{I^2\,(1-\beta^2)}\right) - 2\beta^2 - 2\frac{C}{Z_t} - \delta \right] \qquad (1)$$

where Z and β are the particle charge and velocity (scaled to the speed of light c), respectively, r_e and m_e are the electron classical radius and rest mass, respectively, $W_{\max}$ is the largest possible energy loss in a single collision with a free electron, well approximated in the non-relativistic limit by $2m_ec^2\beta^2$, N_{e^-} and I are the electronic density and ionisation potential of the medium of atomic number Z_t, whereas C and δ are the energy and absorber dependent shell and density corrections, respectively. Equation (1) can be extended
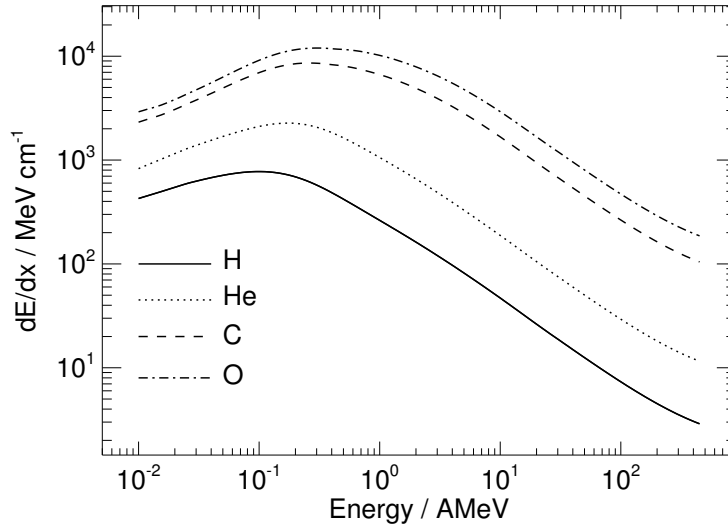
Figure 2–2: *Electronic stopping power of different ions of therapeutic interest calculated in water as a function of the energy on the basis of the ATIMA code [Schw91].*

to lower energies provided that the particle charge Z is replaced by an effective charge Z_{eff} keeping into account the mean charge redistribution due to dynamic loss and capture of electrons from the target for ion velocities comparable to the electron orbital velocity ($\simeq 0.008\,c$). The functional dependence of Z_{eff} on the particle speed can be well approximated by the semiempirical formula [Bar63, Betz72]:

$$Z_{eff} = Z\left(1 - e^{-a\,\beta\,Z^{-\frac{2}{3}}}\right) \tag{2}$$

with $a \simeq 125$ in the original proposal of [Bar63].

The functional relation between the electronic stopping power and the particle energy is shown in figure 2–2 for different ions of therapeutic interest. From the dominant $1/\beta^2 \simeq 1/E$ energy dependence in equation (1) it follows that the energy loss rate increases as the kinetic energy of the particle diminishes along the penetration depth, with a much steeper rise at low residual energy values corresponding to the last few millimetres of the particle path. At the end of the track, however, the stopping power drops due to the rapid reduction of the ion effective charge Z_{eff} at very low energy values according to equation (2). Hence, the distribution of the ionisation density induced by a heavy charged particle along its path shows a rather constant plateau followed by a sharp maximum towards the end, corresponding to the already discussed Bragg-curve. The stopping power describes the loss of energy by the incident particle, whereas the absorbed dose refers to the spatial pattern of energy deposited to a medium either directly by the primary ions or by secondary particles (mostly electrons). In most practical conditions secondary electron equilibrium prevails, that means the energy carried in and out of a volume of interest by secondary electrons is on average the same. Under this assumption the macroscopic dose D delivered by a fluence Φ of mono-energetic heavy charged particles to a medium of density ρ can be directly linked to the average energy loss dE/dx of the ion:

$$D = \frac{\Phi}{\rho}\frac{dE}{dx} \tag{3}$$

The description of the heavy charged particle penetration in a medium as a continuously slowing down process at an energy loss rate mainly given by the electronic stopping power allows to calculate a well defined
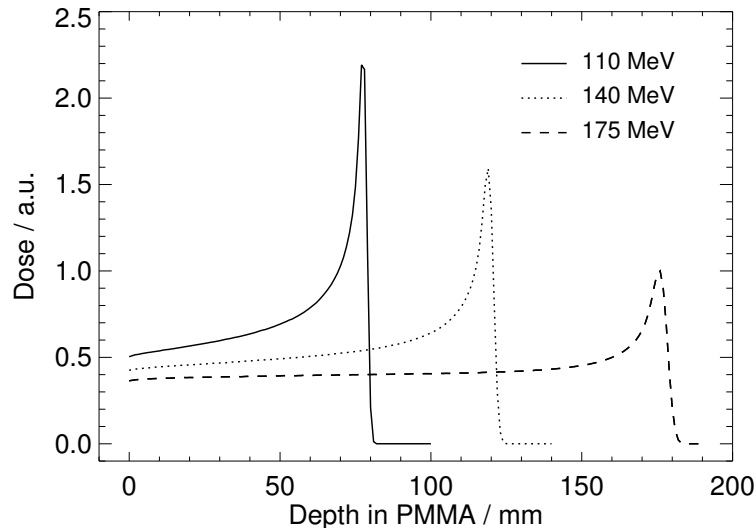
Figure 2–3: *Dose depth profiles in polymethyl methacrylate (PMMA) calculated by means of the FLUKA [Fas01a, Fas01b] code for the same number of primary protons at increasing initial energy values but the same momentum spread of ± 0.1 %.*

mean range R for a given initial energy E_0:

$$R = \int_{E_0}^{0} \left(\frac{\mathrm{d}E}{\mathrm{d}x} \right)^{-1} \mathrm{d}E \tag{4}$$

This integral yields a very close approximation to the finite average path length travelled by an ion in a material. In reality, however, statistical fluctuations of the energy loss around its average value occur [Boh15, Ahl80] and cause a small spread of range values around the mean. This phenomenon is known as *range straggling* and is responsible for the larger width of the Bragg-peak measured for an ion beam with respect to the calculation based on the average energy loss of a single particle. The range straggling increases with the penetration depth in a given material, resulting in Bragg-peaks of larger width and smaller height for higher initial energies of the same ion type (figure 2–3). For different ion species the range straggling approximately varies as the inverse of the square-root of the mass [Lin95]. Therefore, at the same penetration depth heavier ions exhibit a narrower Bragg-peak (figure 2–4) with a steeper distal fall-off and a fragmentation tail beyond the maximum due to nuclear reactions, as described in section 2.1.3. In tissue range straggling amounts to about 1 % of the mean range for protons and only to 0.3 % for carbon ions [Lin95]. Hence, the impact in practical therapeutic applications is smaller or comparable with the unavoidable momentum dispersion of the beam from the accelerator and delivery system.

2.1.2 Lateral scattering

In addition to inelastic collisions with the atomic electrons, heavy charged particles passing through a medium experience also repeated elastic Coulomb collisions with the atomic nuclei, although with a somewhat lower probability [Leo87]. The total recoil energy imparted to the target atoms in these interactions is very small in the energy range of interest ($E \geq 10\,\mathrm{keV}$) and has been therefore neglected in the previous description of energy loss processes. However, the transfer of momentum can lead to a deflection of the particle from its incident direction. After several scattering events a lateral spread and divergence is produced in an ion beam. The net angular distribution of the outcoming particles after a thick absorber with respect to the
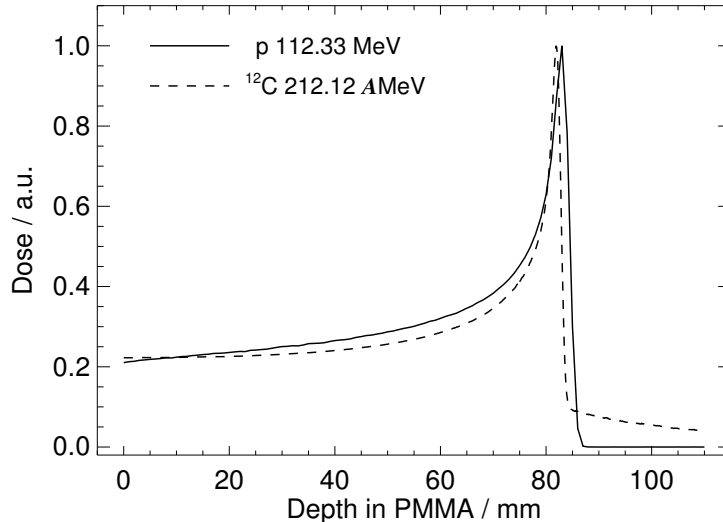
Figure 2–4: *Dose depth profiles in PMMA calculated by means of the FLUKA [Fas01a, Fas01b] and POS-GEN [Has96] Monte Carlo codes for protons and carbon ions at energies of 112.33 MeV and 212.12 AMeV (± 0.1 % momentum spread), respectively, corresponding to a similar mean range of about 82 mm.*

incident direction can be interpreted as the result from several highly probable deflections by small angles as well as rare large-angle single scattering events. The most comprehensive theory of multiple Coulomb scattering within the small-angle approximation is due to G. Molière [Mol48]. However, the central part of the distribution containing very small angular values can be well approximated by a Gaussian shape originating from the statistical repetition of multiple scattering events at small angle ($< 10°$) deflections. A good estimate of the standard deviation σ_θ [rad] is given by the empirical formula [Hig75]:

$$\sigma_\theta = \frac{14.1\,\mathrm{MeV}}{\beta pc} Z \sqrt{\frac{x}{L_{\mathrm{rad}}}} \Big(1 + \frac{1}{9}\log_{10}\frac{x}{L_{\mathrm{rad}}} \Big) \tag{5}$$

where p is the momentum of the particle and L_{rad} and x are the radiation length and mass thickness of the traversed medium, respectively. It follows that multiple Coulomb scattering increases as the particle energy decreases. Furthermore, at energies corresponding to similar penetration depths the lateral deflection is more pronounced for lighter ions. A comparison is given in figure 2–5 for different particles of therapeutic interest. Beams of ions heavier than protons show a well confined lateral broadening ($\leq 1 - 2\,\mathrm{mm}$) at typical penetration depths of relevance for therapy. However, even protons exhibit much less deflection than electrons because of their considerably higher mass. This produces a much sharper fall-off of the lateral dose distribution which can be very useful for delicate irradiation fields adjacent to critical structures.

2.1.3 Nuclear reactions

Unlike conventional radiation species, heavy charged particles can interact with the matter also via the strong nuclear force. The primary quantity for a heavy ion (i.e. nucleus-nucleus) collision is the total reaction cross section σ_R, defined as the total (σ_T) minus the elastic scattering (σ_{el}) cross section for nucleons incident on a nucleus:

$$\sigma_R = \sigma_T - \sigma_{\mathrm{el}} \tag{6}$$

At low energies ($\leq 20\,A\mathrm{MeV}$) nuclear reaction cross sections typically show a strong energy dependence caused by compound nucleus effects [Ahl80] and resulting in pronounced maxima. At larger energies the
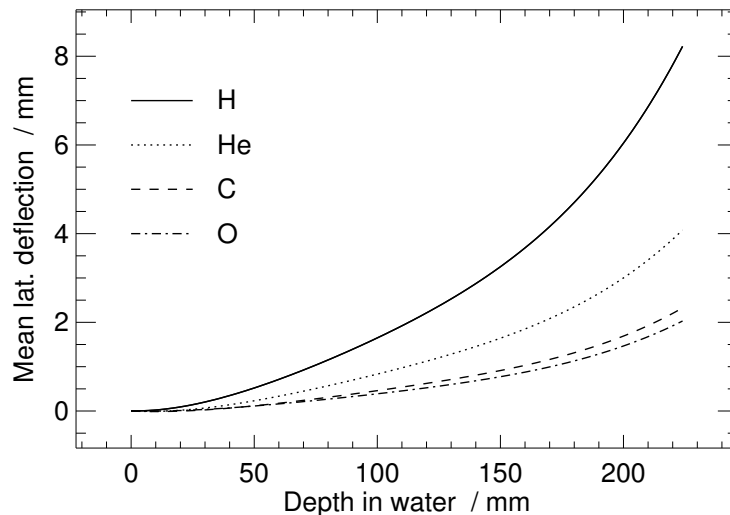
Figure 2–5: *Lateral deflection in water of several ion beams of therapeutic relevance calculated according to [Hab94] and adjusted to the experimental data shown in [Lin95].*

dependence becomes smoother and cross sections approach above about 1.5 AGeV asymptotic values mainly determined by geometrical factors and resembling the energy-independent form proposed on the basis of cosmic ray data [Bra50]:

$$\sigma_R = \pi r_0^2 (A_p^{1/3} + A_t^{1/3} - b_0)^2 \qquad (7)$$

where A_p and A_t are the mass number of the projectile and target nuclei, respectively, r_0 is the proportionality constant in the expression for the geometrical nuclear radius $r = r_0 A^{1/3}$ whereas b_0 is the overlap or transparency parameter.

As a consequence of nuclear interactions, the fluence distribution of the primary particles is exponentially attenuated in depth x according to the expression:

$$\Phi(x) = \Phi_0 e^{-\mathcal{N} \sigma_R x} \qquad (8)$$

where Φ_0 is the initial fluence and $\mathcal{N}$ is the atomic density of the medium. From equation (8) and (3) follows that the dose delivered by the primary ions is reduced with increasing depth due to nuclear reactions, as shown in figure 2–6. However, total reaction cross sections alone are not sufficient for a proper description of nuclear interactions and their impact on therapeutic beams, which is not limited to the attenuation of the primary particles especially for ions heavier than protons. Whereas nuclear recoils give typically negligible contributions to the dose delivery [Pag02, Kar02], secondary nucleons, particles and fragments produced in nuclear reactions can considerably affect the spatial pattern of energy deposition and must be carefully taken into account.

Fragmentation reactions are the dominating interactions in the energy interval and for the material composition of interest for therapy. Nuclear fragmentation is a complex process typically consisting of two steps, where first partially excited prefragments are produced within $\simeq 10^{-22}$ s in the collision and then the final products are formed after de-excitation by nucleon evaporation and photon emission in about $10^{-21} - 10^{-16}$ s [Hüf85]. A recent comprehensive work on fragmentation cross sections [Sih93, Sil98, Tsa98] proposed a semiempirical systematics for proton-nucleus partial cross sections and a scaling approach for the extension to nucleus-nucleus reactions. The systematic regularities of the partial cross section σ_{part} for
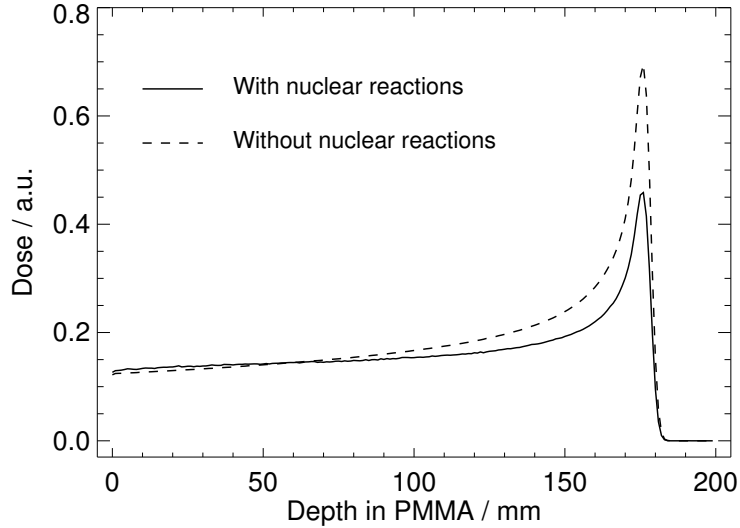
Figure 2–6: *Dose depth distribution in PMMA calculated on the basis of the FLUKA [Fas01a, Fas01b] code for a 175 MeV proton beam including or neglecting nuclear reactions. The reduction of the peak to plateau dose ratio in presence of nuclear reactions is found to be about 35 %, in agreement with previous studies [Lai96, Med97].*

the generation of a given product (Z,A) from a target nucleus were observed first by Rudstam [Rud66] and formulated as:

$$\sigma_{\mathrm{part}} = \sigma_0 e^{-P\Delta A} e^{-R|Z-SA+TA^2|^{3/2}} \tag{9}$$

where σ_0 is a normalisation parameter and the factor $-P\Delta A$ describes the cross section reduction as the mass difference ΔA of target and product increases. The more complex term $e^{-R|Z-SA+TA^2|^{3/2}}$ reproduces the statistical distribution of cross sections for the production of various isotopes of an element of atomic number Z resulting from the stochastic nature of the nuclear evaporation process: the parameter R describes the width of the Gaussian-like distribution and S is related to the peak position, which shifts towards greater neutron excess for heavier products according to the T factor. Silberberg and Tsao [Sil73] have based their semiempirical formulae for proton-nucleus partial cross sections on Rudstam's equation (9) with additional factors introducing a dependence on the specific product nucleus as well as on the energy of the incoming proton. A different equation has been proposed only for the special case of peripheral collisions (i.e. only a partial overlap of the interacting nuclei) leading to products with small ΔA values [Sil73]. Scaling the proton-nucleus systematics for the calculation of projectile-fragment production cross sections in nucleus-nucleus reactions is theoretically founded on the so-called weak-factorisation property [Ols83]:

$$\sigma_{\mathrm{part}} = \gamma_p^f \gamma_{p,t} \tag{10}$$

which decouples the probability of projectile and target interaction (given by the term $\gamma_{p,t}$) from the probability for production of the projectile fragment f (related to the term γ_p^f) in the partial cross section. Following equation (10) the scaling procedure proposed in [Sih93] has been based on a scaling factor S_c corresponding to the $\gamma_{p,t}$ term estimated from a geometry based expression resembling equation (7). The resulting partial cross section $\sigma_{\mathrm{part}}(Z_p, A_p, Z_t, A_t, E_p)$ for the break-up of nuclides (Z_p, A_p) colliding with a target (Z_t, A_t) at an energy per nucleon E_p has been expressed as [Sih93]:

$$\sigma_{\mathrm{part}}(Z_p, A_p, Z_t, A_t, E_p) = S_c \epsilon_L \epsilon_\Delta \epsilon_1 \sigma_{\mathrm{part}}(Z_p, A_p, p, E_{\mathrm{pro}}) \tag{11}$$
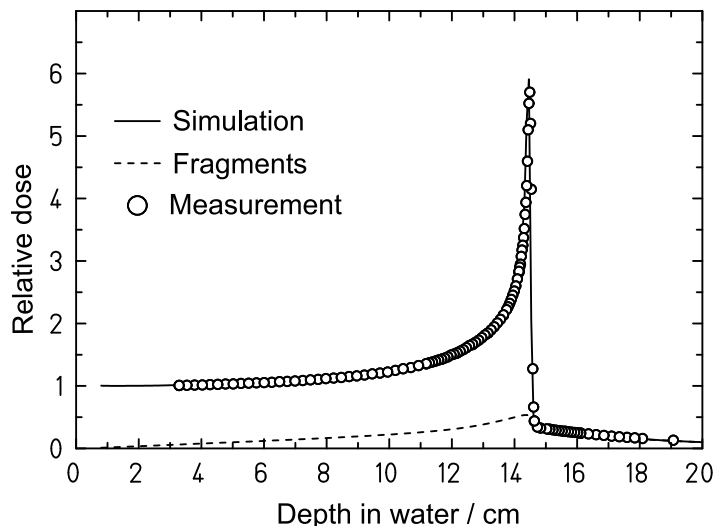
Figure 2–7: *Bragg-curve of 270 AMeV carbon ions measured in water at GSI (open circles) and compared with calculations (lines) including the separate contribution from nuclear fragmentation (dashed line) after [Kra00]. The total dose beyond the Bragg-peak is due to fragments only.*

where $\sigma_{\mathrm{part}}(Z_p, A_p, p, E_{\mathrm{pro}})$ is the partial cross section for the break-up of nuclides (Z_p, A_p) colliding with a proton at a properly scaled energy E_{pro} and ϵ_L, ϵ_Δ and ϵ_1 are correction terms keeping into account deviations from proportionality due to nucleus-nucleus cross section enhancement for the lightest products (Li, Be and B), large ΔA differences and single-nucleon stripping, respectively. The formula originally deduced for projectile fragmentation cross sections can also be extended to target fragmentation reactions by exchange of projectile and target according to the invariance of the cross section for inverse kinematics.

In therapeutic applications peripheral collisions in which fragments are stripped of only few nucleons are by far the most frequent reactions. In the proton case only target fragmentation is possible. Neglecting the heavy target fragments which stay almost at rest in the interaction place, the most important effect of these reactions on the energy deposition is the production of secondary particles, mostly protons and neutrons liberated in (p, xp') and $(p, xp'yn)$ reactions. From this yield only the secondary protons are found to give a significant dose contribution (up to 10 % of the total dose at 160 MeV [Pag02]) in the proximal part of the Bragg-curve because of the lower energy spectrum with respect to the attenuated primary beam. For heavier ions projectile fragmentation is the most important process leading to the build up of secondary particles along the penetration depth. Because of the reaction kinematics, projectile fragments travel nearly in forward direction at almost the same velocity as the incident particle [Gre75] and may therefore cause further fragmentation reactions, while the target nuclei remain approximately at rest at the interaction point. Fragments with $Z < Z_p$ having a longer range of the primary ions give rise to an undesirable dose deposition beyond the Bragg-peak (figure 2–7). Furthermore, the angular emission of the fragments can contribute to an additional lateral spread of the beam particularly evident at the distal side of the Bragg-peak, where the primary projectiles are stopped and the dose deposition is due to nuclear fragments only [Kra00]. Hence, in the case of heavy ions nuclear fragmentation reactions are responsible for the deterioration of the physical selectivity in the longitudinal and transversal dimension especially around the very important Bragg-peak region. The amount of fragments produced increases with increasing mass and charge of the primary particle and is therefore one reason for discouraging the application of ions heavier than neon to therapy. For carbon ions the fragmentation is still within an acceptable limit, especially when using active beam delivery systems (figure 2–7) to avoid projectile fragmentation before entering the patient.

It should be noticed that nuclear reactions are by far the most complex process in the interaction of ions with matter. Therefore, the availability of realistic calculation models for accurate description of fragmentation is a critical issue in radiotherapy, especially for ions heavier than proton (cf. figure 2–7). Although several codes developed for detector design and nuclear safety purposes like GEANT4 [Ago03] and FLUKA [Fas01a, Fas01b] are currently capable of describing ion transport in matter including atomic and nuclear processes, details of nucleus-nucleus collisions may be missed in the energy range and for the materials of therapeutic interest. Hence, dedicated solutions using direct experimental information and tailored to particular applications in radiotherapy (e.g. treatment planning or PET monitoring) are often necessary in order to achieve the desired high precision, as addressed in the following.

2.1.4   Production of positron emitters

For heavy ions the drawback of nuclear fragmentation is more than compensated by the possibility of therapy monitoring by means of positron emission tomography. Fragments stripped of few neutrons and travelling at almost the same velocity as the parent projectiles may be β^+-radioactive isotopes of the primary stable beam stopping nearly at the same penetration depth according to the range dependence:

$$R = \frac{A}{Z^2} f(\beta) \tag{12}$$

where $f(\beta)$ is a function of the ion velocity following from equations (1) and (4). In the case of carbon ion therapy, ^{11}C and ^{10}C are the most abundant β^+-emitting projectile fragments with useful half-lives (1222.8 and 19.3 s, respectively) for PET imaging simultaneously to the tumour irradiation or shortly after the end of the treatment (^{11}C only). Since the stopping process is faster than the radioactive decay, even in on-line monitoring these projectile fragments give rise to a clear and pronounced β^+-activity maximum shortly before the Bragg-peak. As shown in figure 2–8 the peaked signal is superimposed onto a background originating from β^+-emitting target fragments, mostly ^{11}C and ^{15}O. Due to the half-life of 121.8 s the spatial
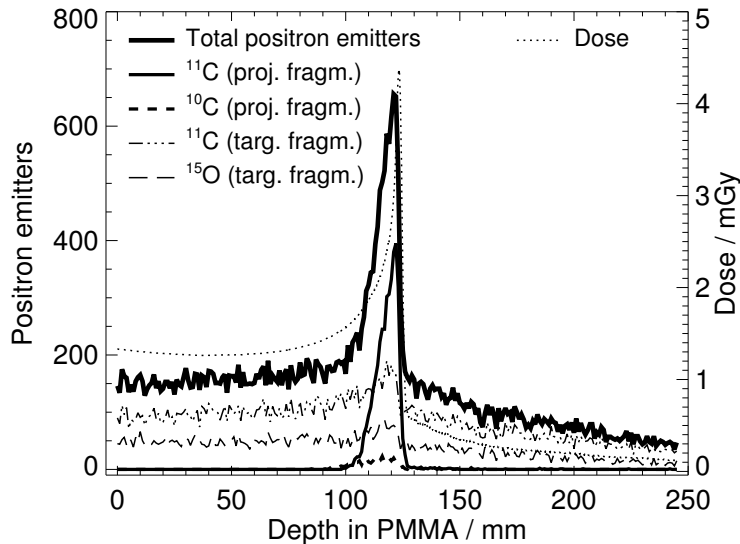
Figure 2–8: *Depth distribution of positron emitters produced in PMMA by 10^5 ^{12}C ions at 270.55 AMeV according to the POSGEN simulation code [Has96], which uses cross section calculations based on equation (11). The main contributions from projectile and target fragments are separately shown. The expected dose depth distribution is additionally depicted by the dotted line.*
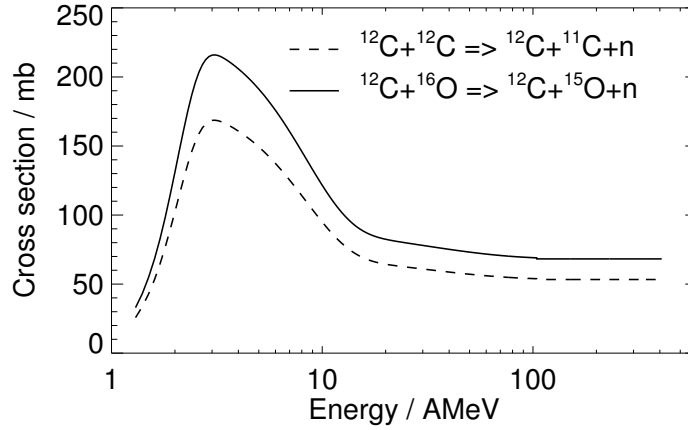
Figure 2–9: *Partial cross sections for the production of ^{11}C and ^{15}O nuclei in the interaction of ^{12}C ions on ^{12}C and ^{16}O nuclei, respectively, implemented in the POSGEN code [Has96] and based on equation (11).*
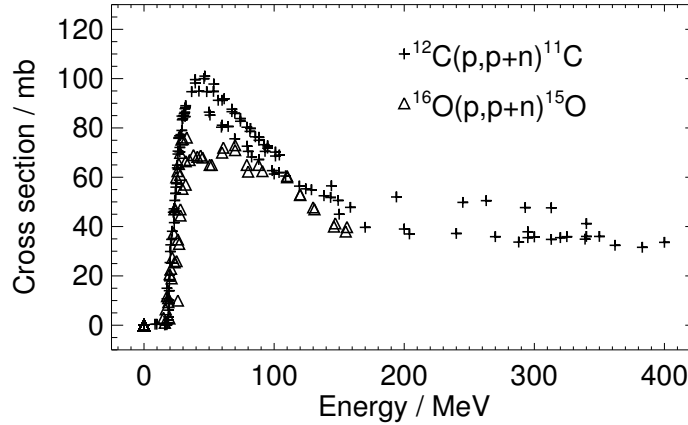
Figure 2–10: *Experimental cross sections for the (p, pn) reaction on ^{12}C and ^{16}O nuclei leading to the production of ^{11}C and ^{15}O β^+-emitting target fragments, respectively [Nuc00].*

distribution of ^{15}O can be detected on-line only. Since the activated target nuclei stay almost at the place of interaction, their spatial distribution contains further useful information on the lateral localisation of the beam and of the dose delivery to be assessed by PET. However, according to the nuclear composition of the tissue and the partial reaction cross sections (figure 2–9), only a small fraction of the stable beam and of the tissue is activated. This results in a relatively low β^+-activity count rate which demands special requirements in the sensitivity of the PET detector and a reduction of background sources (e.g. due to passive beam shaping systems), as it will be discussed in section 2.3. An alternative to therapy with stable beams is the use of primary positron radioactive ions. This results in a strong activity signal carrying direct information on the stopping point of the primary projectiles, as recently demonstrated at HIMAC [Kana02]. On the other hand, there is no real clinical advantage in performing therapy with a β^+-radioactive beam at the expense of nontrivial production and shielding problems.

In the case of protons only β^+-emitting target fragments are produced along the penetration path until the energy drops below the threshold of nuclear reactions, which typically corresponds to few millimetres residual range in tissue. Cross sections are lower than for heavier ions (figure 2–10), but the reduction is compensated by the higher proton fluence required to apply the same therapeutic dose at the lower stopping power due to the lower charge and mass, according to equations (1) and (3). The question on the amount

of useful information that can be extracted from the distribution of β^+-activated target nuclei induced by proton irradiation will be addressed in Chapter 5. As already mentioned in the introduction, similar considerations can be extended also to light ions up to boron.

2.2 The GSI pilot project

After more than 15 years of radiobiological research with ions at GSI Darmstadt, a pilot project has been started in 1994 by GSI in collaboration with DKFZ Heidelberg, Radiological Clinic of Heidelberg University and FZR Dresden with the aim to install an experimental carbon ion therapy unit at the only accelerator complex in Europe capable of delivering heavy ions at the energy necessary for treatment of deep-seated tumours. The facility became operational in December 1997 and up to December 2003 205 patients mainly suffering from chordomas and chondrosarcomas in the head and neck region have been treated safely. In order to investigate the clinical impact of ion beams to the maximum extent, new technological developments have been introduced into clinical routine.

The novel, completely active beam delivery system allows to achieve excellent dose-to-tumour conformity (typically with only two opposite portals) by combining intensity controlled magnetic steering in the lateral direction with active energy variation from the accelerator ($88 - 430 \, A$MeV). The particular time structure of the irradiation delivered by the synchrotron, consisting of repetitions of $\leq 2\,$s particle extraction (spill) and $\simeq 3\,$s extraction pause for a fixed $5\,$s repetition cycle, allows a *pulse-to-pulse* variation of the beam parameters. Hence, in each spill a pencil-like carbon ion beam of well defined focus ($2 - 10\,$mm FWHM) and intensity ($2 \cdot 10^6 - 2 \cdot 10^8\,$ions/spill) is scanned at small step sizes ($\simeq 1/3$ of the focus) in a TV-like mode on a tumour slice of a given depth. Modulation of the number of ions, i.e. of the dose delivered at each scan position is mandatory due to the partial and inhomogeneous pre-irradiation of the proximal (i.e. closer to the origin of the radiation in contrast to distal) slices. The control data for the accelerator and raster scan, namely beam energy, focus, intensity and lateral position, are defined by inverse treatment planning [Krä00a]. The dedicated software developed at GSI is based on accurate analytical models for all the relevant interactions of the primary ions and the resulting fragmentation spectrum in water, with corrections for tissue inhomogeneities on the basis of the X-ray CT of the patient and experimentally verified [Jäk01a] calibration curves between the ion range and CT numbers (or Hounsfield units, HU [Kou82]). The most challenging issue is the inclusion of a novel radiobiological model describing the complex dependence of the biological effectiveness on the particle charge, energy, absorbed dose and tissue type [Krä00b]. Inverse planning techniques allow for optimisation of the physical as well as the biological dose. The latter issue is the most innovative achievement requiring tremendous computational effort due to the intrinsic complexity of radiobiology for the mixed radiation field generated by heavy ions as well as the further requirements from the raster scan system, which demands up to tens of thousands of single scanner positions to be determined. The beam delivery is on-line controlled with feedback during the irradiation by a set of transmission ionisation chambers measuring the number of ions applied at a given position monitored by a multiwire proportional chamber [Vos98]. Precision within $2\,\%$ in intensity and $\pm 1\,$mm in position is achieved. The treatment plan of each individual patient portal is verified by simultaneous measurements using small volume ionisation chambers in a water phantom prior to the first irradiation [Kar99]. Mean and standard deviations between measured and planned dose must be within $5\,\%$ for acceptance of the patient plan. Stereotactic fixation of the patient with orthogonal X-ray verification prior to each dose application further ensures millimetre accuracy of the tumour position [Hee99]. This applies only to the selected anatomical sites not subject to the problem of organ motion. However, the complexity of the raster scan system and the high precision achievable for delicate irradiation of tumours growing in close vicinity to critical organs (e.g. brain stem and

optical nerve) makes an in-situ monitoring of the dose applied to the patient strongly desirable. This is accomplished by means of in-beam PET.

2.3 In-beam PET monitoring of carbon ion therapy

2.3.1 Physical background of PET

The non-invasive monitoring of ion beam therapy is a non-conventional application of PET. In contrast to tracer imaging in nuclear medicine, the β^+-activity source originates from nuclear fragmentation reactions between the projectiles and the target nuclei of the irradiated tissue (section 2.1.4). The produced neutron deficient nuclei can undergo β^+-decay transforming a proton into one neutron with emission of a positron e^+ and an electron neutrino ν_e, which share the available energy from the reaction:

$$A(Z, N) \rightarrow A(Z - 1, N + 1) + e^+ + \nu_e \tag{13}$$

The energy spectrum of the positron is continuous up to maximum possible energy values. For the most abundant isotopes induced by carbon ion as well as proton irradiation, namely ^{11}C, ^{15}O and ^{10}C (see section 2.1.4), these values lie between 1 and 2 MeV. This corresponds to $\simeq 4.5\ldots10$ mm range in tissue. Short-lived β^+-emitters like ^{12}N ($T_{1/2} = 11$ ms), ^{8}B ($T_{1/2} = 770$ ms) and ^{13}O ($T_{1/2} = 8.6$ ms) have higher β^+-endpoint energies up to 16.7 MeV and a considerably longer positron range. They are however neglected in the context of this work due to the low production cross section (except ^{12}N projectile and target fragments induced by ^{12}C ions) and the half-life in the ms region which prevents their detection by the positron camera developed at FZR, as discussed in the next section. Whereas the neutrino escapes from the system without interaction, the positron travels on average about 1 millimetre in tissue rapidly (within $\simeq 10^{-10}$ s) losing its energy in Coulomb inelastic collisions with the atomic electrons and suffering several angular deflections.

Once almost at rest the positron either annihilates as a free particle with an electron of the medium into two photons approximately in $0.2 - 0.4$ ns or captures an electron to form an unstable bound state. Two atomic states called parapositronium and orthopositronium are possible in dependence on the antiparallel or parallel spin orientation, respectively. Because of the very close ground state energy values ($0.84 \cdot 10^{-3}$ eV separation), there is no strong preference for one of the two configurations apart from the 1 to 3 spin multiplicity ratio. According to quantum-electrodynamic selection rules the parapositronium annihilates into 2 photons with an intrinsic – i.e. in vacuum – mean lifetime $\tau = 125$ ps, whereas the orthopositronium can only annihilate into 3 photons with a lifetime $\tau = 140$ ns. However, due to the about 1000 times longer intrinsic mean lifetime the positron bound to an electron in ortho-state has a high probability to undergo a fast para-annihilation with an electron of the medium into two γ-rays. This so called electron pick-off interaction reduces the mean lifetime of the orthopositronium to $0.5 - 5$ ns in matter [Hau79]. As a consequence, the 3γ-emission is in practice negligible and all the detectable radiation can be attributed to the 2 annihilation γ-quanta. According to the momentum and energy conservation law they are emitted at almost 180° in opposite direction and carry each an energy of 511 keV equal to the positron and electron rest mass. Deviations from collinearity can occur because of the residual energy of the electron-positron system, leading to emission angles approximately distributed according to a Gaussian centered at 180°. The width of the distribution is $\simeq 0.3°$ FWHM for typical residual energy values of about 10 eV [Wie89].

The γ-ray pairs are isotropically emitted in the full solid angle of 4π and can be detected by couples of opposite detectors operated in coincidence giving the lines-of-response (LORs) of the system. With tomographic acquisition techniques and suitable reconstruction algorithms it is possible to retrieve the unknown spatial distribution of the β^+-activity source. The two basic assumptions underlying the reconstruction approach in PET are that (*i*) the nucleus from which the positron originated is exactly located along the

**True coincidence**   **Random coincidence**   **Scattered coincidence**
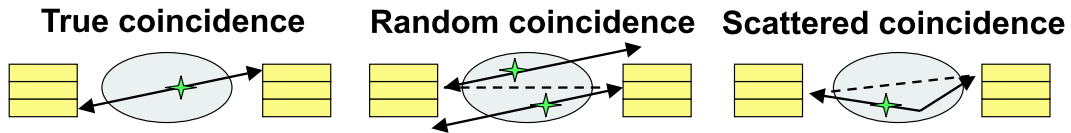
Figure 2–11: *Representation of true (left), random (middle) and scattered (right) coincidence events. The solid lines show the real photon pathways, whereas the dashed line is the assigned line of response to the detected coincident γ-ray pair.*

line at which the two photons are emitted and (*ii*) the two annihilation photons are emitted at 180° opposite [Bend98]. The limited validity of these approximations due the finite distance travelled by the positron from the creation point as well as the non-collinear emission of the annihilation photons restricts the intrinsic achievable spatial resolution of PET to $2 - 3\,$mm [Wie89]. This value is however still below the $\simeq 5\,$mm practical spatial resolution of the current commercial full-body PET scanners, which is mainly determined by the dimension of the single detector units (typically crystals of scintillation materials like bismuth germanate, BGO [Cho77]). Further physical processes affecting the measured data are the reduction of detected photon pairs along the LORs due to attenuation within the object under investigation as well as the incorrect assignment of emission lines to photon pairs detected in coincidence but either not originating from the same annihilation event (random coincidences) or reaching the detector after angular deflection due to scattering in the object (scattered coincidences), as shown in figure 2–11. However, in conventional PET imaging these effects can be rather well quantified and corrected for on the basis of experimental measurements like transmission scans with external sources for the problem of attenuation or model calculations for the estimation of the amount of scattered events in the acquired data. The specific solutions tailored to the dedicated detector installed at GSI will be briefly addressed in the next section.

2.3.2   The dedicated in-beam positron camera

The in-beam positron camera completely integrated into the treatment unit at GSI Darmstadt is a limited angle double head scanner developed by FZ Rossendorf [Eng99a]. This geometrical configuration avoids interference with the fixed horizontal beam line as well as restrictions to the positioning of the patient (figure 2–12). The two large area $(42 \times 21\,\mathrm{cm}^2)$ detectors disposed on a portion of a sphere of about $83\,$cm diameter are built from components of the commercial ECAT EXACT PET scanner (CTI PET Systems Inc. Knoxville, TN, USA). Each head consists of 8×4 position sensitive scintillation blocks of bismuth germanate of $54 \times 54\,\mathrm{mm}^2$ front face and $20\,$mm interaction depth [Cas86]. The blocks are further subdivided into an 8×8 crystal matrix of $6.75\,$mm pitch, resulting in $4\,194\,304$ lines of response in coincidence operation. The scintillation light is read out by four photomultiplier tubes coupled to each block and a crystal identification is performed according to a modified Anger principle [Paw95]. On the basis of the scintillation properties of BGO, the time width for coincidence detection is set to $12\,$ns. Photon pairs hitting opposite crystals within either a prompt or a delayed (by $128\,$ns) coincidence window are acquired. This allows to apply the standard random correction technique based on subtraction of delayed from prompt coincidences. The acceptance energy window for scatter discrimination is set to the default $250 - 850\,$keV interval recommended by CTI.

The data acquisition system extends the standard solution implemented by the manufacturer [Jon86]. It enables the storage of events in histogram mode. In addition, list mode acquisition was introduced with insertion of time labels every $10\,$ms into the data stream for dynamic imaging. Furthermore, the specific information on the status of the irradiation (beam on/off) as well as the parameters of the accelerator (beam energy, focus and intensity) are registered. The former allows to discriminate the highly noisy data recorded during beam extraction. These events mainly originate from β^+-emitters with half-lives in the
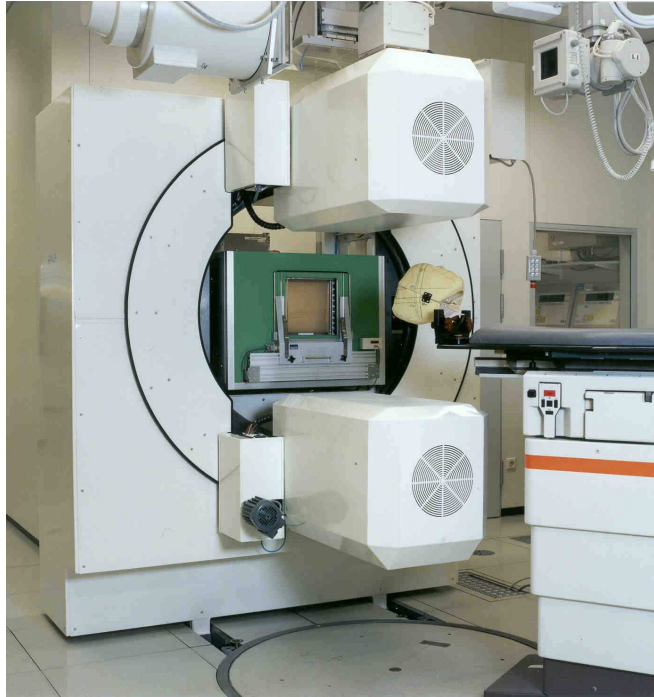
Figure 2–12: *Double head positron camera installed in the treatment site at GSI Darmstadt. The exit window of the horizontal carbon ion beam is visible in the square green area in the centre. The camera heads are kept fixed in the shown vertical position above and below the patient couch during PET monitoring [Eng04a].*

millisecond time scale and corresponding high β^+-endpoint energies (section 2.3.1) or from γ-rays following nuclear reactions and generating random coincidences not properly corrected for by the standard technique of subtraction of delayed events, as indicated by the investigation presented in Chapter 4. Therefore, these data are currently discarded from further processing since they either tend to broaden the β^+-activity distributions or do not contain at all information on the dose delivery. Hence, the PET images are reconstructed only from those annihilation events registered in the beam extraction pauses during the application of the treatment and, furthermore, during the few minutes immediately following the end of the irradiation. The limited acquisition time of about 10 min per irradiation field, the average size of the treated volume from 100 to 200 cm^3, the total number of delivered ions approximately ranging from 10^8 to 10^9 at typical energies between 100 and 300 AMeV as well as the low detection efficiency ($\simeq 2.5\,\%$) of the scanner determine the quite small amount of valuable events. The PET data sets typically contain up to $10^4 - 10^5$ true coincidences at usual clinical doses of $\simeq 0.5 - 1\,$Gy [Eng99b]. This extremely low statistics, orders of magnitude below that in standard application of PET to nuclear medicine, in combination with the shift-variant response of the limited angle system demands special effort in image reconstruction. A practicable solution has been found by the development of a dedicated iterative algorithm [Lau99] implementing the Maximum Likelihood Estimation Maximisation (MLEM) approach [She82]. Corrections for attenuation and scattering have been included on the basis of analytical and Monte Carlo calculations, respectively, modelling the annihilation photon transport within the patient according to the known physical interactions and the anatomical information given by the planning X-ray CT [Pön03a]. Images reconstructed from PET data acquired during fractionated tumour treatment at GSI Darmstadt have been successfully used for the quality assurance of carbon ion therapy since the first patient irradiation in 1997 [Gro98], as discussed in the next section. It must be noticed that the dedicated PET scanner takes full advantage of the completely active beam delivery system developed at GSI, which avoids contamination of the very low β^+-activity count rate due to the absence

of elements in the beam (e.g. collimators and range shifters) that can be easily activated or influence the primary beam quality.

2.3.3   Clinical implementation

The spatial distributions of β^+-activity and dose are correlated but not identical (figure 2–8), due to the different nuclear and electromagnetic interactions underlying positron emitter production and energy deposition, respectively. Therefore, PET monitoring of carbon ion therapy at GSI is based on a comparison between measured and expected β^+-activity distributions. The latter quantity is calculated on the basis of two dedicated Monte Carlo codes [Has96, Pön03a] which realistically describe all the relevant physical processes from the stopping of the ions in the patient, the production and decay of β^+-radioactive nuclei, the emission, transport as well as annihilation of the positrons and the propagation of the γ-ray pairs until the coincident detection by the scanner. Actually, the first code calculates the production of positron emitters induced by mono-energetic pencil-like carbon ion beams of tunable lateral size in homogeneous organic plastic (PMMA). This program has been used to generate a database containing 3D spatial distributions of β^+-emitters for all the 252 discrete energy values delivered by the synchrotron for therapy. In a second step the database is adapted to the specific patient case by taking into account (*i*) the particle delivery to the target volume given by the control parameters of the accelerator and the raster scan unit, (*ii*) the X-ray CT, allowing to correct for tissue inhomogeneity and to determine the ion range on the basis of the same calibration curves [Jäk01a] used for treatment planning [Krä00a], as well as (*iii*) the time course of the irradiation for each particular treatment fraction of the considered portal. The latter information is necessary due to the dynamics of the β^+-activity formation, decay and washout, which is therefore very sensitive to the daily variations of the time dependent beam application for the same irradiation field. The output of the simulation is a list mode data set of predicted annihilation events detected in coincidence with the structure of the measured data. This allows to reconstruct both measured and simulated data with the same MLEM algorithm and, therefore, avoid possible influence of different data processing in the final comparison. In order to support visual inspection, the PET images are finally superimposed onto the X-ray CT [Pön99]. This is feasible with high precision on the basis of the accurate stereotactic positioning procedure of the patient in all the therapy steps, namely diagnostic imaging, treatment planning and irradiation with in-beam PET acquisition.

In clinical routine the PET quality control is performed for each field of each irradiated patient throughout the entire therapy, typically consisting of 20 daily dose applications for a fully fractionated carbon ion treatment or only 5 to 6 sessions for a carbon ion boost combined to conformal photon therapy [Deb00]. The processing and evaluation of the PET data is completed within few hours after the irradiation, in order to allow potential discrepancies between real and planned treatment to be compensated in the next fraction.

2.3.4   Clinical results and future perspectives

The first clinical results for more than 200 patients having been treated so far allow to draw first conclusions on the clinical helpfulness of the PET quality assurance, due to the possibility to (*i*) monitor the maximum carbon ion range, (*ii*) verify the position of the irradiation field and in some cases (*iii*) detect possible unpredictable deviations between real and planned treatment. PET is in fact capable of testing the whole chain from treatment planning to dose application independently from the dose delivery. The extraction of information on the maximum particle range from the distal edge of the measured β^+-activity distribution allows to validate *in-vivo* the physical beam models used in both of the PET simulation as well as the treatment planning code. Systematic deviations between measured and precalculated PET images observed

21
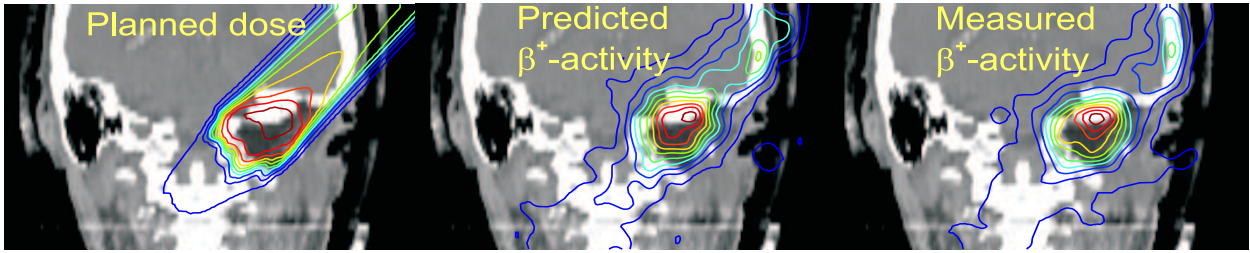
Figure 2–13: *Left: Planned dose distribution (shown by isodose lines at 10 % separation from 5 to 95 % of the maximum in colours from blue to red) superimposed onto the frontal slice of the grey scaled X-ray CT for a cranio-lateral irradiation field stopping in front of the radiosensitive brain stem. Middle: Predicted β^+-activity distribution. Right: Measured β^+-activity distribution, found in good agreement with the prediction. In particular, the distal edge of the measured activity ends in front of the critical organ as planned.*

in the early therapy sessions in 1998 indicated a lack of accuracy in the correlation between CT numbers and carbon ion range, especially in the region of soft-tissue [Eng00]. More precise range measurements started at GSI on the basis of the PET observation lead to the improved calibration curve currently in use [Jäk01a, Krä00a], resulting in the fairly good correspondence between measured and predicted β^+-activity distributions noticed since February 1999 [Eng00].

Consequently, the higher reliability of the precision of the ion range in tissue allowed to extend treatment plans also to more critical irradiation fields. This is shown in figure 2–13 (left) for a cranio-lateral portal where the beam has to be stopped precisely in the tumour in front of the organ at risk, i.e. the brain stem. PET monitoring of such delicate clinical situations is important. For this patient the comparison between measured and predicted β^+-activity distributions shows a good correspondence, indicating a correct delivery of the treatment and, in particular, the proper sparing of the critical organ as planned (figure 2–13). In-situ verification of the lateral position of the field can be also a crucial issue, especially in the frequent case of irradiation adjacent to critical structures. Figure 2–14 shows an example where a cranial portal has to pass between the eyes without touching the radiosensitive optical nerves. Again the measured PET distribution is in fairly good agreement with the simulation. However, in some cases deviations between real and planned treatment may occur because of minor inaccuracies in the positioning of the patient or local and frequently temporary anatomical modifications (e.g. tissue reduction or cavity filling by mucus) within the irradiated region [Eng99c]. Such modifications, whereas rather uncritical in conventional radiotherapy, may severely affect the dose deposition and result in undesirable underdosage within the tumour or critical overdosage in radiosensitive organs, compromising the effectiveness of the therapy. Hence, in these situations
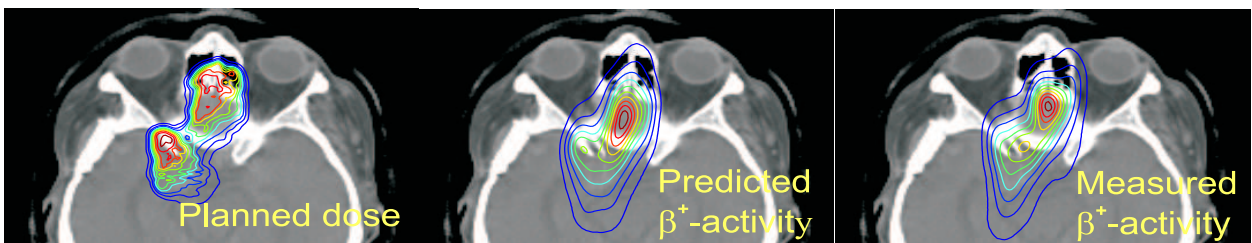
Figure 2–14: *Left: Planned dose distribution superimposed onto the transverse slice of the X-ray CT for a cranial field passing between the eyes. Middle: Predicted β^+-activity distribution. Right: Measured β^+-activity distribution. The radiosensitive optical nerve is spared as planned.*

a quantification of the local dose deviation on the basis of PET data is strongly desired by the radio-oncologists. The problem has been addressed in this work and the developed interactive approach is described in the next chapter. However, more accurate solutions still demand higher counting statistics and better quality of the PET images. Therefore, this issue is connected to the problem of noisy acquisition of the in-beam positron camera during beam extraction investigated in Chapter 4.

On the basis of the positive clinical impact, in-beam PET monitoring of carbon ion therapy will be implemented at the proposed ion beam tumour therapy facility of Heidelberg [Gro98]. This hospital-based centre will have treatment sites resembling the GSI experimental therapy unit but will additionally be able to deliver particles from protons up to oxygen nuclei. Hence, the possible extension of the PET method to other ion species is worthwhile of being considered. The investigation on the potential of in-beam PET for the monitoring of proton therapy is addressed in Chapter 5.

3 Dose quantification from in-beam PET data

3.1 Motivation

In-beam PET monitoring of carbon ion therapy at GSI Darmstadt is based on the visual inspection of measured and predicted β^+-activity distributions superimposed onto the anatomical information given by X-ray computed tomograms. If the comparison indicates deviations between planned and really applied treatment, the radio-oncologist is informed in order to allow a prompt intervention in the delivery of the successive treatment fraction. However, the clinical relevance of the deviation cannot be easily extracted from PET images alone. The information demanded with highest priority by the radio-oncologist is the discrepancy in the delivered dose, especially with respect to the targeted tumour and the radiosensitive critical structures. In the following, only the physical dose is concerned. Nevertheless, the question has no trivial answer, because of the different physical mechanisms underlying the atomic and nuclear processes responsible for energy deposition and positron radioactivity production, respectively. The imaged β^+-activity distribution may be furthermore affected by perfusional and metabolic processes. In addition to the dependence on the time course of the irradiation and acquisition this results in different PET images for the same dose application. Hence, uniqueness is not necessarily fulfilled.

The most appropriate solution to the problem would be the development of an algorithm capable of delivering the most probable dose distribution for a given PET image measured at known boundary conditions (e.g. time course of the irradiation and acquisition). This requires a solution for the inverse problem from the positron radioactivity distribution $A(\mathbf{r})$ to the applied dose $D(\mathbf{r})$. Such a relation can be mathematically described by the equation $\mathbf{A} = \mathbf{T} \times \mathbf{D}$, where the quantity $\mathbf{T}$ is the transition matrix giving the probability that a given dose contribution $dD(\mathbf{r})$ corresponds to the production of an activity density $dA(\mathbf{r'})$. However, several limitations of the presently available PET images discouraged the attempt to face this challenging and very ill-posed inverse problem. The β^+-activity distributions reconstructed by means of the iterative MLEM algorithm [Lau99] are not yet quantitative, despite the introduction of attenuation and scatter corrections [Pön03b]. The reason is the normalisation problem at each iteration step. Furthermore, the extremely low counting statistics in combination with the limited angle geometry of the positron camera unavoidably deteriorates the image quality. Possible limited angle artifacts propagate in the same way in the reconstruction of measured and predicted events, hence not affecting the reliability of the PET monitoring itself. Nevertheless, they further complicate the problem of extracting information on the dose delivery from the imaged positron radioactivity distributions. Finally, biological pathways washing out the produced positron emitters [Kau02] are not yet taken into account in the prediction or corrected for in the measured data. Moreover, the dynamic build-up of the β^+-activity throughout the treatment volume due to the active beam delivery system in use at GSI prevents the alternative possibility to monitor the integrated dose by monitoring the total number of annihilation events detected as a function of time, as proposed in [Lit99] for protons. In order to overcome all these limitations and provide a practicable solution for in-beam PET monitoring with the presently available hardware and software imaging capabilities, an interactive approach has been developed. The basic idea and the implementation with clinical examples are described in the following section. The clinical impact and outlook is discussed in the concluding section 3.3.

3.2 The interactive solution

From the clinical experience at GSI, the reasons for unpredictable deviations between planned and delivered dose distributions have been mostly identified in minor misalignments or local anatomical changes of the patient with respect to the situation depicted in treatment planning (TP). This is illustrated by means of
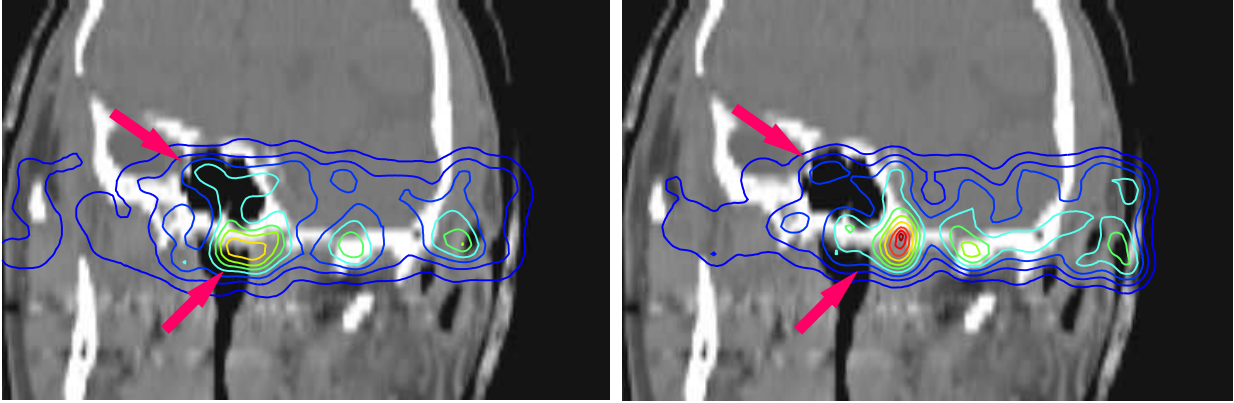
Figure 3–1: *Case (a): measured (left) and predicted (right) β^+-activity distributions (displayed by coloured isolines as in figure 2–13 but normalised to the global maximum instead of that in the considered image plane) superimposed onto the frontal slice of the X-ray CT for a portal entering the patient from the left side (right in figure). The arrows indicate the discrepancies discussed in the text, suggesting a caudal shift of the patient in this treatment fraction.*
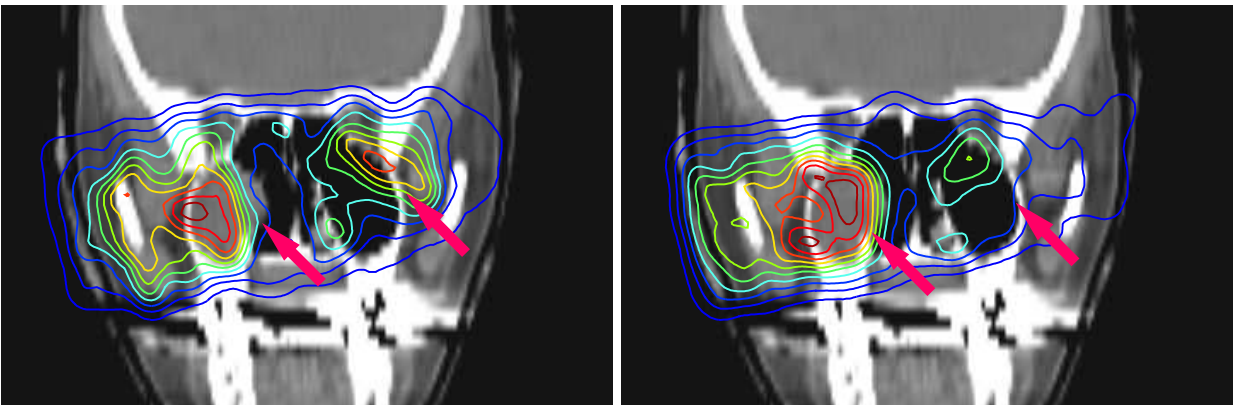
Figure 3–2: *Case (b): similar comparison as in figure 3–1 (but normalisation of the β^+-activity isolines to the maximum within the imaged plane) for an oblique portal entering the patient from the right side (left in figure). Again the arrows point at the discrepancies suggesting a local tissue reduction (cf. text).*

two clinical examples which are utilised throughout the whole chapter for explaining the dose quantification technique. They are given in figures 3–1 and 3–2. In case (a), figure 3–1, a caudal shift of the patient was particularly indicated by the marked mismatch of the measured β^+-activity with respect to the bony structures, where the activity is accumulated. In case (b), figure 3–2, a tissue reduction was suggested by the systematic observation of distal β^+-activation at longer penetration depth than planned in combination with an insufficient shaping of the β^+-activity contour lines at the right side (left in picture) of the nasal cavity.

As a matter of practical training in inspecting PET images, the two mentioned physical explanations can be separated from biological effects due to β^+-activity washout or perfusion. However, plausible conjectures for the observed deviations cannot be in general identified and assessed so easily. Hence, in order to support the PET operator in validating the hypothesis and estimating the corresponding local dose deviation, the interactive approach illustrated by the flow chart of figure 3–3 has been developed. The software implementation performed in IDL (Interactive Data Language) and C programming languages has been completely integrated into the dedicated home-made code VIEW_PCT originally developed for the visualization of the measured and predicted PET distributions as contour plots superimposed onto X-ray CT images [Pön03a].
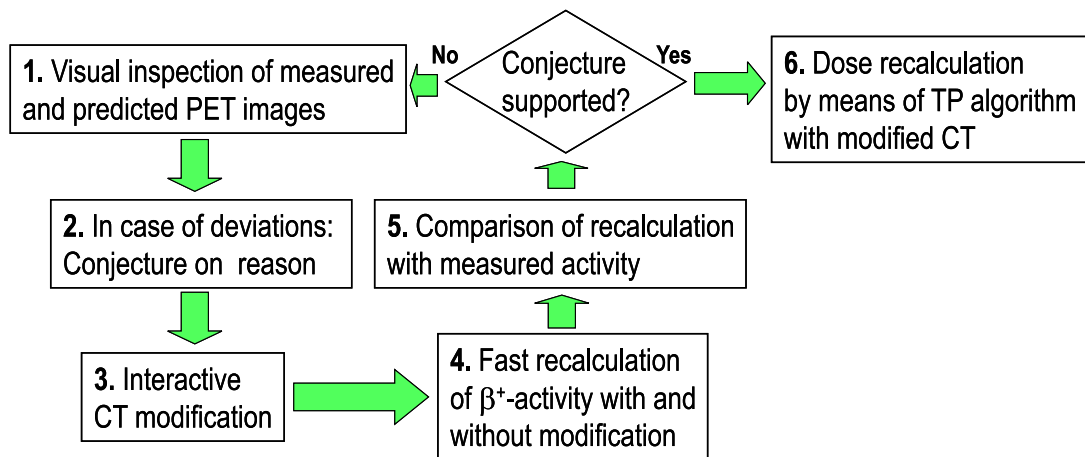
Figure 3–3: *Flow chart of the interactive approach used for local dose quantification from PET images in routine monitoring of carbon ion therapy at GSI Darmstadt.*

Details on the single steps $3 - 6$ of the diagram shown in figure 3–3 are briefly described in the following. The tool is routineously in clinical use since 2001.

3.2.1 Interactive modification of the patient X-ray CT

A session devoted to the interactive manipulation of the treatment planning X-ray CT can be activated by the PET operator directly from the slightly modified main menu of the original visualisation program VIEW_PCT described in [Pön03a]. The additional interactive menu "MODIFY CT" appears and guides the user in the permitted operations, which have to be defined by means of mouse actions (figure 3–4). The modifications may consist in rigid geometrical transformations (translation, rotation) and, furthermore, in
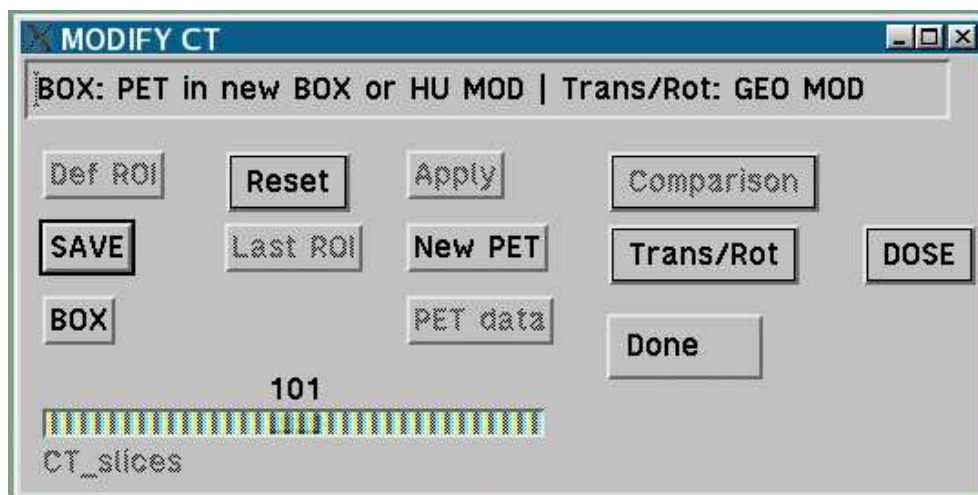
Figure 3–4: *Interactive menu of the PET evaluation tool for the functions for dose quantification. In dependence on the possible operations the sensitivity of the buttons changes and additional pull-down menus or sliders may appear. The dialog box on top of the window provides additional information, in this example the suggestion to press the button "BOX" for initiating Hounsfield units manipulations or PET recalculations in extended regions or to press the button "Trans/Rot" for geometrical modifications (cf. text).*
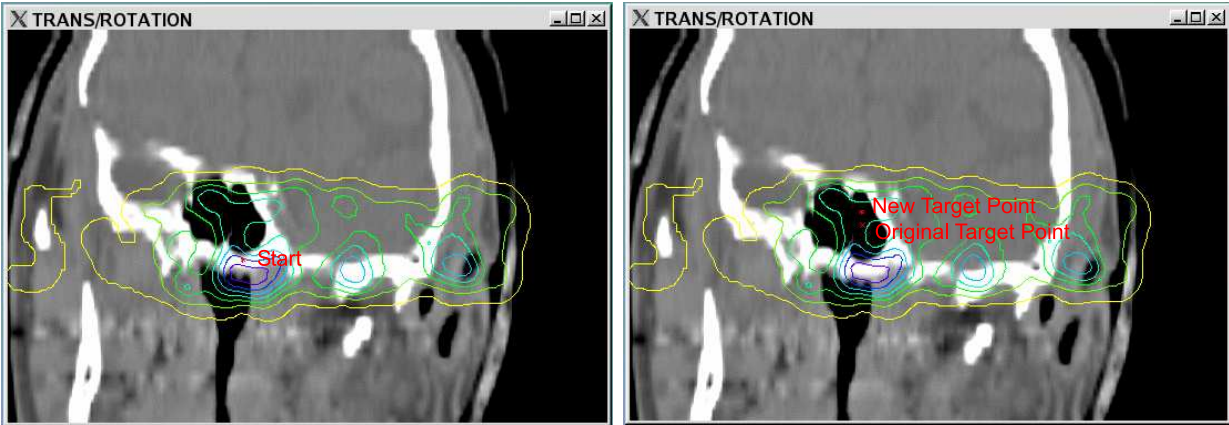
Figure 3–5: *Example of the application of a translation, requiring the definition of the translation vector by means of mouse clicks. The selected initial point " Start" is shown in the left figure, referring to the measured PET data for the considered case (a) (figure 3–1). The chosen caudal shift resulting in the better match of the β^+-activity distribution with the bony structure (right) corresponds to a cranial shift of the target point, indicated by the "Original Target Point" and "New Target Point" positions.*

local changes of Hounsfield units (HU) in user-selected regions of interest (ROI). The Hounsfield units:

$$\mathrm{HU} = 1000 \, \frac{\mu - \mu_{\mathrm{H_2O}}}{\mu_{\mathrm{H_2O}}} \tag{14}$$

express the X-ray attenuation coefficient μ of the material of a given CT voxel relative to that of water $\mu_{\mathrm{H_2O}}$ and therefore provide information on the patient anatomy.

In principle, geometrical transformations may correspond to a redefinition of the beam orientation with respect to the same CT image or to an effective modification of the CT image with respect to the fixed coordinate system specified by the treatment plan. For a practical implementation keeping into account the available utilities tailored to the horizontal beam line and beam delivery system in use at GSI, rotations have been chosen to result in really manipulated CT images, in analogy to local Hounsfield unit modifications. On the contrary, translations lead to a simple redefinition of the target point coordinates in the treatment plan. The latter choice avoids to deteriorate the CT information (e.g. introducing partial volume effects) for typical maximum misalignments of $1 - 2\,\mathrm{mm}$ comparable to the CT voxel size ($\simeq 1\,\mathrm{mm}$ in the transaxial plane and $\simeq 3\,\mathrm{mm}$ along the axis of the X-ray computerised tomograph). As for the original visualisation capabilities of VIEW_PCT, the definitions of the transformations are restricted to the frontal, transversal and sagittal planes of the X-ray CT. The result of each operation is always displayed before becoming effective. In this way the user can always decide whether to apply or reset a given modification. The manipulated CT (or new target point coordinates) can be finally stored in the same format of the planning CT (or treatment plan) with additional detailed information on the modification (e.g. axis and angle of rotation or translation vector). Examples for the two considered clinical cases are given in figures 3–5 and 3–6.

3.2.2 Fast recalculation of β^+-activity distributions

In order to assess the plausibility of the interactive modification, a recalculation of the β^+-activity distribution with and without the CT changes has to be performed and compared with the originally measured and predicted PET images. Since several iterations of the whole procedure may be sometimes necessary before finding out the most plausible conjecture, the applicability to clinical routine demands the results of each calculation to be available within few seconds or at the most a few minutes. Hence, the computing time
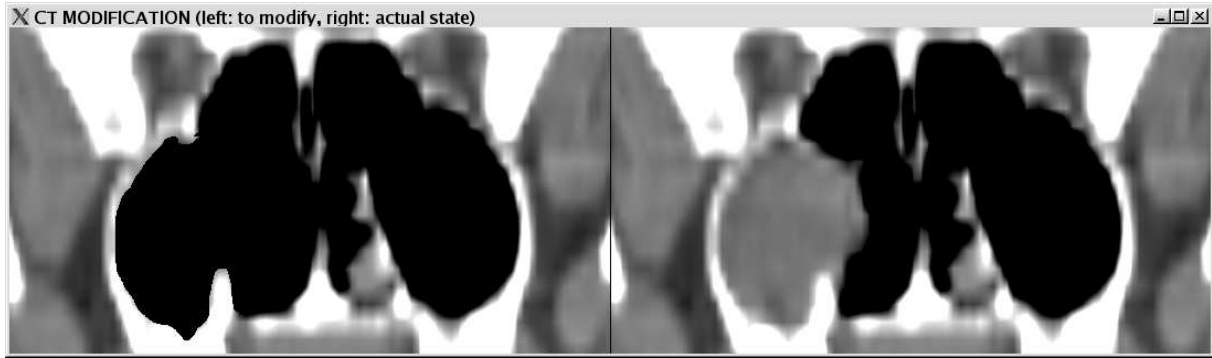
Figure 3–6: *Example of HU manipulation for the considered case (b) (figure 3–2). The two enlarged subportions of the CT slice refer to the working area prior to the application of the defined tissue reduction (left) and the original status (right). The definition of ROI within the working area is done via the mouse, whereas an additional slider for HU values modification appears in the menu after the ROI definition is completed. Measured PET data can be additionally superimposed in order to aid the modification.*

of the β^+-activity recalculation is a crucial issue. This forbids a full simulation with iterative tomographic reconstruction, requiring at least half an hour for completion (cf. section 2.3.3). Therefore, a dedicated code partly based on routines of the PET simulation code [Has96] has been implemented. Actually, the program exclusively computes spatial distributions of β^+-decays and does not take into account the complete PET imaging procedure (e.g. positron annihilation, photon pairs propagation, detection and iterative image reconstruction) in order to achieve the desired fast response (e.g. 15 s on an Intel® Xeon™ 3.06 GHz CPU for a 660 cm³ large treatment volume when taking into account all the $1.5 \cdot 10^8$ ions delivered to 3814 different scan positions). From the control data of the accelerator and raster scan only those pencil-like beams crossing an user-defined ROI are considered. The depth-distribution of the main β^+-isotopes (^{11}C, ^{15}O and ^{10}C) is extrapolated from the PET database (DB) [Has96] containing the spatial distributions of positron emitters produced in PMMA (composition: $C_5H_8O_2$, density: 1.18 g cm^{-3}) by ^{12}C pencil-like ion beams of all the energy values used for therapy. The DB information is combined with the beam delivery control data (ion beam energy, focus, fluence and position) and with the patient anatomical information given by the X-ray CT. The longitudinal adjustment to the estimated penetration depth in the patient is obtained from the HU-ion range correlation [Has96, Jäk01a, Krä00a]. The correction of the distribution according to the tissue density and the tissue elemental composition for the proper weighting of the target fragments is deduced from the stoichiometric calibration of the CT numbers suggested in [Schn00]. The lateral distribution of the induced β^+-activation is assumed to be Gaussian with a FWHM dependent on the beam focus and the average positron range in tissue. The lateral spread of the beam in depth is neglected in analogy to the treatment planning algorithms, because of the negligible lateral straggling of carbon ions. The spatially variant amount of β^+-decays is finally deduced from the fraction of isotopes decayed within the time interval between production (coinciding with the application of the considered pencil-like beams) and the end of the PET acquisition on the basis of the registered time course of the considered irradiation.

The described code, written in C language, has been fully coupled to the IDL visualisation program. The recalculation is directly activated by the user when pressing the "New PET" button in the "MODIFY CT" interactive menu. After completing a computation for a given region of interest, the PET operator can arbitrarily extend it to include further ROI. Results are displayed using the navigation capabilities of the original VIEW_PCT program reported in [Pön03a]. Its basic functionalities have been further enlarged in order to allow comparison of several quantities (PET recalculated distributions with or without modification, original PET measurements, predictions and differences) and produce the corresponding graphical documen-
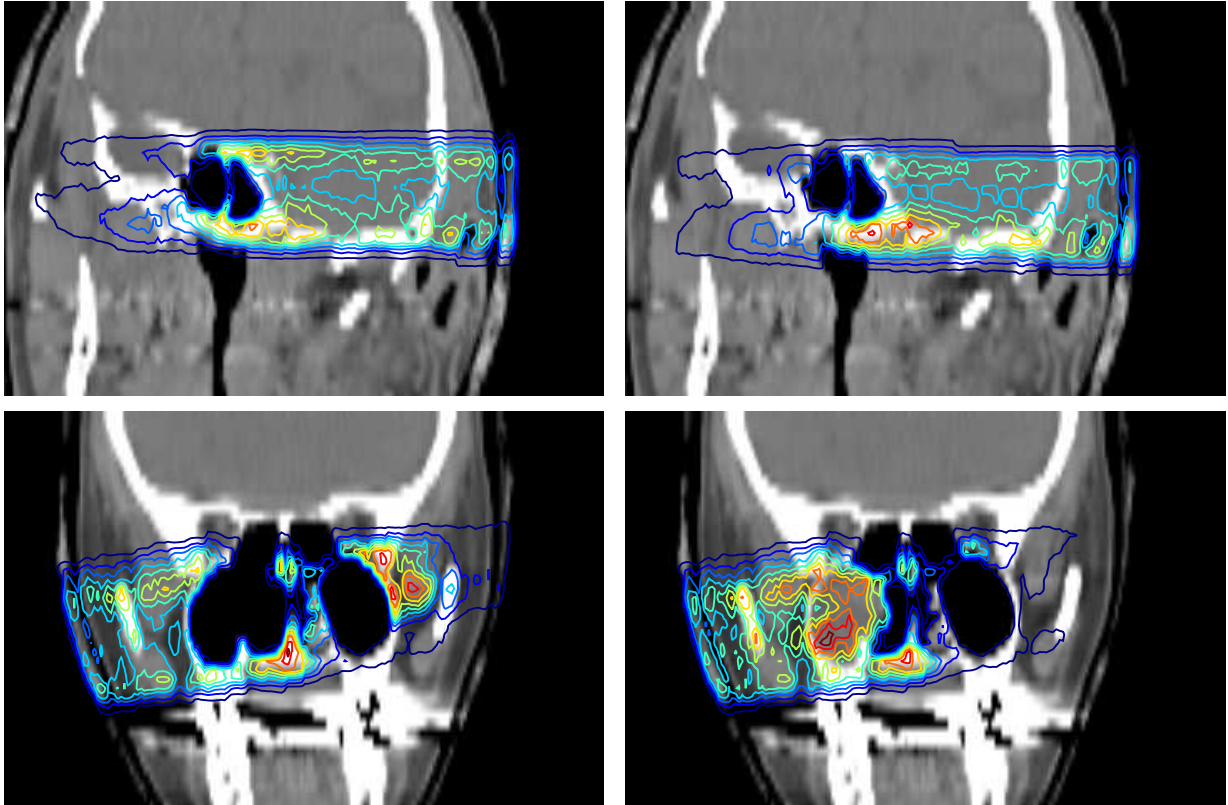
Figure 3–7: *Recalculation of β^+-activity distributions with (left) and without (right) the modification, consisting in the conjectured $\simeq 4$ mm caudal shift shown in figure 3–5 for the considered case (a) (top) and the substantial tissue reduction suggested by the PET measurement in case (b) (bottom).*

tation. Satisfactory recalculations for the two considered clinical examples are illustrated in figure 3–7, to be compared with the original measured and predicted PET images shown in figures 3–5 (right, showing the PET measurement superimposed onto the translated CT) and 3–2. Despite the absence of imaging effects, the fast recalculations with the modifications discussed in 3.2.1 can clearly reproduce the trend observed in the measured data.

3.2.3 Local quantification of the dose deviation

When the PET recalculation supports the conjectured modification, a new dose distribution based on the manipulated CT (or treatment plan in case of translation) can be directly issued by the PET operator via the interactive menu. The dose recalculation is accomplished by means of the treatment planning software [Krä00a] with the new input information. As for the PET recalculations, the results can be inspected and documented according to the visualisation capabilities of the original VIEW_PCT tool. Differences between the originally planned and the recalculated dose distributions are quantified. As an example, the resulting dose recalculations and corresponding deviations for the two considered clinical cases are depicted in figure 3–8 and 3–9. It should be however mentioned that the somehow impressive deviation does not involve critical structures and is mitigated in both cases by the application of a treatment field from the opposite direction.
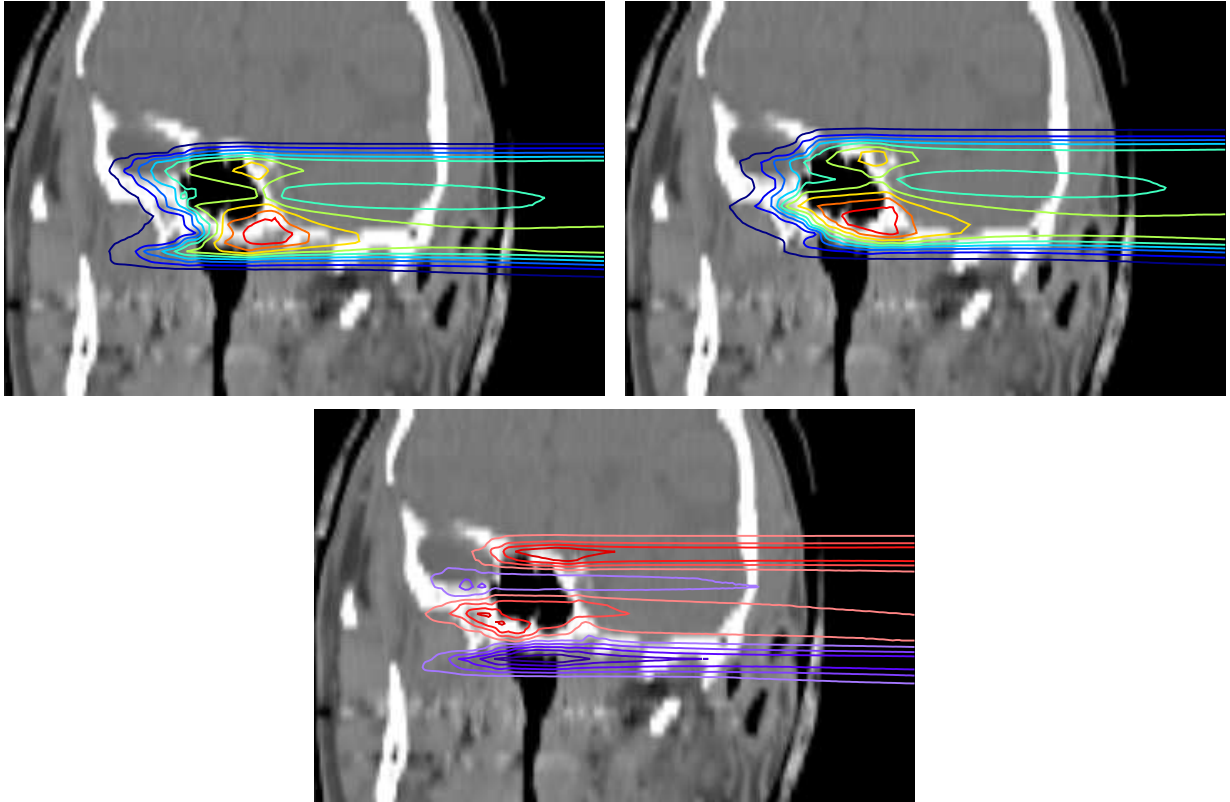
Figure 3–8: *Top: Prescribed dose distribution (left) in comparison to the recalculation following the conjectured caudal shift (right) for the considered case (a). The coloured isodose lines (5...95%) are normalised to the global maximum of 580 mGy in both cases. Bottom: Difference between the recalculated and planned dose. The red and blue coloured isolines correspond to positive and negative differences found to amount to 328 mGy and -326 mGy at maximum, respectively.*

3.3 Clinical results and outlook

Dose distributions recalculated on the basis of interactively manipulated X-ray CT cannot be expected to agree fully with the real dose delivered to the patient. Nevertheless, the described approach offers a valuable tool providing the radio-oncologist with an indicative but quantitative estimation of possible dose deviations detected on the basis of the PET monitoring. According to the entity of the modification, the radio-oncologist may decide whether to initiate more carefully investigations (e.g. a new CT scan when anatomical modifications are suspected) and eventually define new treatment strategies before delivering the successive irradiation fraction.

In both of the two presented clinical cases, the described conjectures were assessed by further investigations following the PET indication. A suboptimal position of the patient (case a) in the considered treatment fraction was revealed by a more accurate inspection of the orthogonal X-ray verifications taken prior to the dose application. A caudal shift of about 2 mm is visible in the antero-posterior (AP) image in comparison to the reference position (figure 3–10), though the real mispositioning might have been more complex than a simple translation, e.g. connected with some rotation of the patient head inside the mask. The considerable tissue reduction indicated by the ion over-range in case b was confirmed by a new CT scan, as shown in figure 3–11. The latter case of tissue modification is often plausible for patients which have been subject to surgery intervention prior to the radiotherapy, in addition to other possible factors
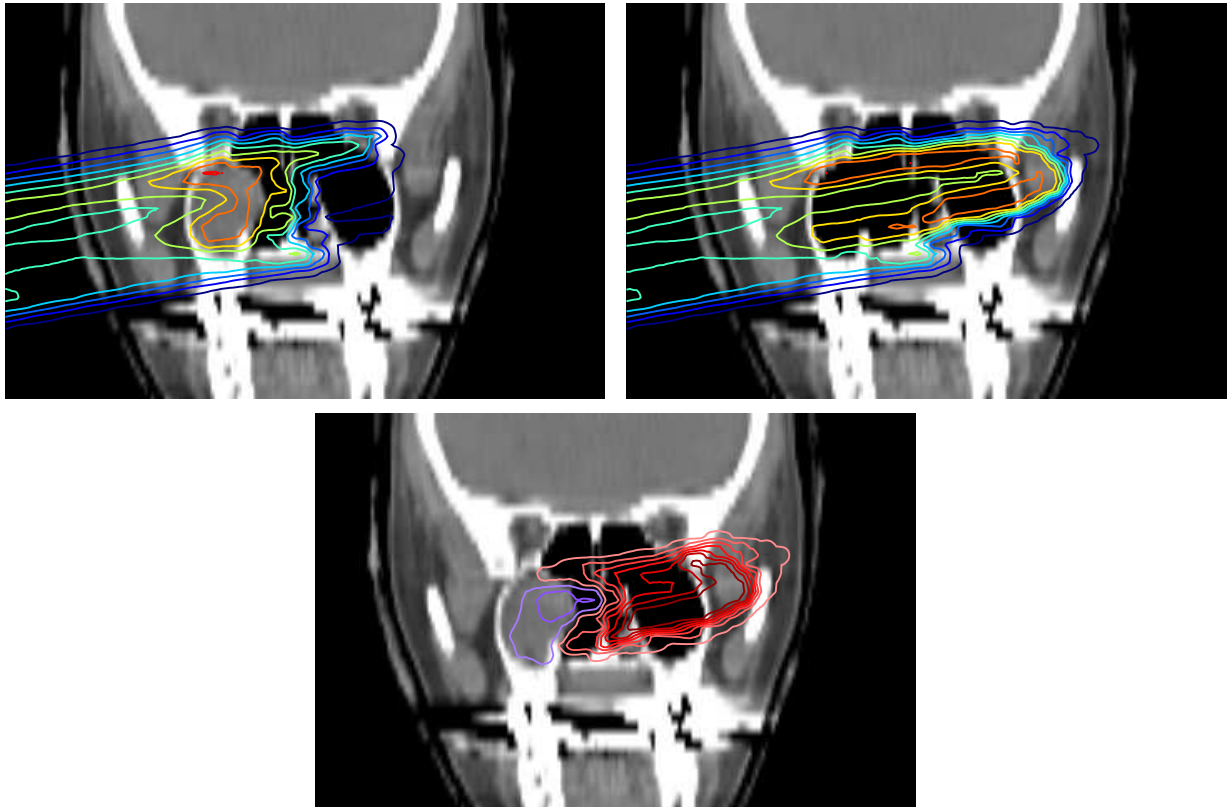
Figure 3–9: *The same comparison as in figure 3–8 between the planned (top, left) and recalculated dose distribution with the modified CT (top, right) for the examined case (b). The maximum dose values of the original and recomputed fields were about 650 mGy. The maximum and minimum values for the difference between the recalculated and planned dose distributions (bottom) were found to be 495 mGy and -200 mGy.*

related to the patient physical condition during the period of therapy (e.g. presence of mucus in respiratory cavities). Up to December 2003 6 patients out of 205 have been exposed to a new X-ray CT investigation triggered by the PET monitoring. In 5 cases the investigation confirmed a local anatomical change and for one of these patients a new treatment plan was elaborated. The remaining false positive was attributed to another anatomical modification resulting from the fold of the insensitive ear lobe of the patient when entering the fixation mask. In all the observed cases of deviations, no serious clinical consequences were encountered. In fact, proper safety margins and careful selection of the beam portals are currently taken into account in treatment planning in order to avoid too delicate irradiation fields. However, the proven detectability of positioning inaccuracies or anatomical changes in combination with the possibility of local dose quantification for a prompt intervention in fractionated radiotherapy might allow to consider in future reduced safety margin for more delicate irradiation fields.

For sake of objectivity, it has to be pointed out that the information on misalignments or tissue modifications underlying the described method in routine use for dose monitoring is not exclusive of PET. The new techniques of image guided radiotherapy [Jaf02] have to be mentioned in this context. By combining X-ray imaging with radiotherapeutic devices it has become feasible to take an X-ray CT of the patient in treatment position before applying a dose fraction and, furthermore, to obtain real time position information by exposing X-ray projections during the therapeutic irradiation. The latter issue is of utmost importance for tumour sites subject to the problem of organ motion. Without entering the discussion whether the improved accuracy of these techniques justifies the increased radiation burden to the patient, the still unique value of
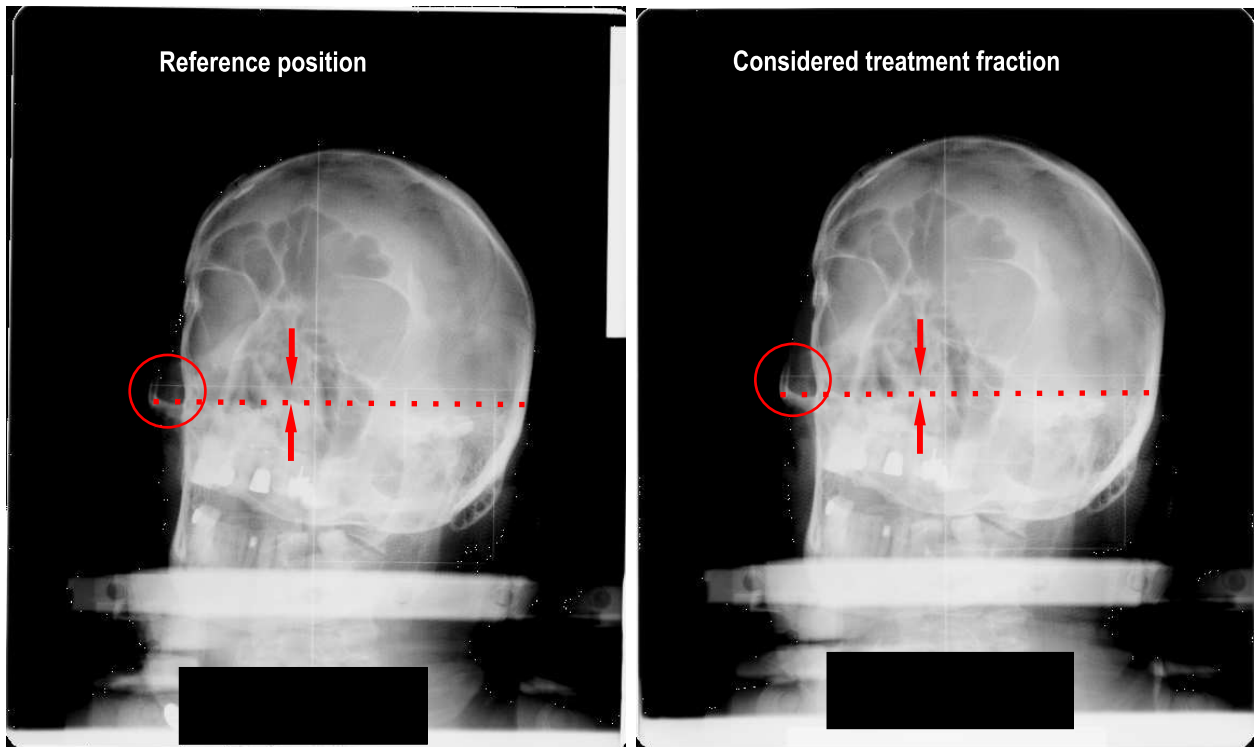
Figure 3–10: *Left: Reference AP X-ray verification film of the treatment position. Right: X-ray image taken before starting the irradiation of the considered treatment fraction for which PET indicated a suboptimal positioning. A caudal shift of the patient of almost 2 mm with respect to the reference position was deduced from the film projections. Such a small deviation, difficult to be assessed by eyes in the shown images without any dedicated imaging tool, was e.g. indicated by the distance between the horizontal steel wire of the cross-hair mounted on the film cassette holder to mark the isocentre (upper arrow) and the position of anatomical structures close to the nasal region like the cheekbone marked by the circle (cf. also dotted line and lower arrow). However, further analysis indicate a more complex mispositioning connected also to a rotation of the patient head within the fixation mask.*
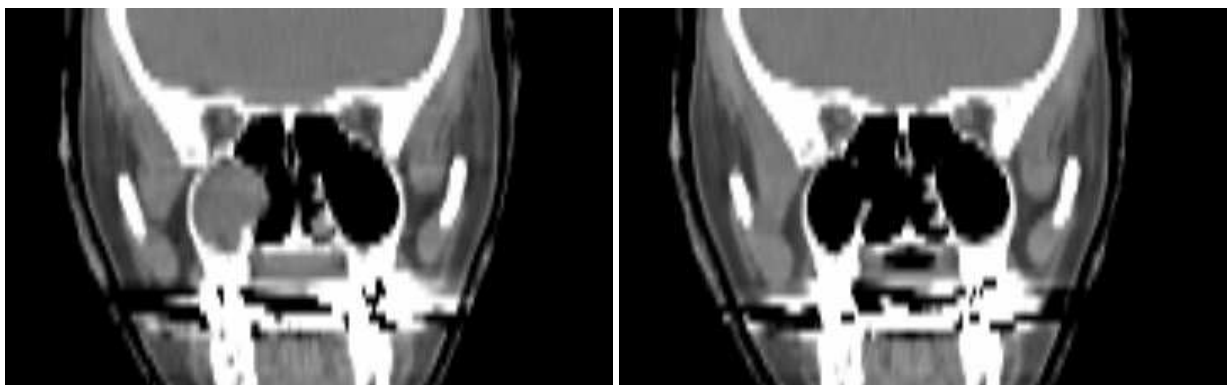
Figure 3–11: *Left: X-ray CT taken few weeks before starting fractionated carbon ion therapy for treatment planning purposes. Right: X-ray CT taken after a therapeutic session on the basis of the PET indication.*

PET in charged particle therapy has to be stressed. In-beam PET represents the unique available method for in-vivo, non-invasive monitoring of the ion range. In addition, it is the only currently known technique allowing to validate in-vivo the beam models implemented in the treatment planning algorithms as well as

33

the whole chain between treatment planning and irradiation. Furthermore, it does not require any additional radiation exposure beyond the application of the therapeutic dose. Therefore, PET is still expected to play an essential role in assuring the potential high precision of particle therapy, especially when starting up a new treatment facility or introducing into clinical routine new ion species. Finally, the whole potential of in-beam PET for a direct dose quantification solving the inverse problem from β^+-activity to dose and for an eventual ambitious access to the tumour response during fractionated therapy has not been yet exploited. With this respect one of the major limitations of the present state of the art is the extremely low counting statistics of the PET images. Hence, this issue is strictly connected to the investigation reported in the next chapter.

4 Random coincidences during in-beam PET

4.1 Motivation

The counting statistics of PET imaging for the monitoring of tumour therapy with stable ion beams is constrained by the relatively small amount of β^+-activity induced by the irradiation, estimated to be about $200\,\mathrm{Bq\,Gy^{-1}\,cm^{-3}}$ for typical therapeutic doses of $0.5 - 1\,\mathrm{Gy}$ per field in the carbon ion case [Eng04a]. Such a low signal demands a highly efficient utilization. Currently, the major limitation to this purpose is the low detection efficiency due to the small solid angle of about $8\,\%$ of the limited angle in-beam positron camera in use at GSI. A further important factor addressed in this chapter is the development of data acquisition schemes which are optimal for in-beam PET. The installation at the GSI facility, however, relies on the adaption of data acquisition methods originally developed for radiotracer imaging in nuclear medicine to the special application of in-beam PET. A high coincidence rate is systematically observed in the data acquired in the time during particle extraction (spill) from the synchrotron, as shown in figure 4–1. These events have been demonstrated to deteriorate the image quality and are therefore considered to be corrupted by a high noise level [Eng99a]. Similar problems were also described in [Lla88] for the unresolvable response of the scintillation detectors of their planar camera during beam extraction at LBL. The time dependence of the increased coincidence rate seen by the PET scanner during the beam pulses (figure 4–1, right) is clearly correlated in shape with the intensity variation of the slowly extracted ion beam from the GSI synchrotron over the spill [For98]. Hence, most of these coincidences are expected to originate from fast (at least in the sub-second scale) processes following the beam intensity. They are attributed to the decay of β^+-emitters with half-lives in the millisecond range and correspondingly high β^+-endpoint energies or to γ-rays following nuclear reactions and generating random coincidences. In contrast to the representation of figure 2–11 (middle), these random coincidences are ascribed to predominantly uncorrelated (in direction or time) photons not generated by positron annihilation after β^+-decay and, furthermore, not necessarily
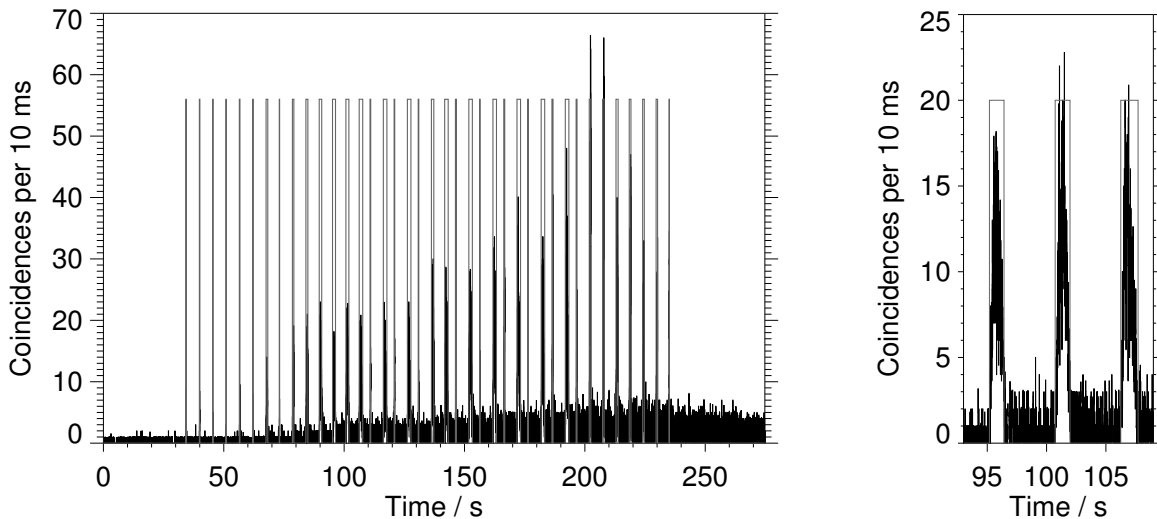
Figure 4–1: *Left: Example of coincidence rate acquired in list mode (with time stamps every 10 ms) by the in-beam positron camera during the delivery of an entire treatment field to a patient at GSI. Right: Enlarged view for a subset of the same measurement. The rectangular pulses indicate particle extraction. The count rate increase during the spills as well as the β^+-activity decay in the pauses between the pulses is evident.*

produced within the field of view of the detector. Coincidences originating from the decay of short-lived positron emitters or from beam induced single γ-rays tend either to broaden the spatial distribution of the induced β^+-activity because of the longer positron range (cf. section 2.3.1) or do not bear information on the dose localisation. At present, these events cannot be separated from the usable decays of long-lived emitters with half-life $T_{1/2} > 1\,\text{s}$, which generate the build-up of activation visible in the time dependence of the coincidence rate acquired within the beam pauses in figure 4–1, left. Therefore, all coincidences detected during beam extraction are currently discarded from the image reconstruction [Eng99a]. With the present irradiation scheme, consisting of a maximum of 2 s particle extraction followed by a pause of about 3 s for a total fixed repetition cycle of about 5 s, the rejection of the in-spill data can be estimated to reduce the counting statistics up to $40\,\%$ (i.e. $2\,/\,5$). This rough calculation assumes a constant count rate over the beam spills and pauses and takes into account only the decay of long-lived positron emitters. The situation is expected to become even worse in the dedicated Heidelberg facility, where a more efficient utilisation of the accelerator in combination with the next generation ion beam raster scanner is estimated to shorten the fraction of total beam pauses during the treatment by about $20\,\%$ and, in addition, to reduce the overall treatment time from an average of 250 s to 90 s [Hab00]. In fact there is no clinical as well as practical advantage in prolonging the treatment time just in order to improve the quality of the PET images. Therefore, an alternative solution for the next generation in-beam PET scanner has to be found in order to suppress the noise during beam extraction and recover the usable signal from the decay of the long-lived positron emitters of interest for the monitoring. As a pre-requisite for such a development, a deeper insight into the physical reason underlying the noisy in-spill data acquisition is mandatory. This issue has been addressed in the series of experimental investigations presented in the following sections. This work is the basis for a new concept of data acquisition tailored to in-beam PET [Eng04b, Cre04].

4.2 The indication from in-beam PET data

4.2.1 Experimental observations

In order to investigate the conjectured role of γ-rays originating from nuclear reactions induced by the beam and not related to β^+-decays (addressed in the further text as "beam induced background") on the noisy in-spill PET acquistion, the following initial experiments were performed. Mono-energetic carbon ion beams of fixed intensity were partially or completely stopped in $9 \times 9 \times 20\,\text{cm}^3$ blocks of polymethyl methacrylate (PMMA) placed with the long edge perpendicular to the beam at a distance $x \in \{-30, 21, 71, 121, 171\}\,\text{cm}$ from the centre of the field of view (FOV) of the PET scanner, coinciding with the isocentre of the treatment unit (figure 4–2). This configuration allows to substantially reduce or rule out the contribution to the measured events coming from β^+-decays due to the position of the activated target outside the positron
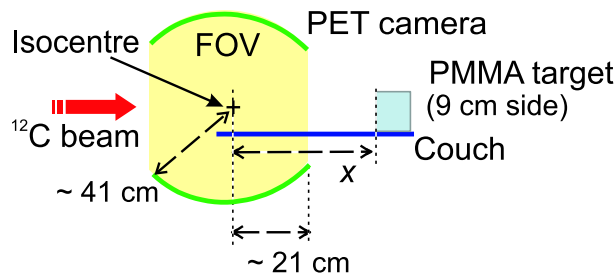
Figure 4–2: *Experimental set-up for the investigation of the coincidence rate measured by the positron camera during beam extraction without any β^+-activity source in the marked field of view of the tomograph.*
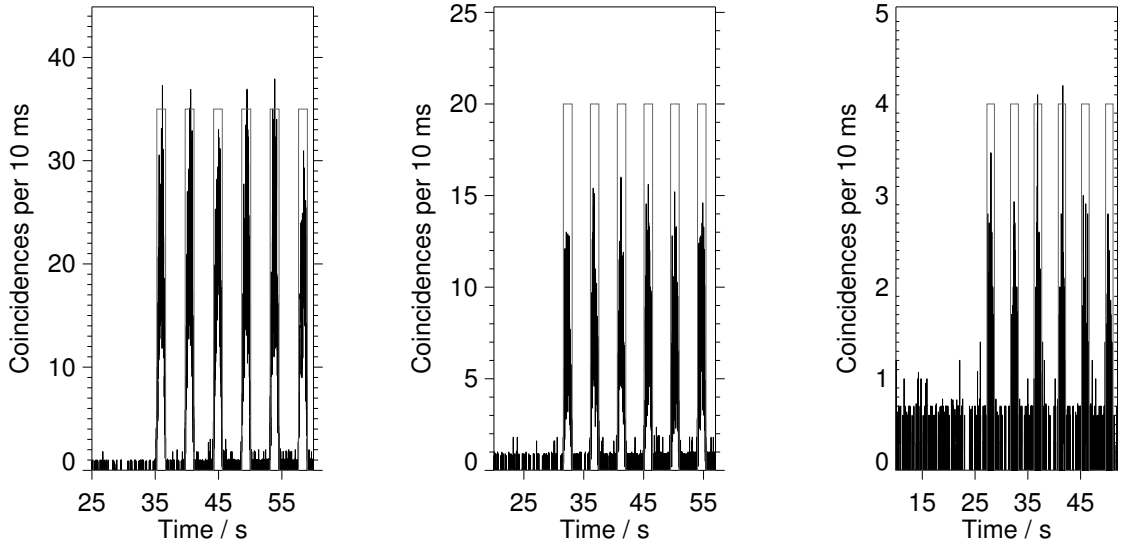
**Figure 4–3:** *True coincidence rate acquired by the positron camera in the same condition of ^{12}C irradiation (energy: 280.48 AMeV, intensity: $2 \cdot 10^7$ ions spill^{-1}) but different phantom position x of –30 cm (left), 21 cm (middle) and 171 cm (right).*

camera FOV. Nevertheless, a non zero coincidence rate was measured during particle extraction, whereas the activity level correctly drops to zero as soon as the particle extraction stops (figure 4–3). Moreover, the intensity of the beam induced signal was found to depend not only on the distance of the target from the detector, but also on its relative position with respect to the beam direction. In particular, the about 3 times higher count rate registered at a position $x = -30$ cm against $x = 21$ cm in the same irradiation condition suggests a strong background component in the forward emission cone, e.g. due to in-flight de-excitation of projectile fragments or pair production processes. Because of the absence of β^+-activity sources in the field of view of the tomograph, all these observations lead to the conclusion that the increased coincidence rate during the beam pulses is due to random coincidences not properly corrected for by the positron camera. The effect must be furthermore related to the time dependence of the beam intensity. A proper random correction was observed when placing a 80 MBq positron emitting ^{68}Ge source producing a stationary γ-ray background at similar distances x from the centre of the FOV. A plausible conjecture on the reason for the failure of the random correction approach in presence of particle extraction as well as a first validation of this assumption on the basis of the described experiments is given in the next subsections.

4.2.2 The method of random correction and its failure due to the beam microstructure

For the sake of clarity the definitions of prompt, true and random coincidences extensively used in the following and already addressed in section 2.3.1 are here briefly reminded. Prompt coincidences P are events generated by photon pairs of energy within a given acceptance interval firing opposite crystals in a prompt coincidence time window. A subset of these coincidences originate from photon pairs belonging to the same annihilation event and are therefore addressed as true coincidences T. The remaining fraction is ascribed to photon pairs not originating from the same annihilation event or even not related to β^+-activity decays but accidentally falling in the valid time and energy windows for prompt coincidence detection. Therefore, these are called random coincidences R. Hence, the recovery of the true signal requires a correction for
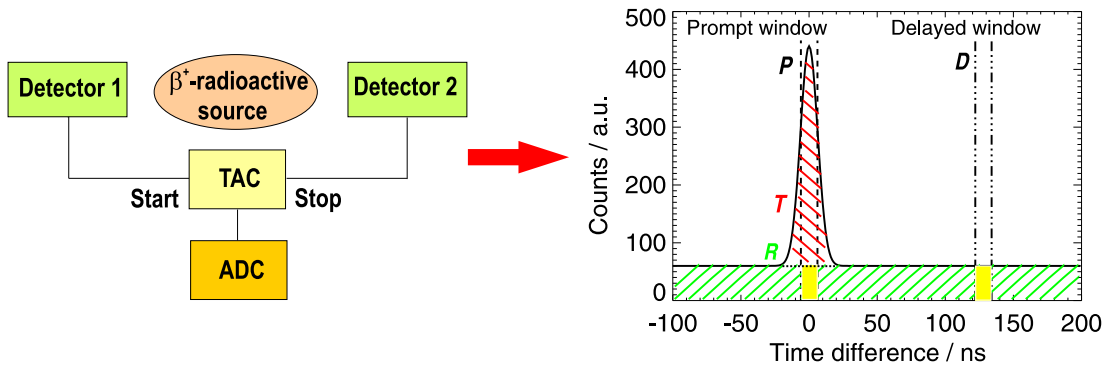
Figure 4–4: *Typical coincidence spectrum recorded with a time-to-amplitude-converter (TAC) and an analog-to-digital-converter (ADC) when placing a β^+-radioactive source in the field of view of two detectors. The indicated true T, prompt P, random R and delayed D coincidences are explained in the text.*

random coincidences. The standard random correction technique implemented by the manufacturer of the data acquisition system of the in-beam PET scanner (CTI PET Systems Inc. Knoxville, TN, USA) is based on the subtraction of coincidences detected in a 128 ns delayed window (delayed coincidences D) from all the prompt coincidences generated by photon pairs within the chosen energy window ($250 - 850$ keV). Both of the prompt and delayed windows are of the same width (12 ns). The basic assumption underlying such an approach, always fulfilled in radiotracer imaging, is a γ-ray flux being constant over the delay time and generating an approximately constant random coincidence rate superimposed onto the true signal (figure 4–4). Obviously in this condition the amount of delayed coincidences D taken in a time window properly shifted far away from the desired true signal is a very good approximation of the number of random coincidences R falling within the prompt window and contributing to the total amount of prompt coincidences P detected. Hence, the true signal within the prompt window $T = P - R$ can be rather well recovered as $T = P - D$. However, a variation of the γ-ray flux on the time scale of the shift between the prompt and delayed coincidence window will lead to a wrong estimation of the amount of random coincidences superimposed onto the true signal.

During in-beam PET a non-stationary γ-ray background in the sub-microsecond time scale can be attributed to the micropulsed structure of the beam. Accelerators for ions as well as conventional electromagnetic radiation sources do not accelerate particles continuously but in packages (bunches) separated in time from some hundreds of nanoseconds (synchrotrons and cyclotrons for ions) to some hundreds of picoseconds (linear accelerators for electron and photon radiotherapy) corresponding to the MHz or GHz operation region of the accelerating radiofrequency (RF) cavities, respectively. According to the parameters of the heavy ion synchrotron SIS of GSI as well as the 4th harmonics acceleration scheme (i.e. four bunches circulating in the ring are accelerated by one RF cavity), the periodical repetition of the micropulses varies from 450 ns to 250 ns in the $88 - 430$ AMeV energy range used for carbon ion therapy. This bunched structure is not destroyed during the extraction procedure because the chosen approach was demonstrated to provide a beam with reduced intensity fluctuations for optimal coupling to the raster scanning system.

In a first approximation the beam induced background radiation can be assumed to be correlated in time to the carbon ion microstructure, due to the typically fast (with respect to the nanosecond time scale) secondary particle production and prompt γ-ray emission processes following nuclear reactions. A model for such a background based on a realistic description of the beam microstructure with bunches of Gaussian shape is depicted in figure 4–5. The period of the modulation and the width of the Gaussian bunches directly reflect the beam microstructure, related to the accelerator RF and to the beam momentum spread resulting from the longitudinal phase compression, respectively. The bias accounts for a delayed γ-ray component
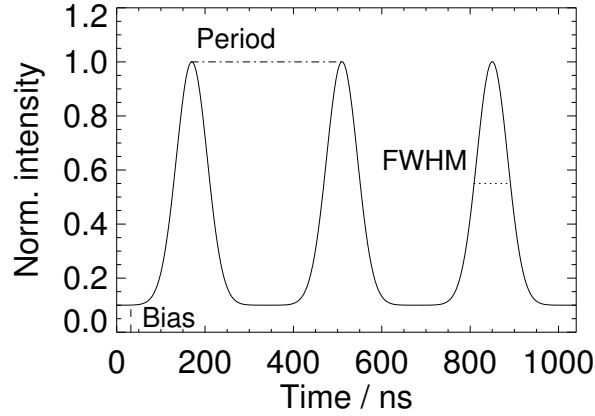
Figure 4–5: *Model of a γ-ray background varying in time according to the carbon ion beam microstructure.*

due to the decay from isomeric excited nuclear states or radioisotopes with half-lives larger than several hundreds of nanoseconds. Depending on the model parameters, the modulation can result in a reduction of the delayed coincidence rate leading to an underestimated random correction responsible for the increase of noise in the data acquired during particle extraction. This is illustrated in figure 4–6 for calculations of the ratio between the average delayed and prompt random coincidence rates per second generated by the modelled single γ-ray background at a given period in dependence on the width of the Gaussian bunches at a fixed bias or vice versa. The simulated values were obtained from the times of detection of single γ-rays randomly distributed on two detectors according to a probability density function resembling figure 4–5. In analytical calculations the average prompt and delayed random coincidence rates induced by a flux of photons distributed in time according to the same probability density function $f(t)$ was estimated as:

$$P = \frac{1}{T_{\mathrm{RF}}} \int_0^{T_{\mathrm{RF}}} \left(\frac{1}{\tau} \int_{\bar{t}}^{\bar{t}+\tau} K_1 f(t)\mathrm{d}t \int_{\bar{t}}^{\bar{t}+\tau} K_2 f(t)\mathrm{d}t \right) \mathrm{d}\bar{t}$$

$$D = \frac{1}{T_{\mathrm{RF}}} \int_0^{T_{\mathrm{RF}}} \left(\frac{1}{\tau} \int_{\bar{t}}^{\bar{t}+\tau} K_1 f(t)\mathrm{d}t \int_{\bar{t}+\Delta\tau}^{\bar{t}+\Delta\tau+\tau} K_2 f(t)\mathrm{d}t \right) \mathrm{d}\bar{t}$$

(15)
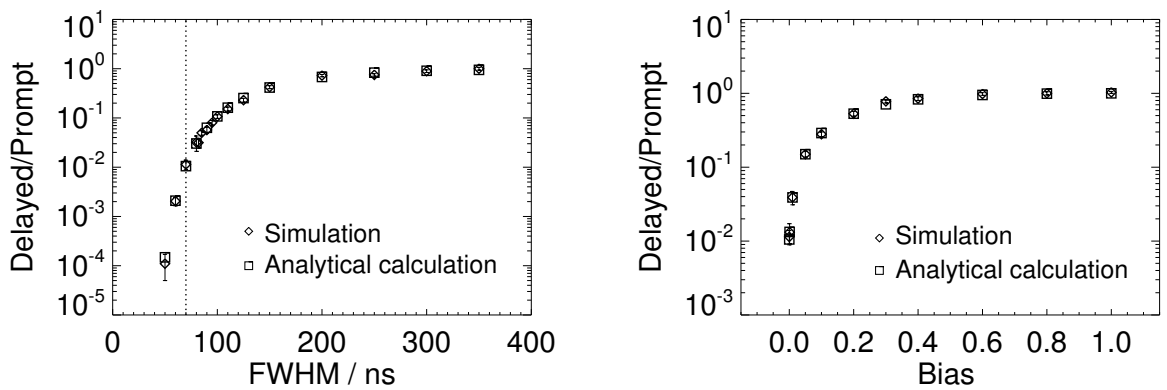
Figure 4–6: *Ratio of delayed and prompt coincidences induced by a background of uncorrelated γ-rays modulated in time according to the model of figure 4–5. The data were obtained from Monte Carlo simulations and analytical calculations at a period of 340 ns in dependence on the width of the Gaussian bunches with no bias (left) and on the bias at the FWHM value of 70 ns marked by the dotted line in the left panel (right).*

39

where K_1 and K_2 are normalisation factors to the count rates of photons hitting the two camera heads, τ is the 12 ns width of the coincidence window, $\Delta\tau$ is the 128 ns time shift of the delayed window and T_{RF} is the modulation period. For an uniform probability density function $f(t) = 1$ the two formulae reproduce the known expectation of random coincidences induced by stationary single count rates K_1 and K_2 [Wie89]:

$$P = D = R = K_1 K_2 \tau \qquad (16)$$

In equation (15) the time dependent prompt and delayed coincidence rates were averaged over one modulation period, since the coincidences acquired by the positron camera are always separated on a temporal scale comparable to T_{RF} due to the 256 ns period of the master clock of the coincidence processor [New89]. Furthermore, a limited number of photons per modulation period is expected because of the low amount of primary carbon ions in the same time interval at the typical intensities of about $10^7 - 10^8$ ions s^{-1} used for therapy. However, these intensity values still provide enough single events per RF period in order to observe the effect of the modulation for coincidence detection. A first validation of the presented γ-ray background model on the basis of the coincidence rates measured by the in-beam positron camera in the previously described experiments is addressed in the next subsection.

It should be remarked there is a second known technique of random correction in addition to the described method based on the measurement of delayed coincidences. This alternative solution implemented in other commercial PET scanners is based on the measurement of the single γ count rates and equation (16). However, for each detector the single count rate information is collected over several seconds in order to reduce the statistical error. Since this time interval corresponds to millions of modulation periods any possibility of synchronization with the time of detection of the prompt coincidences affected by the time variant random background is completely lost, hence resulting in a faulty random correction. Therefore, standard available techniques for correction of random coincidences based on measurements of delayed coincidences or single γ count rates fail in presence of a γ-ray background being non-stationary in the sub-microsecond time scale.

4.2.3 A first validation of the conjectured influence of the beam microstructure

The list mode data acquisition of the positron camera allows for the distinction of prompt and delayed coincidences detected in 10 ms wide intervals during beam extraction and extraction pauses (figure 4–7). From these values average prompt and delayed coincidence rates per second P_s, P_p and D_s, D_p – the subscripts s and p refer to "spill" and "pause", respectively – were calculated for each spill and pause. The
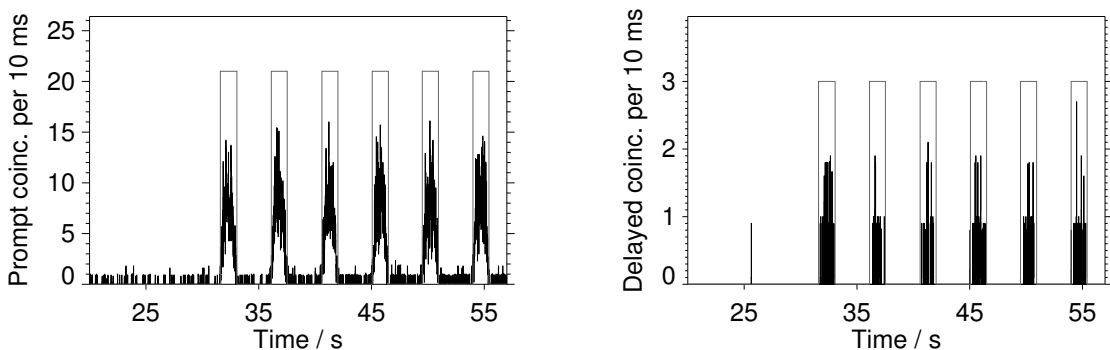

Figure 4–7: *Separate prompt (left) and delayed (right) coincidence rate for a 280.48 AMeV carbon ion irradiation at a phantom position x = 21 cm.*
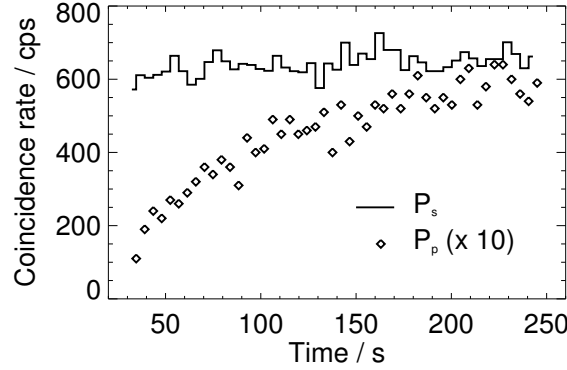
Figure 4–8: *Average prompt coincidence rate per second (cps) during particle extraction (P_s) and beam pauses (P_p) for the same irradiation (cf. figure 4–7) with the target at the edge of the scanner FOV. The activity build-up due to the small contribution from long-lived positron emitters is visible in the growth of P_p with the time of irradiation.*

observed high prompt and delayed coincidence rate during particle extraction (P_s and D_s, respectively) is conjectured to originate mostly from the beam induced γ-ray background in addition to the true contribution from the decay of short-lived ($T_{1/2} \ll 1\,\mathrm{s}$) as well as long-lived β^+-emitters in case of activity sources within the FOV of the positron camera. The latter long-lived positron emitters represent the almost exclusive source of a detectable signal during the extraction pauses. For the analysis of the experiments described in section 4.2.1 the beam induced background component, addressed in the following with the index r staying for "random", had to be separated from the measured total P_s and D_s count rates. The following approach was applied. The contribution to P_s and D_s from short-lived isotopes of typical half-lives in the ms time scale was neglected in first approximation. If detectable in dependence on the phantom position, short-lived emitters are very roughly estimated to contribute to the coincidence rate in spill in the same order of magnitude of the long-lived isotopes formed in the same spill, due to the compensation between their small production cross section and their larger decay constant. Hence, on the basis of the observed strong count rate variation between particle extraction and extraction pauses in figure 4–7, the contribution of short-lived positron emitters to P_s and D_s is expected to be rather small in comparison to that induced by the beam. Moreover, such short-lived isotopes almost entirely decay within the spill in which they are produced. Thus, their neglection can affect the final estimation of the beam induced random coincidence rate only by a constant offset in each spill. On the contrary, the contribution to P_s and D_s from long-lived β^+-emitters varies with the time of the irradiation because of the activity build-up process (figure 4–8). Therefore, this component was subtracted by means of an extrapolation from the corresponding prompt (P_p) and delayed (D_p) count rates measured in the successive extraction pauses. Hence, the beam induced prompt and delayed coincidence rate per second was estimated for each spill as $P_r = P_s - P_p$ and $D_r = D_s - D_p$, respectively. The resulting ratio of the delayed and prompt beam induced coincidence rates, averaged over all the spills of the irradiation, was observed to be rather independent on the target position outside the FOV and on the beam energy at the considered typical intensities of $10^7 - 10^8\,\mathrm{ions\,s^{-1}}$. The latter values corresponded to prompt count rates in spill P_s from 100 to 1500 cps at the selected distances x. An average ratio $\langle D_r/P_r \rangle = (0.040 \pm 0.008)$ was extracted from measurements performed at different days and with different irradiation parameters (figure 4–9). It should be noticed that a proper random correction should result in a $\langle D_r/P_r \rangle$ ratio of one.
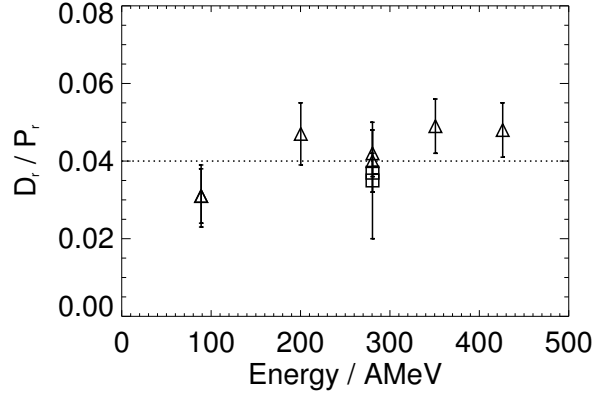
Figure 4–9: *Ratio of the beam induced average delayed and prompt coincidence rate estimated from several in-beam PET experiments. Measurements at different energies corresponded to a phantom distance x of 21 cm (triangles). The additional values at the energy of 280.48 AMeV (squares) were found at different target positions x of –30 cm and 71 cm.*

A first validation of the γ-ray background model illustrated in section 4.2.2 was performed by means of the described Monte Carlo simulations, trying to reproduce the average beam induced delayed (D_r) and prompt (P_r) random coincidence rates extracted from the measured PET data. Since the results do not unambiguously depend on the selection of the bias and FWHM model parameters at a fixed modulation period corresponding to a given ion energy, the bias was set to 0. This choice allows to investigate the maximum width of the Gaussian bunches capable to reproduce the observed suppression of delayed coincidences (cf. figure 4–6). Indeed the experimental values could be reproduced by means of a proper choice of the maximum FWHM parameter (figure 4–10, left). However, at energies below 200 AMeV (figure 4–10, right) the predicted FWHM values were found to be considerably smaller than the measured widths of the beam bunches within the synchrotron ring before extraction [Eic00]. In order to interpret correctly the reasons for
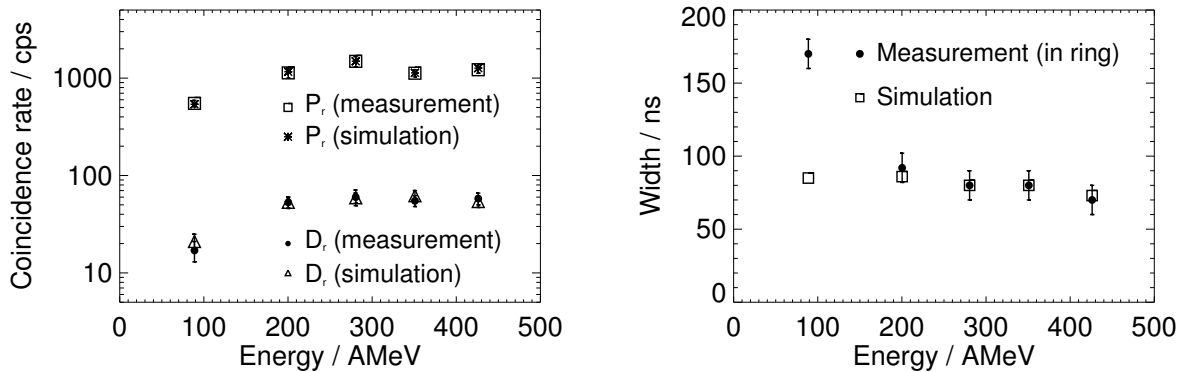
Figure 4–10: *Left: Beam induced average coincidence rates D_r and P_r extracted from PET measurements at different initial energies at $x = 21$ cm in comparison to Monte Carlo simulations based on the model of figure 4–5 at the period corresponding to the given ion energy and with no bias. Right: Predicted FWHM values leading to the simulated data presented in the left panel in comparison to the FWHM of the beam bunches measured in the synchrotron ring before extraction. The disagreement for low energies is evident.*

this disagreement, the microstructure of the carbon ion beam had to be assessed after the extraction and as much as possible close to the position of the PET scanner. The experiment addressing this issue is presented in the next section.

4.3   The time microstructure of the carbon ion beam

The residual microstructure of the carbon ion beam after slow resonant extraction in the same condition used for therapy (i.e. applying a flat top voltage of $2\,kV$ to the RF tank) was measured by means of a standard plastic scintillator (BC400, decay time of about $2\,ns$) of $75 \times 75\,mm^2$ surface and $1\,mm$ thickness placed in the beam line of the medical cave, $50\,m$ downstream of the SIS exit and about $100\,m$ in front of the PET camera (figure 4–11). The detector was coupled to a fast photomultiplier (PMT, Phillips XP2972), resulting in pulse widths less than $10\,ns$. A fast digital storage oscillograph (DSO, $1\,GHz$ maximum sampling frequency) was used to acquire the PMT pulses simultaneously to the sinusoidal signal coming from the RF cavity. Data were sampled either at 1 or $5\,ns$ separation for a total of 4 or $20\,ms$ acquisition time, respectively. A relatively low amount of 10^6 ions per acceleration cycle was produced in the SIS ring prior to the extraction in order to limit as far as possible pile-up in the scintillation detector. An example of acquisition is given in figure 4–12. As indicated by the vertical dotted and dashed lines, the arrival time of the particles on the detector was identified either with the leading edge position obtained from the derivative of the PMT signal or with the pulse maxima (inverse polarity) position. In the latter case single and piled-up events could be distinguished by analysing the pulse amplitude and width, because of the rather constant shape of the signal induced by mono-energetic carbon ions in the used thin scintillator. Both of the approaches provided similar results. A rather good time resolution was obtained due to the steep and constant rise time of the signal. However, the maximum achievable resolution is limited by the finite sampling period of the digital oscillograph, comparable to the rise time of the scintillator signals. The final time distributions were obtained by relating all the events to one RF period, exploiting the phase and period information given by the RF signal. As indicated by figure 4–13, the particle arrival times exhibit a strong correlation with the phase of the RF signal. The observed phase of maximum occurrence probability varies in dependence on the particle energy because of the different transit time of the ions to the detector with respect to the constant delay of the signals fed to the scope via a cable of fixed length. The measured microstructure rather well supports the approximation of beam bunches of Gaussian shape, in spite of a very slight asymmetry which increases with the beam energy, as visible in figure 4–13. The average FHWM values obtained from least squares Gaussian fits of all the performed experiments are summarised in table 4–1. The broadening trend at lower energies is due to the larger momentum spread, in analogy to the previous values measured in the synchrotron
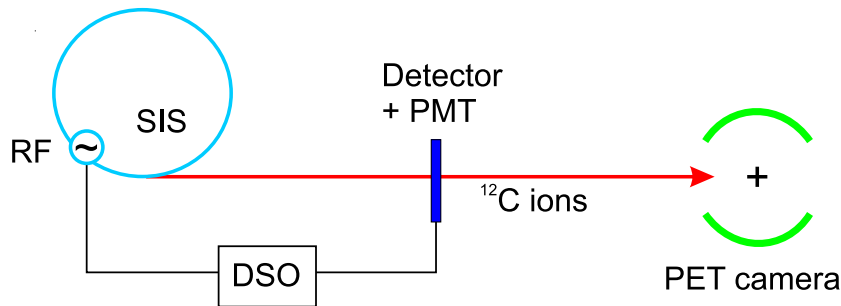

Figure 4–11: *Experimental set-up for the measurement of the carbon ion beam microstructure after extraction in the beam line downstream from the SIS synchrotron and 100 m before reaching the medical cave where the PET camera is installed.*
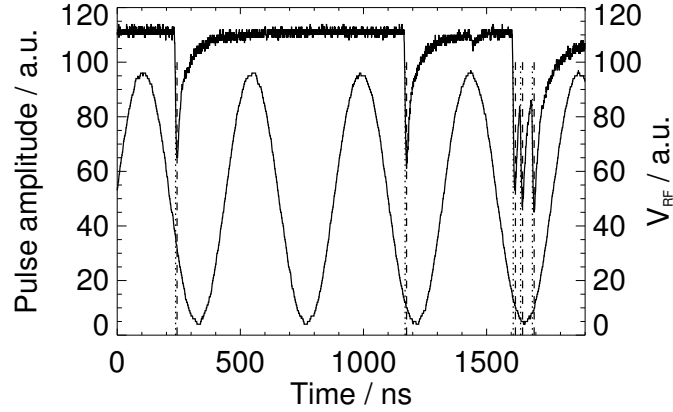
Figure 4–12: *Example of the scintillator and RF signals acquired for an irradiation at 88.83 AMeV ion energy (T_{RF} = 442.8 ns). The arrival times of the ions deduced from the derivative or maxima (inverse polarity) of the scintillator pulses are shown by the vertical dotted and dashed lines, respectively.*

ring (cf. figure 4–10, right). However, the bunch widths measured after particle extraction are found to be much smaller than in the SIS ring. Moreover, these new values are well below the maximum FWHM values which were predicted by the simulations in order to explain the delayed coincidence suppression leading to the strong noise of the in-beam PET acquisitions. Hence, the experimental beam induced prompt (P_r) and delayed (D_r) count rates detected by the PET scanner (cf. figure 4–10 in section 4.2.3) could still be reproduced by simulations using the parameters of table 4–1, provided that a plausible bias of about 1 % was included in the model. Therefore, as a remaining validation step the γ-ray background reaching the positron camera detectors during particle extraction had to be measured, as addressed in the next section. It should be finally mentioned that due to a typical beam momentum spread of ± 0.1 % no debunching of the measured carbon ion microstructure can be expected in the $\simeq 100$ m distance between the location of the plastic scintillator and the PET camera in the explored full energy range used for therapy, corresponding to
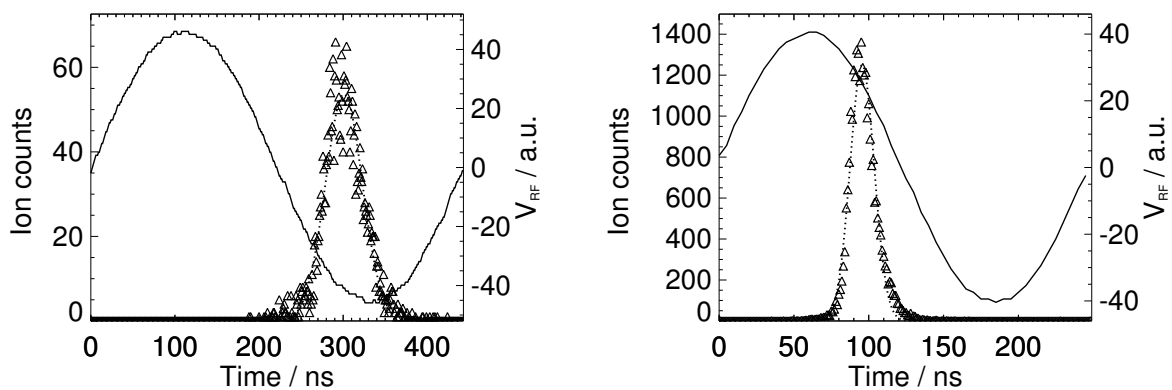
Figure 4–13: *Time correlation of the particle arrival with respect to the phase $\varphi = 0$ of the synchrotron RF signal measured at an ion energy of 88.83 AMeV (left) and 426.11 AMeV (right). The left axis refers to the ion counts (triangles), whereas the right axis refers to the sinusoidal voltage applied to the RF tank (solid line). The Gaussian fit of the measured count distribution is shown by the dotted line.*

Table 4–1: *Average FWHM values from least squares Gaussian fits of all the ion-RF time correlation distributions measured after particle extraction at different energies corresponding to different RF periods.*

Energy / AMeV	RF period / ns	FWHM / ns
88.83	442.8	55 ± 4
200.28	318.2	32 ± 3
280.48	282.4	28 ± 3
350.84	262.9	24 ± 2
426.11	248.4	19 ± 2

ion velocities within $0.4 - 0.7\,c$. Furthermore, Schottky spectra measurements excluded also any significant variation of the bunch widths at the higher intensities of $10^7 - 10^8\,\text{ions}\,\text{s}^{-1}$ usually applied for therapeutic irradiation [Mor00].

## 4.4   The measured γ-ray background

In order to assess the conjectured failure of the random correction of in-beam PET coincidences acquired during particle extraction because of a non-stationary γ-ray background correlated in time to the carbon ion beam microstructure, time spectra of the γ-rays originated by ^{12}C bombardment of organic matter relative to the synchrotron radiofrequency had to be measured. Since it is impossible to operate the PET camera for such an investigation, a detector of similar stopping properties as bismuth germanate (BGO) but better timing performances was chosen. These requirements are rather well fulfilled by gadolinium ortho-silicate (cf. table 4–2). Hence, a GSO crystal of 20 mm radius and 25 mm thickness (MolTech GmbH, Berlin) coupled to a fast PMT (Philips XP2020) was selected. This size allows a detection efficiency comparable to that of a single BGO block detector of the in-beam PET scanner to be achieved. In order to compare the timing and energy performances, GSO-BGO time coincidence spectra with additional spectroscopic analysis were measured with a ^{22}Na positron emitting source in a laboratory set-up resembling the scheme of figure 4–4. The GSO detector was estimated to have a 2.6 ns time resolution (FWHM) against the 5.3 ns of the available BGO sample. The energy resolution of the GSO detector was found to be about 15 % against the $\simeq 25$ % of the BGO crystal at 511 keV. These values support the choice of the GSO detector for the planned energy and time correlation measurement of the γ-ray background with respect to the RF signal. The experimental set-up as well as the data analysis and outcome are separately reported in the next subsections. As briefly addressed in the discussion of the results, an independent spectroscopic investigation of the beam induced γ-ray background was additionally performed with a Germanium detector of better energy resolution ($\simeq 3\%$ at 511 keV) in the same set-up of the GSO experiment.

Table 4–2: *Main properties of the inorganic scintillators bismuth germanate (BGO) and gadolinium ortho-silicate (GSO): effective atomic number Z_{eff}, density ρ, radiation length X_0, wavelength of maximum emission λ_{max}, refraction index n, fluorescence time constant τ (doping dependent for GSO), light output η relative to NaI(Tl) and radiation hardness $\mathcal{R}$. Both crystals are not hygroscopic.*

Scintillator	Z_{eff}	ρ / g cm^{-3}	X_0 / cm	λ_{max} / nm	n	τ / ns	η / %	$\mathcal{R}$ / Gy
$\text{Bi}_4\text{Ge}_3\text{O}_{12}$ (BGO)	75	7.13	1.12	480	2.15	300	$10 - 20$	10^{3-4}
Gd_2SiO_5:Ce (GSO)	59	6.71	1.38	440	1.85	$30 - 60$	$18 - 27$	$> 10^6$

4.4.1   Experimental set-up

For the experimental investigation of the beam induced γ-ray background, mono-energetic carbon ion beams spanning the energy range of therapeutic interest ($88.83 - 426.11\,A$MeV) were completely stopped in $9 \times 9 \times 20\,\text{cm}^3$ PMMA targets placed at the isocentre of the treatment unit with their long edges parallel to the beam (figure 4–14). This configuration well resembles typical irradiation conditions during therapy. Corresponding intensity values from $1 \cdot 10^8$ to $4 \cdot 10^6$ ions per about $2\,\text{s}$ spill were selected in order to achieve a similar dead-time of the data acquisition system [Ess00] for all beam energy values. The GSO detector coupled to the fast PMT was horizontally placed on the patient couch with the crystal centre aligned to the isocentre. The couch was mostly positioned perpendicularly to the beam. In few measurements the angle was varied in order to explore the angular dependence of the γ-ray flux with respect to the beam direction. The distance between the detector and the isocentre was kept fixed to $41\,\text{cm}$, approximately as the radius of the PET detector heads. This reproduces the exposure condition of the positron camera to the beam induced background radiation. For the measurement of the time distribution of the γ-ray flux with respect to a fixed phase of the synchrotron RF with additional photon energy discrimination the signal processing scheme shown in figure 4–15 and based on standard NIM and CAMAC electronics was used. The tunable blocking window of the constant fraction discriminator (CFD) in the time branch of the detector was used to prevent multiple triggering. The CFD trigger level was adjusted to a lower energy threshold of about $100\,\text{keV}$. The higher energy threshold resulting from the energy branch in combination with the ADC was about $3.4\,\text{MeV}$. The TAC settings were chosen in order to have a time range interval of almost $400\,\text{ns}$ comparable to the maximum RF period of about $450\,\text{ns}$. The signals from the accelerator control and beam monitor (ionisation chambers) were used in order to enable the acquisition exclusively during particle extraction (beam on). Besides the time and energy record, the following additional parameters were inserted into the list mode data stream. The spill number $C1$ was registered in order to perform dynamic acquisition for establishing the relationship between the single photon count rate detected by the GSO crystal and the prompt as well as delayed coincidence rates simultaneously recorded by the positron camera. $C0$ is the number of triggered events detected by the GSO crystal independently on the irradiation status (beam on/off), in the following distinguished as $C0_s$ and $C0_p$ for detection during the spills and pauses, respectively. This record in combination with $C1$ further enables a more straightforward comparison with the PET measurement during the pulsed beam delivery. The strobe signal of the ADC $C2$ provides additional
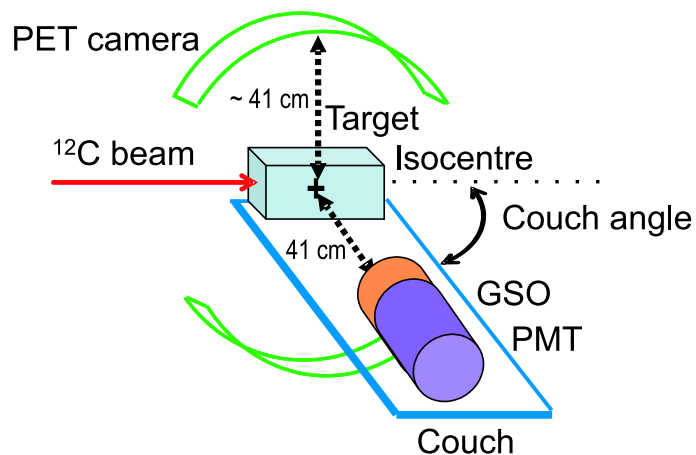
Figure 4–14: *Experimental set-up for the energy and time correlation measurement of the beam induced γ-ray flux with respect to the synchrotron radiofrequency.*
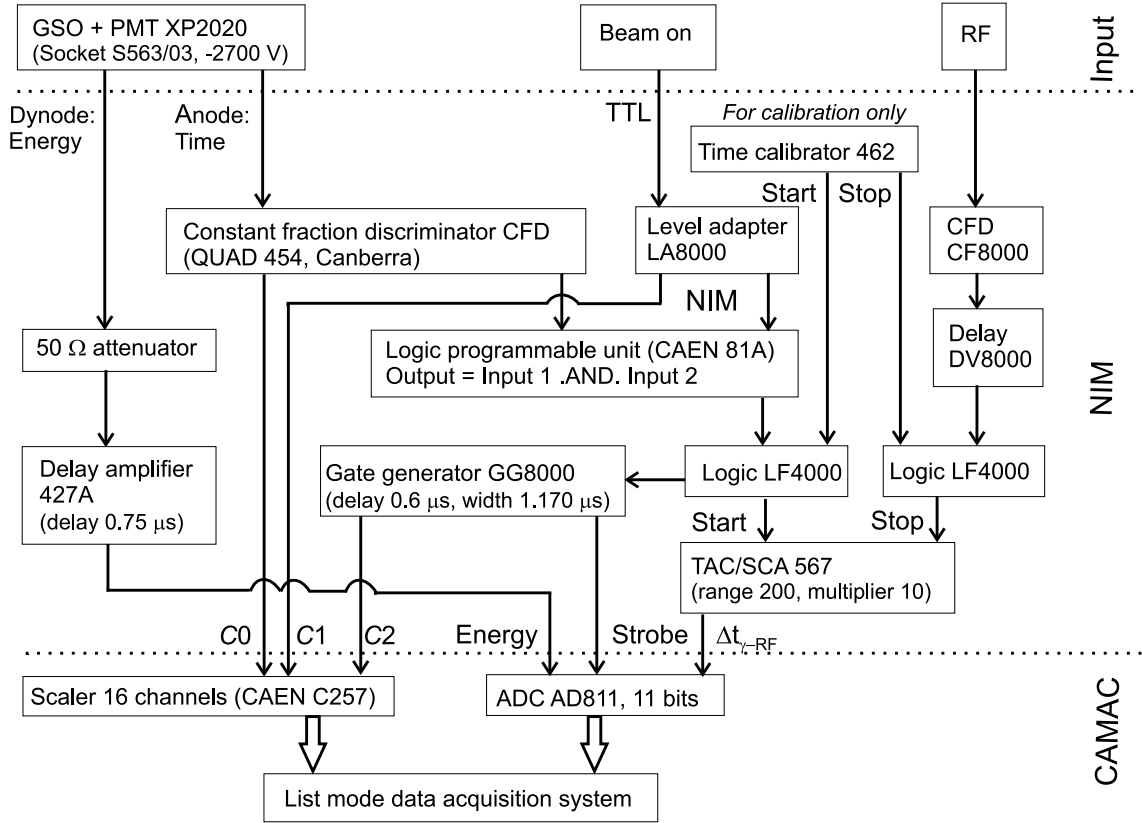
Figure 4–15: *Scheme of the NIM and CAMAC electronics used for the RF-γ time correlation measurement with photon energy discrimination. Where not explicitly referenced, the used electronics modules were produced by EG&G ORTEC (Oak Ridge, TN, USA). The data were registered using the acquisition system developed at GSI [Ess00].*

statistics information on the electronics dead-time during beam extraction. The count rate capability of the data acquisition system was about $500 - 600$ events per second. In the measurements at $90°$ couch angle the average fraction of events registered in the list mode data file with respect to the amount of triggered events during beam extraction ($C0_s$) was approximately 15% whereas the ratio $C2/C0_s$ was found to be about 80%. Hence, most of the dead-time arises from the ADC and list mode data storage. Time calibrations performed at the beginning and at the end of the experiments revealed a very high stability with deviations below 0.1 ns. On the contrary, a $\simeq 10\%$ drift at $500 - 600$ keV was observed in energy calibration spectra acquired with ^{22}Na and ^{207}Bi sources prior to and after the experimental run in addition to the phantom activation measurements. However, this energy uncertainty does not affect the analysed time distributions, as discussed in the next section.

4.4.2 Results and discussion

The time distribution (figure 4–16) of the detected γ-rays with energy values between $250-850$ keV, i.e. within the acceptance window of the positron camera, confirmed a clear correlation with the RF signal and thus with the measured microstructure of the primary carbon ion beam. Furthermore, no modification in shape was observed when shifting the energy window according to the measured energy drift of the electronics. The depicted time correlation spectra were reversed in time by exchanging the start and stop role of detector and RF signal with respect to the electronics scheme of figure 4–15. In this more straightforward representation
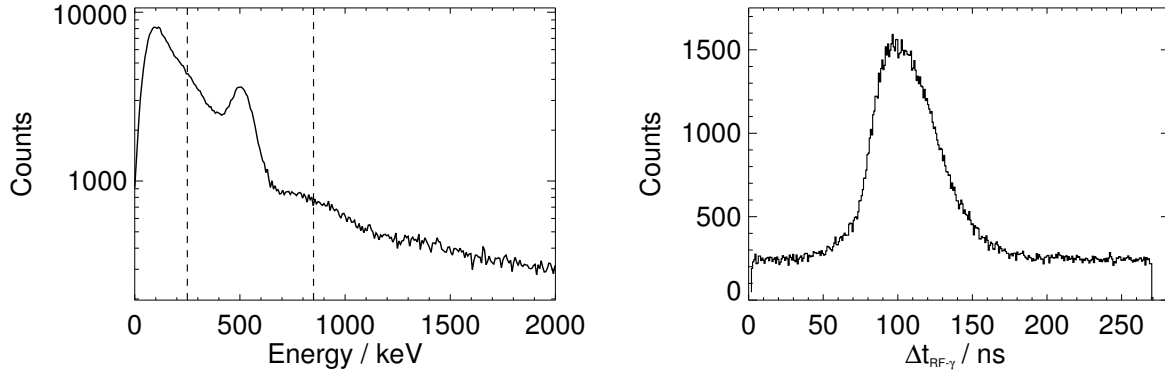
Figure 4–16: *Left: Energy spectrum detected by the GSO crystal during 500 spills of a ^{12}C irradiation at an energy of $280.48\,AMeV$ (RF period of $282.4\,ns$) and an intensity of $8.5 \cdot 10^6\ ions\,spill^{-1}$. Right: Corresponding RF-γ time spectrum restricted to photons with energy deposition in the $250 - 850\,keV$ interval marked by the dashed lines in the left panel.*

the steep leading edge of the asymmetric peak is attributed to prompt γ-rays following nuclear reactions, whereas the slope of the falling edge is diminished by a delayed component originating from the decay of isomeric excited nuclear states and radioisotopes with half-lives in the nanosecond region. The constant bias consistent with the model predictions is primarily due to the decay of longer-lived isotopes mostly ascribed to the phantom β^+-activation. According to this physical interpretation the measured time distributions were described by the function:

$$F(t) = b + a \int_{\bar{t}+\delta}^{t} B(t' - \delta)\, e^{-\frac{(t-t')}{\tau_{\text{eff}}}}\, dt', \qquad \bar{t} \text{ starting time for which } B(\bar{t}) \neq 0, \qquad (17)$$

defined as the convolution of the measured bunched beam flux $B(t)$ presented in section 4.3 (cf. figure 4–13) with an exponential decay accounting for all γ-ray emission processes with half-lives in the sub-microsecond time scale in addition to the bias b. The constant term a is a normalisation factor whereas δ compensates the different delay with respect to the RF signal in the measurement of the carbon ion microstructure and this experiment. A rather good agreement of the model with the measured time spectra was obtained, as shown in figure 4–17. An "effective" decay time τ_{eff} ranging from 19 to 37 ns in the explored energy interval
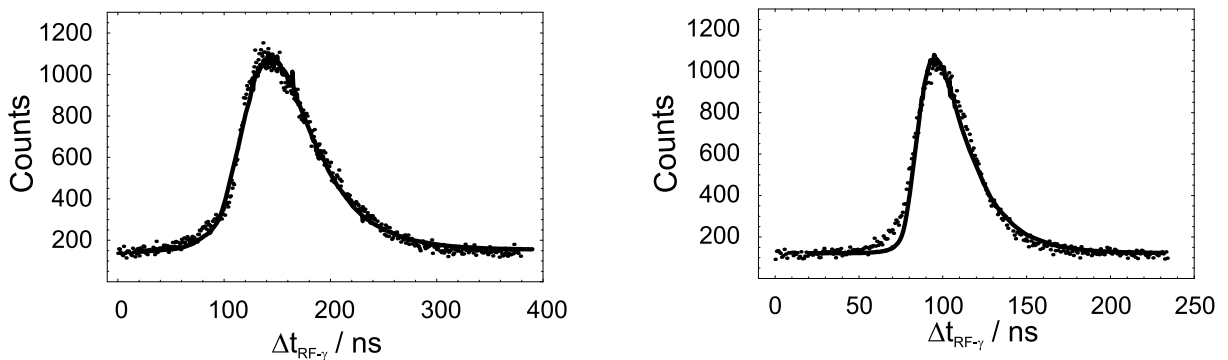
Figure 4–17: *Measured time spectra (dots) in comparison to a non-linear least squares fit (solid line) based on the model of equation (17) for ^{12}C irradiation at an energy of $88.83\,AMeV$ and intensity of $1.3 \cdot 10^8$ ions spill^{-1} (left, total of 420 spills) and at $426.11\,AMeV$ and $3.5 \cdot 10^6$ ions spill^{-1} (right, 350 spills).*
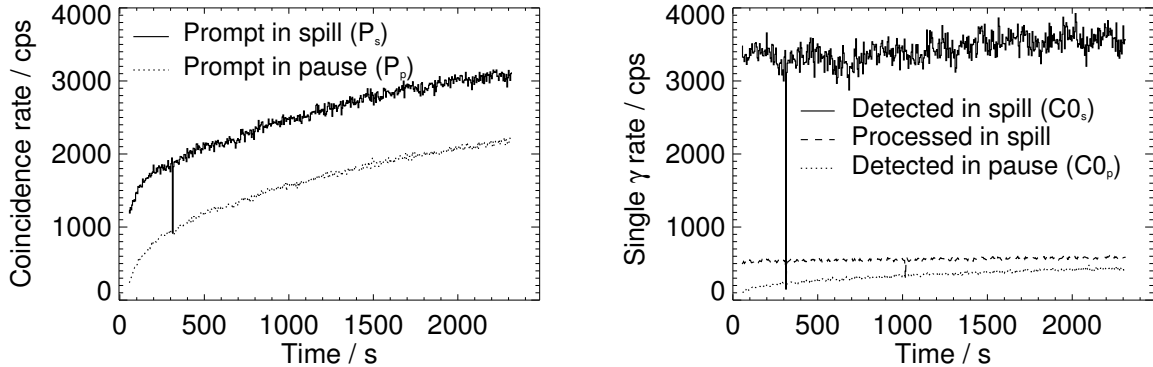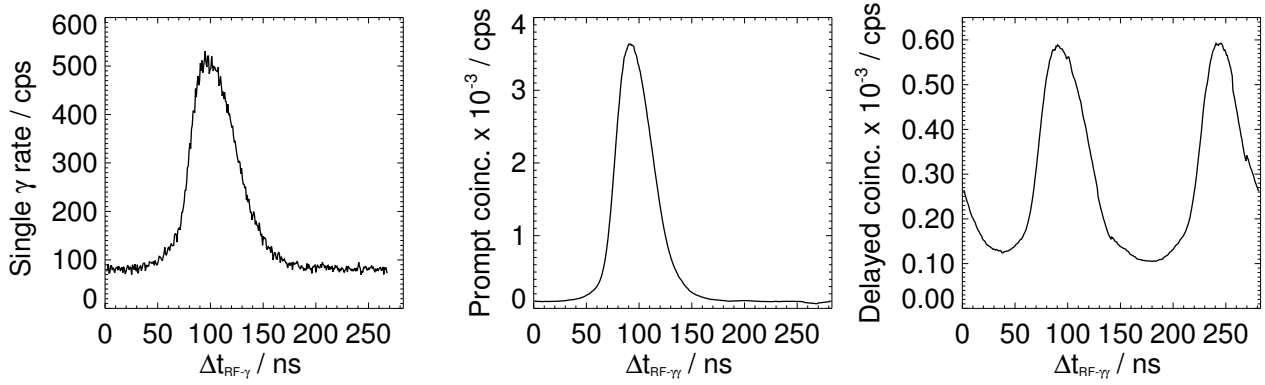
Figure 4–18: *Left: Prompt coincidence rate detected by the PET scanner during particle extraction (P_s) and pauses (P_p) for the same 280.48 AMeV irradiation leading to the GSO energy and time distributions of figure 4–16. Right: Corresponding total (i.e. without energy discrimination) single count rate of GSO events processed by the whole data acquisition system during ion extraction in comparison to the detection rate (deduced from C0) during the beam spills and pauses. The count rate dip at about 300 s in both of PET and GSO data is due to an intensity drop from the accelerator.*

from 426.11 down to 88.83 AMeV, respectively, was extracted from the fit of data measured in the same set-up and under similar condition of data acquisition load. However, an identical average count rate per second on the detector at different primary carbon ion beam energies corresponds to different conditions of dead-time during the micropulses within single RF periods. This is supported by the known changes of the RF period and of the carbon ion bunch widths (table 4–1) in dependence on the beam energy.

The data analysis has been mostly concentrated on the comparison between (*i*) the calculated prompt and delayed random coincidence rates induced by a γ-ray flux modulated in time according to the GSO data in the $250 - 850$ keV energy window and (*ii*) the corresponding P_r and D_r count rates extracted from the simultaneous PET acquisition. In comparison to the previous experiments analysed in section 4.2.3 a stronger contribution of the activated target placed in the centre of the positron camera field of view was obviously found in the PET measurements. This is reflected by the build-up of the coincidence rate P_s detected during the spills visible in figure 4–18 (left) in contrast to figure 4–8. Hence, the fraction of beam induced coincidence rates P_r and D_r was extrapolated from P_s and D_s by means of a more refined estimation of the contribution due to long-lived positron emitter, assuming a constant isotope production rate during the spill and based on the initial and final activity detected by the positron camera shortly before and after each particle extraction (spill). However, no significant difference ($\leq 5\%$) was observed in comparison to the alternative method addressed in section 4.2.3, based on the simple subtraction of the coincidence rates measured in the pauses (P_p and D_p) from those detected during the precedent spills (P_s and D_s).

The corresponding estimation of the prompt and delayed random coincidence rate induced by the γ-ray background measured by the GSO detector was based on the RF-γ time correlation curves acquired for each spill and equation (15) of section 4.2.2 (figure 4–19). However, the GSO measurements were found to be affected by a minor build-up of the induced target activation as well, as indicated by the increase of $C0_p$ with the time of the irradiation in figure 4–18, right. This is expected to affect the measured time distributions by means of a bias varying with the time of the irradiation. In order to enable a correction, the subset of events processed during each spill and originating from the decay of long-lived positron emitters had to be estimated. In analogy to the original approach used for the PET data, the contribution from long-lived

Figure 4–19: *Measured RF-γ time correlation for the 280.48 AMeV irradiation (left, cf. figure 4–18) and estimated time dependent prompt (middle) and delayed (right) coincidence rates (integrands in bracket of equation 15), not yet corrected for the contribution of long-lived β^+-emitters (cf. text). The shown data were obtained from the time spectrum measured over the whole irradiation to reduce statistical fluctuations for visualisation purposes, whereas single contributions during each spill were considered for data analysis. (For clarity this figure was included after the defense of the thesis at TU Dresden.)*

emitters was deduced from the count rate measured in the beam pauses. This was achieved on the basis of the following available information. The measured detector count rate during the beam pauses (extracted from $C0_p$) was corrected for the data acquisition dead-time, which was deduced from the ratio between the measured amount of processed and detected ($C0_s$) events during particle extraction (figure 4–18). This approximation, assuming a constant dead-time during beam extraction and extraction pauses, is justified by the previous dead-time considerations, showing a dominant contribution from the list mode acquisition rather than the event count rate on the detector. However, this approach does not include any energy discrimination. Nevertheless, events measured during the beam pauses can be mostly ascribed to positron emitter decays. Therefore, the fraction of single γ-rays resulting from long-lived β^+-decays and falling into the $250 - 850 \, \text{keV}$ energy window was deduced from measurements with positron emitting sources. After this correction, the resulting estimate of the amount of registered events per each spill due to the decay of long-lived positron emitters was realistically assumed to be uniformly distributed in time within single RF periods. Therefore, for each irradiated spill a bias was subtracted from the measured time correlation spectra. Contributions due to short-lived positron emitters were neglected as in the case of the PET data (cf. section 4.2.3). The corrected time distributions, periodically extended on the basis of the known RF period, were finally used as probability density function $f(t)$ in order to determine the beam induced prompt and delayed coincidence rates according to equation (15).

The resulting estimates of the ratio between the delayed (D_r) and prompt (P_r) beam induced coincidence rates extracted from the PET and the GSO data simultaneously acquired are compared in figure 4–20 for different initial beam energies. The quantities deduced from the GSO single count rates were normalised to the average values of the estimated PET coincidence rates in order to compensate for the different detection efficiency and the different signal processing. Furthermore, a median filter over 10 subsequent spills was applied in order to reduce statistical fluctuations. Both of the estimates based on the PET and the GSO acquisitions exhibit a common trend for the increase of the beam induced delayed to prompt coincidence rate ratio with the time of the irradiation. This is mostly originated by the increase of the delayed coincidence rate D_r up to a rather constant plateau during the irradiation. Such an observation may be attributed to
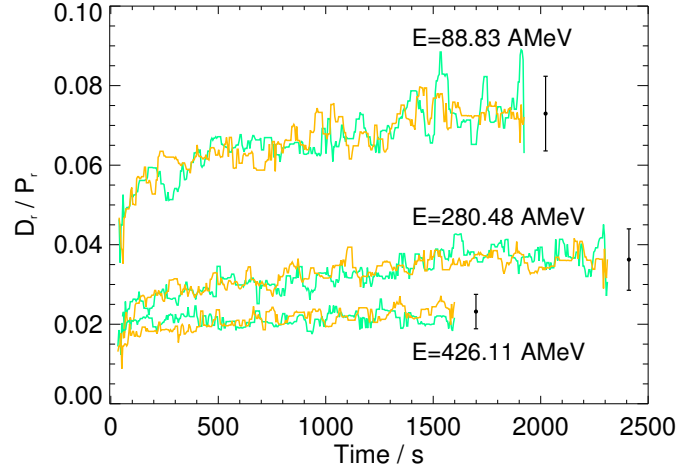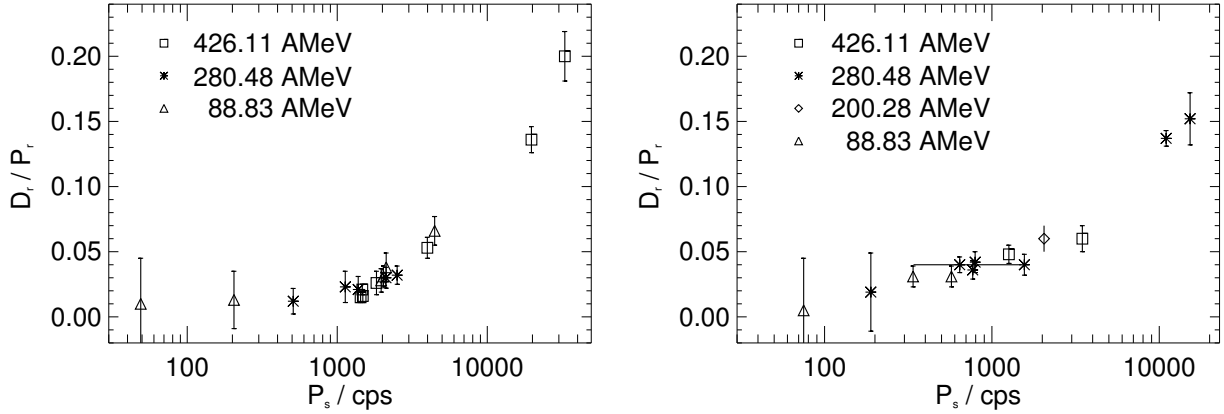
Figure 4–20: *Ratios of the beam induced delayed and prompt coincidence rates extracted from the simultaneous PET and GSO acquisition for carbon ion irradiation at 88.83, 280.48 and 426.11 AMeV. The quantities extracted from the GSO data (orange curves) were normalised to the average values of those deduced from the PET measurements (green). For each pair of curves the mean error is given by an error bar. The acquisitions correspond to the GSO time spectra of figures 4–16, 4–17.*

the enhancement of events contributing to the bias b of the γ-ray background model – equation (17) – via increasingly formed long living isotopes from fragmentation reactions between the ^{12}C projectiles and the PMMA target until saturation over the time of irradiation. The resulting increase of the delayed to prompt coincidence rate ratio for an increasing bias can be deduced from figure 4–6. However, an additional effect may derive from an inefficient subtraction of the β^+-activity build-up due to the long-lived β^+-emitters. Nevertheless, the good correspondence between the quantities extracted from the two independent PET and GSO data sets indeed supports the explanation of the random correction failure of the positron camera due to the measured γ-ray background correlated in time with the beam microstructure.

Figure 4–20 furthermore indicates a decrease of the average ratio $\langle D_r/P_r \rangle$ for increasing carbon ion beam energies. Such a trend is in agreement with the decrease of τ_{eff} – cf. equation (17), suggesting an increase of the prompt γ-ray component at higher carbon ion beam energies. However, the parameters of the time correlation spectra measured by the GSO detector (figures 4–16 and 4–17) in combination with the widths and periods of the particle bunches (table 4–1) cannot explain such a strong dependence of the $\langle D_r/P_r \rangle$ ratio on the initial carbon ion beam energy as observed in the PET data. The most plausible explanation for this discrepancy is a dependence of the D_r/P_r ratio on the coincidence rate measured by the positron camera due to different conditions of dead-time within the micropulses of the irradiation. The considered acquisitions at 88.83, 280.48 and 426.11 AMeV were performed at beam intensities of $1.3 \cdot 10^8$, $8.5 \cdot 10^6$ and $3.5 \cdot 10^6$ ions spill^{-1}, respectively. These values corresponded to different average prompt coincidence rates P_s of 4.5, 2.5 and 1.5 kcps, respectively, detected by the positron camera during particle extraction. In order to examine this issue more in detail, the dependence of the D_r/P_r ratio on the photon flux reaching the positron camera has been further investigated in the series of experiments reported in the following.

The beam induced photon flux on the detector heads varies in dependence on the energy and intensity of the primary carbon ion beam in combination with the characteristics of the irradiated target as well as its position relative to the positron camera. Hence, several irradiation of PMMA targets were repeated in the same configuration at given initial energies but with significantly different primary carbon ion beam

Figure 4–21: *Average beam induced delayed to prompt coincidence ratios extracted from PET data measured for PMMA phantoms centered in the FOV of the positron camera (left) or at the edge of the FOV (x = 21 cm, right). The carbon ion beam intensity was varied over the whole range $2 \cdot 10^6 - 2 \cdot 10^8$ ions spill^{-1} available for therapy, corresponding to the depicted total prompt coincidence rate P_s of the positron camera during beam extraction. The intensity interval explored in the previous measurements (section 4.2.3) suggesting the average ratio of $D_r/P_r \simeq 0.04$ is marked by the solid line in the right panel.*

intensities, spanning the whole interval $2 \cdot 10^6 - 2 \cdot 10^8$ ions spill^{-1} available for therapy. Acquisitions with the target placed in the centre of the positron camera FOV – i.e. resembling realistic conditions for therapy monitoring – were compared to additional measurements in the set-up of figure 4–2 at a phantom distance x of 21 cm. This choice provided a comparison of results for two configurations with either a significant or a marginal influence from the contribution of positron emitters to the total coincidence rate in spill P_s, respectively. The data shown in figure 4–21 indeed confirm a dependence of the D_r/P_r ratio on the positron camera count rate (reflecting the photon flux variation in dependence on the beam energy and intensity). Furthermore, the only difference for the two phantom positions is found to be a stretching factor of the horizontal axis in the figure. This arises from the different contribution to P_s coming from the decay of positron emitters (negligible for the phantom position outside the FOV) in addition to the beam induced component P_r itself. Whereas values at low coincidence rates are affected by the poor counting statistics, reflected by the large error bars, the observed increase of the D_r/P_r ratio at higher coincidence rates above about $1 - 2$ kcps is ascribed to the increasing dead-time of the PET data acquisition during the micropulses. This mostly affects the detection of the considerably higher prompt coincidence rate. As a rough estimation, at the lowest energy of 88.83 AMeV the average prompt count rate in spill P_s was found to be 50 cps at an intensity of $1 \cdot 10^6$ ions spill^{-1} in the same configuration of the GSO experiment. In this low count rate measurement an average $\langle D_r/P_r \rangle$ ratio of about 0.01 was found. At the increased intensity of $1.3 \cdot 10^8$ ions spill^{-1} the expected average coincidence rate in spill P_s would rise up to a maximum of 845 kcps. Furthermore, the average count rate values are estimated to correspond to instantaneous coincidence rates up to a factor 10 times higher during the micropulses, according the measured parameters of the microstructure and of the beam induced γ-ray background. The resulting maximum value of 8.45 Mcps is well above the coincidence rate processing capability of the positron camera installed at GSI, limited to about 400 kcps. Hence, this rough calculation explains a lower prompt coincidence rate detected by the positron camera during particle extraction at higher beam intensities. Such a reduction can be therefore responsible for the underestimate of P_r leading to the higher D_r/P_r ratio reported in figure 4–20 for the considered 88.83 AMeV irradiation at $1.3 \cdot 10^8$ ions spill^{-1} intensity. It should be also noticed that this count rate dependence was not observed
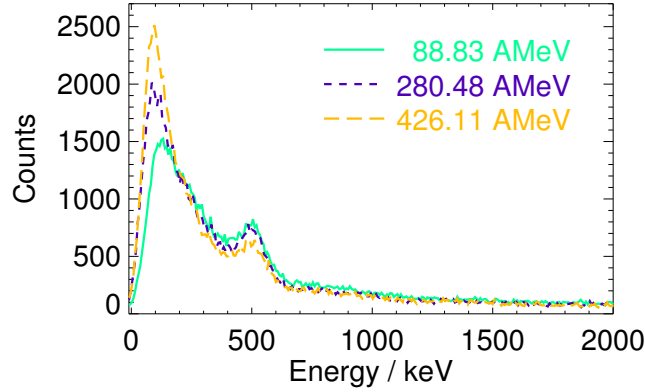
Figure 4–22: *Energy spectra acquired by the GSO detector during the first 100 spills of carbon ion irradiation at 88.83, 280.48 and 426.11 AMeV and intensities corresponding to a similar acquisition dead-time in the same experimental set-up. The data were normalised to the area of the lowest energy spectrum.*

in the initial study reported in section 4.2.3. This preliminary investigation was in fact intentionally limited to the narrow intensity range corresponding to the region marked in figure 4–21 (right) in order to avoid to exceed the count rate capabilities of the imaging system. Finally, the rough independence of the results of figure 4–21 on the primary carbon ion energy for both of the experimental configurations at a given photon flux is in agreement with the measured parameters of the microstructure and of the beam induced γ-ray background, resulting in variations of the D_r/P_r ratio less than 30 % at the considered different energies. However, it should be stressed once more the high sensitivity of the beam induced delayed to prompt coincidence ratio on the parameters of the single γ-ray background, especially for small bunch widths and bias values as illustrated in figure 4–6.

Up to this point the analysis has been focussed on the random coincidence problem for the positron camera installed at GSI. In the following, additional properties of the beam induced background radiation are reported. This includes the comparison of the γ-ray flux and energy spectra measured by the GSO detector in dependence on the primary carbon ion beam energy and on the angle with respect to the beam direction as well as a deeper spectroscopic insight by means of a Ge detector. The aim is to provide a more complete information which might be of interest for the definition of the technical specifications of an in-beam PET tomograph in presence of an ion beam delivery pulsed on the sub-microsecond time scale. Hence, only technically relevant aspects will be outlined, whereas a detailed understanding of the complex mixture of physical processes behind the findings of the data analysis is beyond the purpose of this work.

Energy spectra measured by the GSO scintillator during carbon ion irradiation at different initial energies and intensities corresponding to a similar acquisition dead-time are compared in figure 4–22. The variation of the height of the 511 keV annihilation peak with respect to the low energy component of the continuous background in dependence on the carbon ion beam energy is evident. This resulted into a reduced fraction of photons falling into the $250 - 850$ keV energy window at increasing beam energies. Despite the rather constant ratio of the probability per unit path length for nuclear reactions leading to prompt photon emission or positron emitter production at different initial beam energies, the data indicate a relative increase of the prompt photon flux for increasing carbon ion energies. This may imply a further photon flux increase for higher beam energies at the same primary ion intensity, in addition to the enhancement due to the larger amount of nuclear reactions along the higher penetration depth. Therefore, different conditions of pile-up and dead-time on the detectors in dependence on the beam energy and intensity should be taken into account
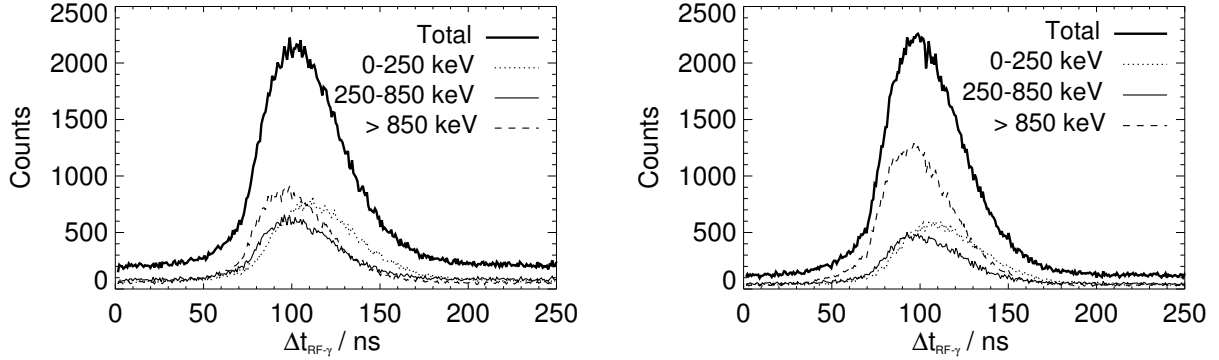
Figure 4–23: *RF-γ time correlation spectra measured during 200 spills of carbon ion irradiation at 280.48 AMeV energy. The left acquisition was performed at a couch angle of 90° and an intensity of $8.5 \cdot 10^6 \, ions \, spill^{-1}$. The right one refers to a 34° angle and $3.5 \cdot 10^6 \, ions \, spill^{-1}$. The time distributions of events detected in different energy intervals are shown.*

for realistic applications of in-beam PET to therapy monitoring. In particular, the count rate capabilities of a system intended to be operated also during particle extraction should be designed on the basis of the huge beam induced γ-ray background component rather than the relatively low amount of positron radioactivity induced by stable ion beams in typical treatment situations. This suggests special care in the selection of the energy thresholds for coincidence detection in PET imaging. From figure 4–22 especially the lower value of 250 keV seems to be inappropriate and should be increased up to about 350 keV. Similarly, the high energy threshold of 850 keV might be decreased to about 650 keV.

GSO measurements performed at different couch angles (cf. set-up of figure 4–14) indicated also an anisotropic γ-ray fluence distribution peaked in the forward emission cone. As an example the ratio of registered to detected ($C0_s$) events dropped to 13 % at 34° couch angle against the 16 % value at 90°, despite the reduction of the primary ion beam intensity by a factor 2.4 for the same irradiation condition at 280.48 AMeV. The explored angular dependence revealed also a variation of the energy spectrum, reflected by the different contributions to the total time distributions given by photons within, below and above the energy window for PET monitoring (figure 4–23). Almost no difference can be observed in the shape of the shown time spectra, apart from the bias reduction in all the considered energy intervals at the 34° couch position. But a considerable and systematic enhancement of the high energy component above 850 keV was clearly found for detector positions at small angles with respect to the beam axis. Moreover, the observed fluence enhancement significantly involves also energies well above the upper threshold of the PET energy window. This is indicated by the increase of the overflow (i.e. amount of depositions above the upper threshold of about 3.4 MeV in the energy acquisition) up to 55 % of the energy component above 850 keV at 34° couch angle in comparison to the 32 % at 90°. This suggests also the possible presence of a particle component due to nucleons, particles and fragments mostly emitted in the forward beam direction in nuclear interactions [Gun04]. Hence, besides the care in the selection of the upper threshold of the energy window for PET coincidence detection, consequences of different spatial detector arrangements on pile-up, dead-time and also possible detector activation have to be considered.

Further information on the complex mixture of the beam induced radiation superimposed onto the background component from the environment and from the β^+-activation of the PMMA target were provided by the spectroscopic measurements performed with a Germanium detector placed perpendicularly to the beam in the same configuration of the GSO experiment. In figure 4–24 an in-beam energy spectrum acquired dur-
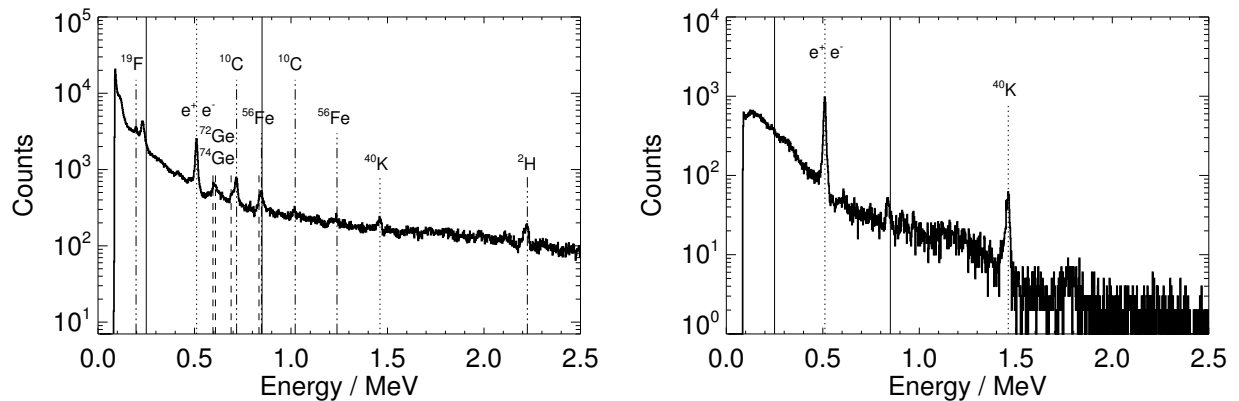
Figure 4–24: *Left: Energy spectrum recorded by the Germanium detector during 250 spills of a carbon ion irradiation at 280.48 AMeV and $4 \cdot 10^6$ ions spill^{-1} intensity corresponding to a count rate of about $4000 \, s^{-1}$ and 15 % dead-time. Besides the continuous spectrum, lines ascribed to beam induced processes (dotted-dashed), detector excitation/activation (dashed) and natural background or positron annihilation (dotted) are marked. The energy window relevant for PET imaging is indicated by the solid lines. Right: Activation measurement of the target during the 5 min immediately following the end of the beam delivery.*

ing 20 minutes of irradiation is compared to a 5 minutes long measurement of the target activation started immediately after finishing the beam delivery. Clearly, in the measurement exclusively performed during particle extraction the ^{40}K line of 1461 keV from the natural background is embedded in a beam induced continuous background. In this in-beam spectrum lines ascribed to the production of stable but excited nuclei (e.g. ^{19}F) or radioactive isotopes (e.g. ^{10}C) have been identified. Further lines have been attributed to deuteron formation or prompt excitation of the beam dump, exclusively consisting of iron [Schar01]. Additional lines falling within the energy window of interest for PET are attributed to emissions from the Germanium detector, mostly due to $(n, n'\gamma)$ reactions. However, these events do not obviously pertain to the GSO experiment. Besides, they can only slightly affect the positron camera measurements, due to the content of Germanium in BGO. Few lines of the in-beam spectrum (e.g. the one at about 230 keV) could not be unambiguously identified, due to the limited quality of the detector, the insufficient knowledge of all background components of the environment as well as the different measuring time between the in-beam and off-beam acquisition. Nevertheless, they involve energy regions of no interest for PET imaging and their characterisation is therefore beyond the aim of this study. Instead, it is important to remark that no significant activation as well as beam induced background radiation was observed after finishing the beam delivery, as indicated by the off-beam spectrum dominated by the 511 keV annihilation peak and the natural background. In addition to the shown variation of the flux and energy spectrum of the γ-rays in dependence on the carbon ion beam energy and direction, this spectroscopic investigation furthermore points out the dependence on the specific target (e.g. each individual patient in the individual treatment position) in addition to the environment (e.g. the beam dump).

4.5 Conclusion

In summary, all the presented experimental validations support the consistency of the proposed model which attributes the noise of in-beam PET acquisition at the GSI facility to not properly corrected random coincidences originating from a γ-ray background correlated in time with the carbon ion beam microstructure.

The measured time distributions of the γ-rays following the beam appearance indicate that during particle extraction a rather large fraction of each RF period (from about one third up to an eventual entire period in case of low beam intensities) contains usable events for PET imaging. These events are currently discarded according to the present data acquisition scheme, capable to discern only the macroscopic structure of the irradiation (beam on/off). Standard random correction techniques based on the measurement of delayed coincidences or single count rates have been demonstrated to be inapplicable due to the time variation of the γ-ray background during the microbunches of the particle extraction. An alternative exploiting the periodicity of the γ-ray flux by adjusting the time shift of the delayed window to the RF period of the given beam energy for each spill is also not practicable. In addition to the technological challenge of such a solution, the γ-ray flux varies from one microbunch to the next due to statistical fluctuations, intensity instabilities from the accelerator on the sub-microsecond time scale as well as beam modifications in space and time due to the raster scanning technique. Therefore, the random coincidences due to the beam induced γ-ray background have to be suppressed. Hence, on the basis of the presented basic investigation an alternative solution for in-beam PET acquisition has been proposed [Eng04b] and is currently under implementation and experimental validation [Cre04]. The aim is to recover the useful signal from long-lived positron emitters decayed during beam extraction, in order to increase the poor counting statistics of in-beam PET imaging during therapeutic sessions. In fact, the same beam microstructure is foreseen also for the Heidelberg facility, despite the planned substitution of the slow resonant extraction with a knock-out technique [Eic01]. However, it has to be finally mentioned that the recovered events will also contain a contribution from the decay of short-lived positron emitters. As qualitatively addressed in section 4.2.3, the activity contribution from these short-lived positron emitters with half-lives $T_{1/2} \ll 1\,\mathrm{s}$ may be not negligible. Since the in-beam PET monitoring of carbon ion therapy at GSI is presently limited to the processing of data acquired during the beam pauses, mostly originated from long-lived positron emitters, no deeper insight into this issue has been performed yet. Therefore, a realistic quantification of the production rate of millisecond short-lived β^+-emitters as well as the consequence of their longer positron range due to the typically higher endpoint energies on the quality of the PET images for therapy monitoring is a still open question.

5 In-beam PET for proton therapy monitoring

5.1 Motivation

The clinical experience at GSI Darmstadt has demonstrated the important contribution of in-beam PET to quality assurance of high precision carbon ion therapy, due to the possibility to *(i)* monitor the maximum ion range, *(ii)* verify the field position and in some cases *(iii)* detect and quantify unpredictable deviations of the applied dose with respect to the treatment plan, as shown in chapter 3. The physical selectivity of protons is comparable to carbon ions for realisation of highly conformal radiotherapy. Hence, a similar clinical benefit is expected from the possibility to control the precision of dose delivery simultaneously to proton irradiation by means of in-beam PET techniques, at least in delicate clinical cases. However, the straightforward extension of positron emission imaging to monitor proton therapy is nontrivial. Due to the absence of projectile fragmentation reactions no pronounced maximum of β^+-activity is formed in close vicinity to the Bragg-peak as in the carbon ion case (cf. section 2.1.4). Additionally, the β^+-activation of the target nuclei vanishes along the last few millimetres of proton penetration due to the energy threshold for nuclear reactions. Hence, the spatial correlation between the induced β^+-activity distribution and the proton range as well as the dose delivery is poor, as already pointed out by previous investigations [Oel96]. Furthermore, the partial cross sections for proton-nucleus reactions leading to the production of the main positron emitters of interest for PET monitoring are up to three times lower than the corresponding ones for carbon-nucleus interactions, according to the available experimental data as well as the formulae of [Sih93] (cf. sections 2.1.3 and 2.1.4).

Up to now, despite the widespread installation of proton therapy facilities as well as the growing interest for more strict quality assurance in high precision charged hadron therapy, no definitive conclusion on the feasibility and value of PET for in-situ control of proton therapy has been drawn. Therefore, the issue has been addressed again in this work. With respect to the previous investigations mentioned in section 1.2, more answers on the potentialities and limitations of in-beam PET for quality assurance of proton therapy have been derived from the comparison with the already clinically implemented carbon ion case as well as the experimental availability of the unique in-beam PET scanner installed at GSI. The initial feasibility study reported in section 5.2 has been entirely based on Monte Carlo simulations. Supported by the encouraging results, very promising in-beam phantom experiments have been carried out at GSI for the first time, as presented and discussed in section 5.3. The conclusions are drawn in section 5.4.

5.2 Initial predictions

5.2.1 Material and methods

The two main items deciding on the applicability of PET techniques to the monitoring of proton therapy are the amount and the spatial distribution of the proton induced β^+-activity. The former determines the feasibility of signal detection during or shortly after the irradiation of the patient for on-line or off-line monitoring, respectively. The latter affects the possibility to extract information on the particle range and to control the precision of the dose delivery. Therefore, the initial feasibility study has investigated the amount and the spatial distribution of the main positron emitters produced in organic plastic by mono-energetic pencil-like (non divergent, lateral profile of $10\,\mathrm{mm}$ FWHM) proton beams at initial kinetic energy within the $60-220\,\mathrm{MeV}$ interval of interest for therapy. Polymethyl methacrylate (PMMA, composition: $C_5H_8O_2$, density: $1.18\,\mathrm{g\,cm^{-3}}$) has been selected as target material because of the favourable stoichiometric composition including the most abundant elements of living tissue, the density similar to that of water as well as

the practical suitability for further experimental verification. Proton transport has been calculated on the basis of the FLUKA Monte Carlo code [Fas01a, Fas01b] which is a general purpose program already successfully applied to simulation of therapeutic proton beams for dosimetric and radiobiological problems [Bia99]. Besides all main electromagnetic physical processes the code takes into account also hadronic interactions. Nuclear reactions are treated by means of a model [Fer97] starting from explicit intra-nuclear cascade (INC). After the full INC treatment stops (when all nucleons have energies below 50 MeV and all particles except nucleons have been emitted or absorbed) a statistical preequilibrium emission accounts for nuclear thermalisation. At the end of the preequilibrium stage the thermalised, but still excited residual nucleus approaches the final configuration via particle evaporation, γ-ray de-excitation or fragmentation according to the Fermi Break-up model for light isotopes ($A \leq 17$). Hence, among the wide spectra of products the model is capable of predicting the formation of β^+-emitters, too.

For a quantitative estimate of the practicability of β^+-activity detection during and shortly after proton irradiation, the calculated production of the most abundant positron emitters and the resulting number of decays within a typical average measurement time of five minutes have been compared to the corresponding amounts induced by the same number of primary ^{12}C ions at energies leading to a similar penetration depth. The latter values have been obtained from the predictions of the dedicated POSGEN Monte Carlo code [Has96] developed for calculation of the PET database currently in clinical use for the monitoring of carbon ion therapy at GSI (cf. section 2.3.3). The qualitative analysis of the β^+-activity spatial distribution has been focussed on the study of positron emitter depth profiles, which determine the feasibility of range monitoring and control of the correct dose delivery in the most critical distal (i.e. away from the origin of the radiation in contrast to proximal) part of the irradiation field. Hence, additional dose depth profiles have been obtained by calculating the energy deposition in cylindrical detectors of 5 mm radius and 1 mm length along the central beam axis for 10^6 primary protons and carbon ions (lateral FWHM of 10 mm) by means of FLUKA and POSGEN, respectively.

5.2.2 Results and discussion

The predicted amount of the most abundant nuclei (^{15}O, ^{11}C and ^{10}C) produced by three mono-energetic pencil-like proton beams of 70, 140 and 200 MeV ($\pm 0.1\%$ momentum spread) is presented in table 5–1. The comparison with the corresponding values for carbon ion irradiation shows a reduction of about one order of magnitude of the proton induced activation at the same range and number of primary ions. However, the applicability of positron emission imaging to therapy monitoring demands a comparison for a number of projectiles leading to the same dose deposition at a given penetration depth. Hence, an increase of the proton fluence up to a factor of about 20 has to be taken into account in order to compensate the lower stopping power of protons in comparison to carbon ions at energies corresponding to the same range in a given material (cf. figure 5–1, figure 5–2 and equation 3 in chapter 2). From these considerations the total β^+-activity signal produced within the treated volume by a therapeutic proton irradiation is expected to be about two times larger than that measured by the in-beam limited angle positron camera for carbon ion dose application at GSI. The factor of 2 is expected to increase further in realistic clinical cases on the basis of considerations on the relative biological effectiveness of carbon ions and protons [Wam99, Kra99]. Therefore, this quantitative analysis supports the feasibility of PET signal detection during or shortly after a proton therapeutic irradiation. An on-line solution is strongly suggested on the basis of the values presented in table 5–1. The contribution from ^{15}O is expected to dominate the proton or ^{12}C ion induced β^+-activity signal shortly after production in realistic patient treatments, according to the tissue composition, the reaction cross sections and the isotope half-life. Hence, an in-beam detector similar to the device used at

Table 5–1: *Positron emitter production predicted by the FLUKA and POSGEN Monte Carlo codes for proton and ^{12}C ion irradiation, respectively, of thick PMMA targets at typical therapeutic energies E and ranges R. The amount of ^{15}O ($T_{1/2} = 121.8\,s$), ^{11}C ($T_{1/2} = 1222.8\,s$) and ^{10}C ($T_{1/2} = 19.3\,s$) produced per 10^6 projectiles and the related number of β^+-decays within 5 min after production are given.*

Isotope	Protons			^{12}C ions		
	E / MeV	Amount	Decays	E / AMeV	Amount	Decays
	R / cm	per $10^6\,p$	in 5 min	R / cm	per $10^{6\ 12}$C	in 5 min
^{15}O	200.0	$2.071 \cdot 10^4$	$1.69 \cdot 10^4$	400.41	$1.679 \cdot 10^5$	$1.37 \cdot 10^5$
^{11}C	$\simeq 22.6$	$4.572 \cdot 10^4$	$7.15 \cdot 10^3$	$\simeq 23.2$	$4.272 \cdot 10^5$	$6.68 \cdot 10^4$
^{10}C		$2.171 \cdot 10^3$	$2.17 \cdot 10^3$		$2.990 \cdot 10^4$	$2.99 \cdot 10^4$
$\sum$			$2.62 \cdot 10^4$			$2.34 \cdot 10^5$
^{15}O	140.0	$1.230 \cdot 10^4$	$1.01 \cdot 10^4$	270.55	$1.004 \cdot 10^5$	$8.22 \cdot 10^4$
^{11}C	$\simeq 12.1$	$2.665 \cdot 10^4$	$4.17 \cdot 10^3$	$\simeq 12.3$	$2.661 \cdot 10^5$	$4.16 \cdot 10^4$
^{10}C		$9.46 \cdot 10^2$	$9.46 \cdot 10^2$		$1.964 \cdot 10^4$	$1.96 \cdot 10^4$
$\sum$			$1.52 \cdot 10^4$			$1.43 \cdot 10^5$
^{15}O	70.0	$3.919 \cdot 10^3$	$3.21 \cdot 10^3$	126.11	$2.876 \cdot 10^4$	$2.35 \cdot 10^4$
^{11}C	$\simeq 3.5$	$7.595 \cdot 10^3$	$1.19 \cdot 10^3$	$\simeq 3.3$	$8.821 \cdot 10^4$	$1.38 \cdot 10^4$
^{10}C		$7.0 \cdot 10^1$	$7.0 \cdot 10^1$		$5.960 \cdot 10^3$	$5.96 \cdot 10^3$
$\sum$			$4.47 \cdot 10^3$			$4.33 \cdot 10^4$

GSI should allow the most efficient utilization of the PET signal.

The simulated spatial distribution of the considered positron emitting nuclei, projected onto the penetration depth and superimposed onto the dose depth profile, is shown in figure 5–2 for the three proton beams and one carbon ion energy. The proton induced activation is rather constant along the penetration depth and drops to zero shortly before the Bragg-peak and the primary proton range (listed in table 5–1). The position
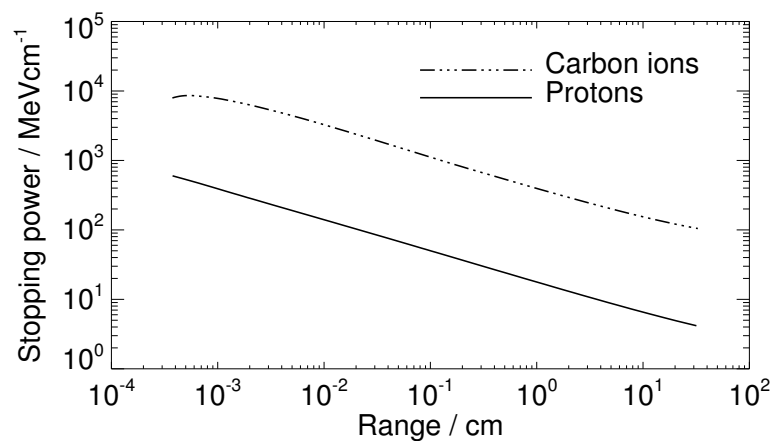
Figure 5–1: *Stopping power of protons and carbon ions as a function of the residual range in water according to the ICRU report 49 [ICR93] and the predictions of the ATIMA code [Schw91], respectively. The ratio of about 20 decreases for low residual range ($< 10^{-3}$ cm) due to effective charge effects (eq. 2 in chapter 2).*
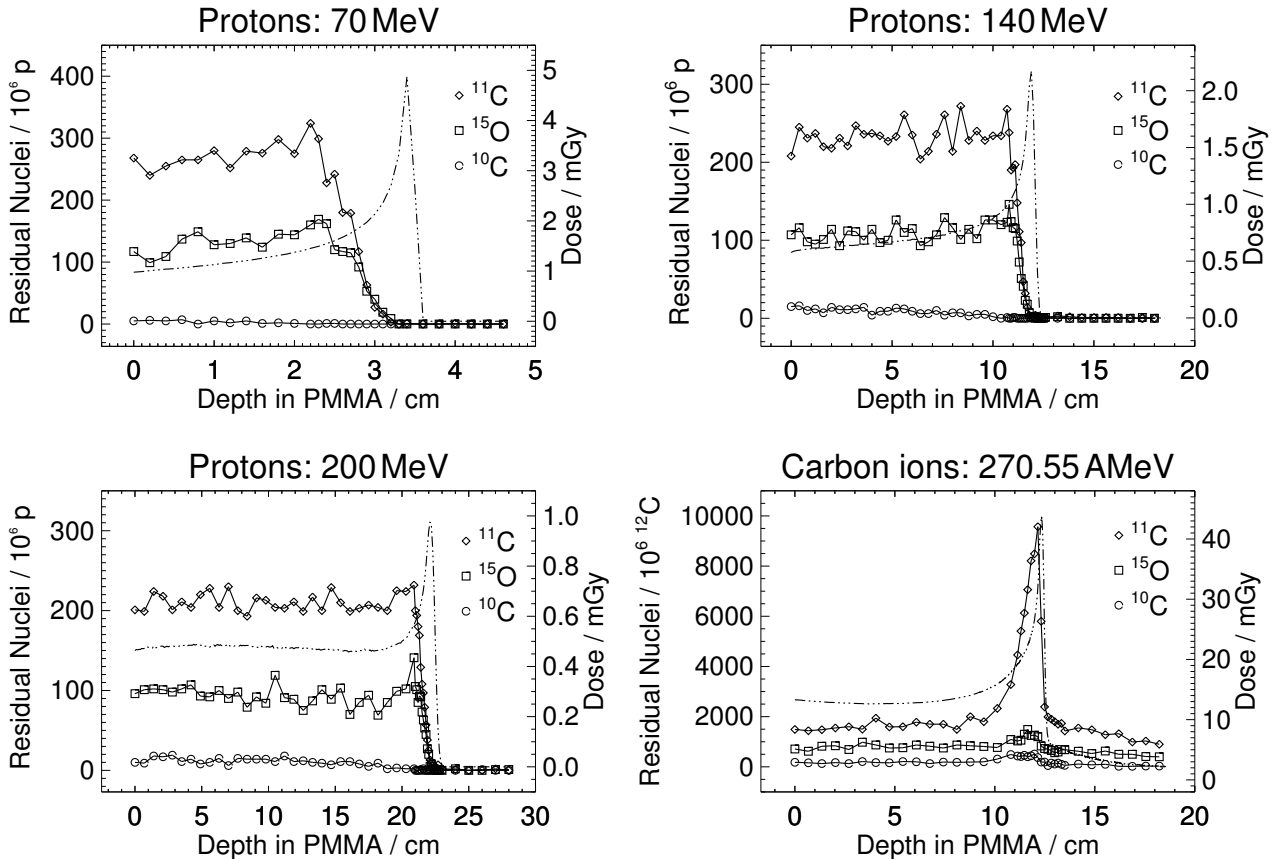
Figure 5–2: *Depth distribution of ^{11}C, ^{15}O and ^{10}C produced in PMMA by proton irradiation at 70, 140 and 200 MeV initial energy and a 270.55 AMeV carbon ion beam, according to the FLUKA and POSGEN predictions, respectively. The calculated dose depth profile is additionally shown by the dashed-dotted curve. The factor of about 20 between the dose delivered by the same number (10^6) of primary carbon ions and protons at initial energies corresponding to the same penetration depth can be noticed from the right panels.*

of the distal fall-off is mainly influenced by the 16.6 MeV and 20.3 MeV energy thresholds [Vyn93] for the main (p, pn) reaction channels leading to the production of ^{15}O and ^{11}C, respectively. This means that the systematic distance of about 6 mm observed between the 50 % level of the distal edge of the total positron emitter distribution and the dose maximum could change in other materials than PMMA, depending on the proton residual range at energies below the reaction thresholds and on the C/O ratio of the medium composition. A similar spatial correlation between the distal fall-off of the induced positron emitter distribution and the maximum proton range is also expected in more realistic extended treatment fields. This is supported by a previous off-line PET phantom experiment showing nearly no difference in the shape of the very distal slope of the β^+-activity distribution induced by a mono-energetic and a spread-out Bragg-peak irradiation [Oel96]. Therefore, despite the absence of β^+-emitting projectile fragments in close proximity to the dose maximum as in the case of heavy ions like carbon (figure 5–2), the extraction of information on the maximum particle range and Bragg-peak position from the distal fall-off of the activity distribution as well as the localisation of the beam path and of the delivered dose from the track of activated target nuclei seems to be possible in the proton case, too. Because of the poor spatial correlation between dose and positron radioactivity distributions, therapy monitoring has to be performed by comparing measured PET images with realistic predictions based on the individual treatment plan of the patient and the time

course of the specific irradiation, as already done for the quality assurance control of carbon ion therapy at GSI [Eng99b]. In combination with the predicted increase of counting statistics, a positive clinical impact of PET is expected from the possibility to check the precise stopping of the protons in the patient, to verify the correct position of the irradiation field and to control the stability of the treatment over all sessions of fractionated therapy. However, this conjectured successful applicability of PET to the monitoring of proton therapy still demands careful experimental verification, as described in the next section.

As a concluding remark it can be noticed that the reliability of the quantitative estimate of the proton induced activation has been supported by the comparison with a previous off-line phantom experiment [Oel96] discussed in [Par00]. Considerations on the accuracy of the simulated spatial distribution of positron emitters will be addressed in the next chapter, where refinements of the calculation model for comparison with the measured β^+-activity profiles are presented.

5.3 Experimental investigations

Following the promising results of the preliminary simulation study, the feasibility of proton therapy monitoring by means of PET has been further investigated in a series of in-beam phantom experiments carried out at the heavy ion synchrotron of GSI Darmstadt. In December 2000 three mono-energetic pencil-like proton beams with initial energy of 110, 140 and 175 MeV were for the first time delivered to the medical cave dedicated to carbon ion therapy. They were completely stopped in PMMA targets placed in the centre of the field of view (FOV) of the in-beam positron camera. Despite the suboptimal quality of the beam, exhibiting fluctuations in lateral position of about 5 mm but stable intensity, the β^+-activation of the targets could be imaged with high statistics. These measurements addressed the same issues like the simulation study: the amount and the spatial distribution of positron radioactivity induced by mono-energetic proton irradiation of homogeneous targets. The resulting quantitative comparison with the carbon ion case is presented in section 5.3.3.1, whereas depth and lateral profiles are shown in section 5.3.3.2 and 5.3.3.3, respectively.

A further set of experiments was carried out in March 2003, when beams of better quality in terms of focussing stability and better characterisation of the beam parameters became available. This made possible also the use of the raster scan system for multi-dimensional mono-energetic and spread-out Bragg-peak (SOBP) irradiation. However, the lowest energy deliverable at the minimum meaningful intensity values of about $10^8\,p\,s^{-1}$ was limited to about 150 MeV. This second experimental run allowed to complete the investigation on the spatial distributions of β^+-activity induced by irradiation fields extended in the longitudinal (SOBP) and transversal (scanned fields) dimension, as discussed in section 5.3.3.2. Furthermore, it addressed the more delicate questions on the potential of PET for *(i)* the monitoring of the proton range, *(ii)* the verification of the lateral position of the irradiation field as well as *(iii)* the detection of possible positioning inaccuracies or local tissue modifications within the patient during fractionated therapy. The first topic was deeply investigated by means of mono-energetic and SOBP irradiation of homogeneous PMMA phantoms at steps of initial kinetic energy values corresponding to range differences less than 1 mm (section 5.3.3.2). For the second purpose a special thick plastic phantom with slits for insertion of photographic emulsions was designed. In this way the spatial distribution of proton induced β^+-activity could be detected simultaneously to the independent film measurement of the dose lateral distribution at several penetration depths, as illustrated in section 5.3.3.3. The last issue was preliminarily investigated by means of a mono-energetic irradiation of an inhomogeneous phantom. This allowed to study the production of β^+-emitting target fragments in different materials as well as to assess the sensitivity of the proton induced positron radioactivity to density gradients and tissue stoichiometry, as reported in section 5.3.3.2.

The description of the experimental set-up and of the common methods used for data analysis are given

in the following two sections. Details on the specific irradiation are separately reported together with the presentation of the results in section 5.3.3. The latter has been subdivided into the three major topics for the purpose of therapy monitoring: *1)* the intensity of detectable PET signal produced by proton compared to carbon ion irradiation as well as *2)* the depth and *3)* the lateral distributions of the proton induced β^+-activity.

5.3.1   Experimental set-up

In all the measurements pencil-like proton beams of about $10 - 15\,\mathrm{mm}$ diameter (FWHM) with initial energy ranging within the $110 - 215\,\mathrm{MeV}$ interval at intensities of approximately $(1 - 5) \cdot 10^8\,p/\mathrm{s}$ were extracted from the heavy ion synchrotron of GSI. The beams were stopped in targets of organic plastic placed on the patient couch in the middle of the two in-beam positron camera heads (figure 2–12 and 5–3). In almost all acquisitions $9 \times 9 \times 20\,\mathrm{cm}^3$ PMMA blocks with the long edge parallel to the beam were irradiated. Two special phantoms were used only for the experiments on lateral position verification with simultaneous exposure of photographic emulsions and for the activation of an inhomogeneous target. They will be described in a dedicated section. The irradiation strategy and the vertical position of the targets were always selected in such a way to produce compact β^+-activity distributions in the mid-plane of the PET scanner in order to avoid limited angle artifacts as far as possible. In most of the measurements the phantom position along the beam direction was chosen in order to centre the expected β^+-activity distribution in the field of view of the positron camera. Only for the more delicate investigation of the range resolution power of PET the predicted position of the activity distal edge was carefully adjusted to the centre of the FOV, which exhibits the best imaging properties (e.g. spatial resolution and sensitivity). In all cases the laser alignment system of the treatment room was exploited. In addition, a PET scan with a ^{22}Na point source placed on the entrance face of the targets was performed prior to the irradiation. This allowed to recover with high accuracy the front face position of the object with respect to the imaged β^+-activity depth profile for the data analysis. The targets were typically irradiated for an average time of 10 minutes. The in-beam PET acquisition was in general prolonged over $10 - 20$ minutes after stopping the irradiation. In this way decays of short-lived (e.g. ^{10}C, ^{15}O) and long-lived (^{11}C) isotopes could be collected with very good statistics ($\simeq 10^6 - 10^7$ true coincidences, i.e. more than one order of magnitude than in typical treatment situations). The data were registered in list mode with time stamps every $10\,\mathrm{ms}$ for dynamic acquisition. This further enables analysis in different time windows. In all the irradiation the time structure of the beam was approximately the same as for carbon ion therapy: about $1 - 2\,\mathrm{s}$ particle extraction (spill) and $3 - 4\,\mathrm{s}$ extraction pause. The
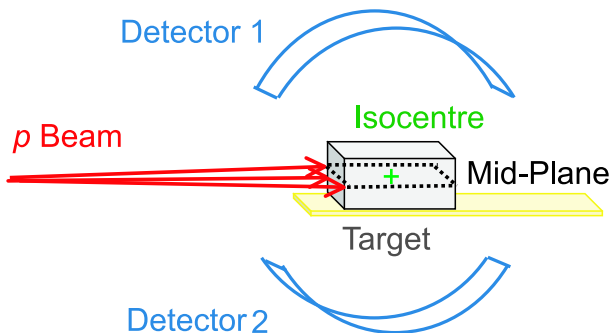
Figure 5–3: *Schematic display of the experimental set-up. Non-scanned pencil-like proton beams were delivered to the isocentre, coinciding with the centre of the positron camera FOV. In case of scanning, the beam was moved only in the lateral dimension restricted to the mid-plane of the tomograph.*

proton beam had furthermore a microstructure similar to that of the carbon ion beam, because of the same longitudinal phase compression and slow resonant extraction procedure from the accelerator. Hence, noise originating from the physical reason explored in chapter 4 for carbon ions was also observed in the PET events acquired during proton irradiation. Therefore, the information on the status of the irradiation (beam on/off) was recorded and used in order to reject the noisy PET events registered during the spills from the data analysis, as done for the processing of coincidences acquired during carbon ion therapy.

5.3.2 Data analysis

Despite the wide spectrum of measurements performed in order to address several issues, common points can be identified in the approaches used for data analysis. The study of the spatial distribution of the proton induced β^+-activity in relation to the localisation of the dose and of the maximum proton range demanded a comparison between the available tools for image reconstruction and a final choice of an optimal strategy. Because of the particular experimental conditions at GSI, a mathematical description of the isotope production and decay rate during the pulsed beam irradiation had to be developed. This was used for the quantitative investigation of the proton and carbon ion induced β^+-activity as well as for the estimate of the ratio between measured events originating from ^{11}C and ^{15}O decays. The latter contributions affect the position of the β^+-activity distal edge related to the maximum proton range. Finally, the feasibility study of proton therapy monitoring based on the comparison between measured and realistically predicted PET images required the refinement of the models used for calculation of positron emitter distributions.

5.3.2.1 Reconstruction and presentation of the proton induced β^+-activity distributions
The PET images and positron radioactivity distributions of all the performed experiments were obtained using the backprojection algorithm with corrections for the attenuation of the γ-rays within the phantom as well as for the spatially variant detection efficiency of the tomograph [Lau99, Hinz00]. Attenuation corrections were calculated from the linear attenuation coefficient of the 511 keV annihilation photons in the phantom along each line of response of the positron camera. The position dependent detection efficiency of the scanner was taken into account by means of weights proportional to the geometrical detection probability. These weights were normalised to the detection efficiency of the tomograph in the centre of the FOV, measured to be 2.45 % by means of a ^{22}Na point source of known activity. The backprojection approach was preferred to a complete iterative MLEM tomographic reconstruction [Lau99] since it is simple, quantitative and artifact free. This is however true only for the chosen experimental conditions leading to β^+-activity distributions confined to the mid-plane of the PET scanner. An additional remarkable advantage of the selected algorithm is the low computing time. Only 1 min was necessary against 120 min and even twice the time when using the MLEM reconstruction without or with scatter corrections [Pön03b], respectively, for the processing of a data set of $5.7 \cdot 10^6$ true coincidences and a typical image space of $230 \times 80 \times 90$ voxels of 1.6875 mm edge size (i.e. one fourth of the detector crystal pitch) on an Intel® Xeon™ 2.20 GHz CPU. According to the intrinsic spatial resolution of the positron camera the backprojection algorithm furthermore ensures a satisfying spatial resolution in the considered central plane. Values of about $7 - 8$ mm FWHM against $5 - 6$ mm after MLEM reconstruction were obtained from measurements with ^{22}Na point sources. However, for the delicate issue of the range resolving power and lateral position verification, the independence of the results on the image reconstruction algorithm was carefully checked, as shown in the results. Obviously, different approaches for data processing may introduce in the final PET images slight discrepancies which are, however, beyond the purpose of the presented experimental feasibility studies.

In the following the PET images and the β^+-activity depth or lateral profiles are always displayed in

the mid-plane of the positron camera FOV. Depth profiles of activity distributions imaged during the first experiment were projected onto the central axis, in order to rule out effects due to the slight beam position instabilities. In all the other cases, the depth profiles were averaged over ± 5 voxels around the central beam axis.

5.3.2.2 Extraction of isotope production rates from the measured PET data

A quantitative comparison of the proton and carbon ion induced β^+-activity distributions requires the reliable estimation of the production rates of the β^+-active isotopes from the measured PET data (figure 5–4). This procedure has to be independent on the irradiation parameters. Furthermore, the study of the dynamic variation of the $^{11}C/^{15}O$ decay ratio during the pulsed beam delivery has to be feasible. For these purposes attention has been particularly focussed on the production rates of ^{11}C, ^{15}O and ^{10}C, which are the most abundant positron emitting isotopes formed in the considered irradiation of organic plastic. Due to the uselessness of the noisy data acquired during the beam bursts as well as the too short duration of the extraction pauses between the pulses for time analysis of the activity decay (figure 5–4, left), the following dedicated approach tailored to mono-energetic irradiation has been developed.

(i) The *relative* amount $N_{^{11}C}$, $N_{^{15}O}$ and $N_{^{10}C}$ of the isotopes of interest present at the end of the irradiation $\bar{t}$ has been deduced from a non-linear fit of the measured activity decay $A(t)$ after stopping the irradiation (figure 5–4, right):

$$A(t) = \lambda_{^{11}C}N_{^{11}C}e^{-\lambda_{^{11}C}(t-\bar{t})} + \lambda_{^{15}O}N_{^{15}O}e^{-\lambda_{^{15}O}(t-\bar{t})} + \lambda_{^{10}C}N_{^{10}C}e^{-\lambda_{^{10}C}(t-\bar{t})}, \quad t > \bar{t} \tag{18}$$

where λ and N are the decay constants and fitting parameters, respectively. The adjective *relative* emphasizes the PET-system dependence of this estimate, not yet corrected for the attenuation of the annihilation photons within the phantom and for the detection efficiency of the tomograph in opposition to the *absolute* values discussed later.
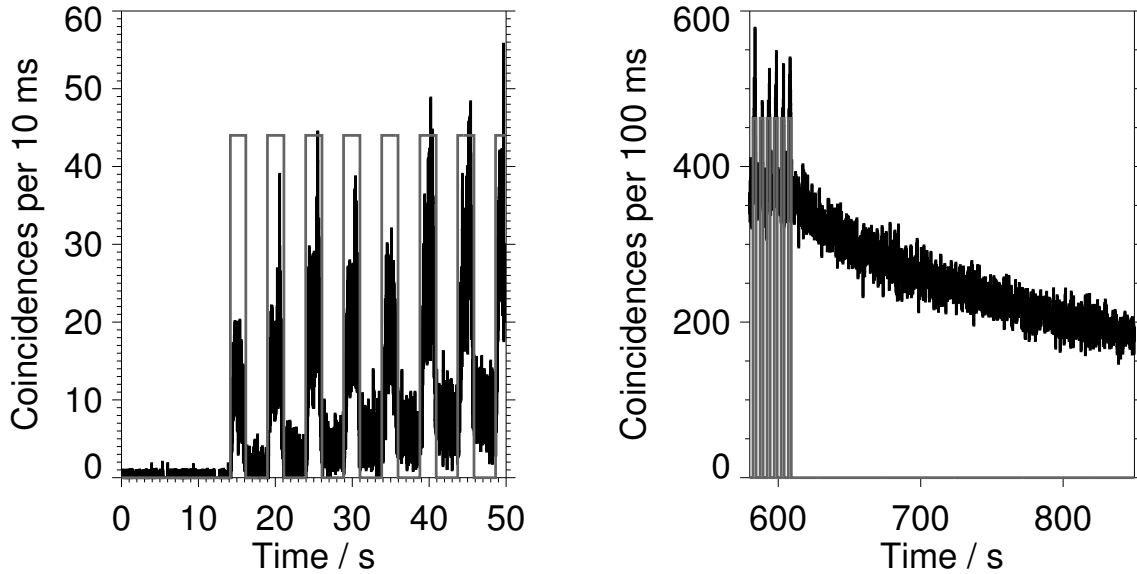
Figure 5–4: *Example of coincidence rate acquired at the beginning (left) and at the end (right) of a mono-energetic proton irradiation. The beam extractions (spills) are marked by the rectangular pulses displayed in grey.*

(*ii*) The relation between the isotope abundance at the end of the irradiation and the production rate during beam extraction has been established by means of a mathematical description of the activity accumulation and decay during the pulsed beam irradiation. Such a description is particularly feasible in the special case of mono-energetic irradiation without beam scanning (addressed in the following as 1D), leading to the same spatial distribution of positron emitters produced at each beam burst. The underlying principle is the assumption of a constant isotope production rate during particle extraction. This is feasible because of the much longer half-life of the isotopes of interest in comparison to the time scale of the intensity variations and fluctuations during the spill. Furthermore, due to the quite stable operation of the synchrotron the irradiation conditions can be assumed to be constant with fixed duration of spills and pauses as well as the same number of extracted protons at each pulse. Under these approximations the number $K_{l,j}$ of nuclei of species l present at the end of the j-th spill can be described as:

$$K_{l,j} = K_{l,j-1}e^{-\lambda_l(t_p+t_s)} + \frac{P_l}{\lambda_l}(1 - e^{-\lambda_l t_s})$$
$$K_{l,1} = \frac{P_l}{\lambda_l}(1 - e^{-\lambda_l t_s}) \tag{19}$$

where P_l is the production rate for the isotopes of interest $l \,\epsilon\, \{^{11}\text{C},\ ^{15}\text{O},\ ^{10}\text{C}\}$ and t_p and t_s are the average pause and spill duration, respectively. From this recursive system of equations follows a first expression for the production rate as:

$$P_l = \frac{\lambda_l K_{l,\mathcal{T}}}{(1 - e^{-\lambda_l t_s}) \sum_{i=1}^{\mathcal{T}} e^{-\lambda_l(i-1)(t_p+t_s)}} \tag{20}$$

where $K_{l,\mathcal{T}}$ is the *relative* amount of isotopes of species l present after the last spill $\mathcal{T}$, hence given by $N_{^{11}\text{C}}$, $N_{^{15}\text{O}}$ and $N_{^{10}\text{C}}$ resulting from *(i)*.

In a second more refined approach the specific production rate $P_{l,j}$ for each j-th spill was deduced from the total activity A_j measured at the end of the spill and the relative contribution f_l of the l-th isotope to the estimated amount of activity $\mathcal{A}_j$ produced in the j-th spill:

$$P_{l,j} = \frac{\mathcal{A}_j f_l}{1 - e^{-\lambda_l t_{s,j}}}$$
$$\mathcal{A}_j = A_j - \sum_l \sum_{i=1}^{j-1} P_{l,i}(1 - e^{-\lambda_l t_{s,i}})e^{-\lambda_l \sum_{m=1}^{j-i}(t_{s,m+i}+t_{p,m+i-1})} \tag{21}$$

where f_l was approximated by the expression $\lambda_l P_l / \sum_k \lambda_k P_k$, with P_l extrapolated from the predictions of equation (20). This second formula can lead to a slight overestimation of the individual isotope production rate, since it attributes all the experimental β^+-activity to ^{11}C, ^{15}O and ^{10}C. On the other hand, it accounts for possible changes of the irradiation conditions, since it directly uses the individual time duration $t_{s,j}$ and $t_{p,j}$ of each spill and pause as well as the coincidence rate measured after each spill and not only the final activity at the end of the irradiation. For comparison of the two model predictions the measured average count rate per second cps_j registered within each j-th pause during irradiation was compared to that deduced from the production rate estimations $L_{l,j}$ set to $P_l \,\forall j$ from equation (20) and to the average $\langle P_{l,j}\rangle \,\forall j$ as well as to the individual $P_{l,j}$ from equation (21), respectively, according to the expression:

$$cps_j = \sum_l \left\{ \sum_{i=1}^{j} \left[\frac{L_{l,i}(1 - e^{-\lambda_l t_{s,i}})}{\lambda_l} e^{-\lambda_l \sum_{m=1}^{j-i}(t_{s,m+i}+t_{p,m+i-1})} \right] \frac{(1 - e^{-\lambda_l t_{p,j}})}{t_{p,j}} \right\} \tag{22}$$

As shown in figure 5–5 a rather good agreement with maximum deviations of about 10 % was found, hence supporting the reliability and consistency of the models based on equations (20) and (21).
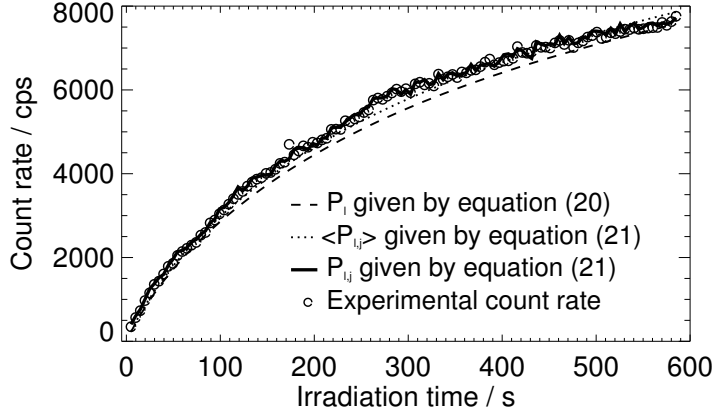
Figure 5–5: *Mean count rate (in counts per second, cps) measured during the beam pauses of a proton irradiation in comparison to the predictions resulting from the production rate estimates based on equations (20), (21) and (22).*

(*iii*) For the *absolute* quantitative comparison of the proton and carbon ion induced β^+-activity, the production rate estimation *relative* to the measured PET events had to be corrected for the attenuation of annihilation photons within the phantom and for the spatially varying detection efficiency of the PET scanner. Furthermore, the different spatial distributions of β^+-activity induced by the two different projectiles had to be taken into account. For this reason a local correction factor $c(\mathbf{r})$ dependent on the position $\mathbf{r}$ within the image-space has been introduced as the ratio of the activity values $A_u(\mathbf{r})$ and $A(\mathbf{r})$ obtained from the measured data by backprojection without and with the two corrections for attenuation and detection efficiency, respectively:

$$c(\mathbf{r}) = \frac{A_u(\mathbf{r})}{A(\mathbf{r})} \tag{23}$$

An average correction factor $\mathcal{C}$ has been deduced from the weighted integral of $c(\mathbf{r})$ over the corrected spatial activity distribution for each measured data set as:

$$\mathcal{C} = \int d\mathbf{r}\, c(\mathbf{r})\, p(\mathbf{r}) = \frac{\int d\mathbf{r} A_u(\mathbf{r})}{\int d\mathbf{r} A(\mathbf{r})} \quad \text{for} \quad p(\mathbf{r}) = \frac{A(\mathbf{r})}{\int d\mathbf{r}\, A(\mathbf{r})} \tag{24}$$

The *absolute* production rates have been therefore obtained by dividing the *relative* P values calculated according to the methods described in (*ii*) by $\mathcal{C}$. Scatter corrections have not been taken into account for this estimate, since the number of events located outside the beam path due to Compton scatter has been found to be negligible in the backprojected images. Furthermore, the contribution of scattering is expected to be comparable for the proton and carbon ion induced β^+-activity distributions considered in the presented experiments.

(*iv*) The ratio between ^{11}C and ^{15}O decays has been deduced from the estimate of the average isotope production rate in spill P_l. This allows to separate the amount $\mathcal{D}_{j,l}$ of isotopes of species l decayed within each j-th pause according to the expression:

$$\mathcal{D}_{j,l} = \frac{P_l(1 - e^{-\lambda_l t_s})}{\lambda_l} \Big[\sum_{i=1}^{j} e^{-\lambda_l(i-1)(t_s+t_p)} \Big] (1 - e^{-\lambda_l t_{p,j}}) \tag{25}$$

For a complete analysis over the entire PET acquisition time, the amount of decays from the l-th isotope species within a Δt interval starting at a time t after stopping the irradiation has been simply obtained from
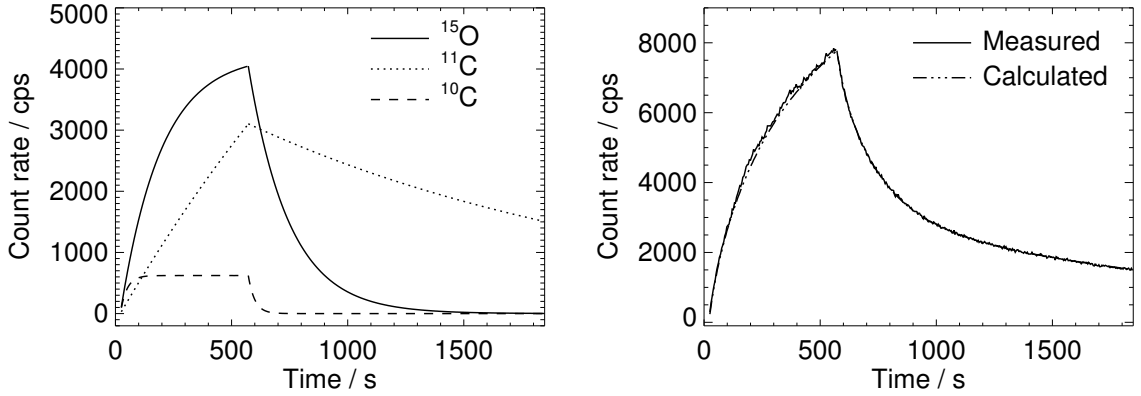
Figure 5–6: *Count rate (cps) contributions derived from the calculated β^+-decays of ^{11}C, ^{15}O and ^{10}C nuclei (left) and comparison of the resulting total value with the coincidence rate measured during and after approximately 10 min proton irradiation of a thick PMMA target (right).*

the isotope abundance N_l at the end of irradiation introduced in (*i*) as:

$$\mathcal{D}_{t,l} = N_l e^{-\lambda_l(t-\bar{t})}(1 - e^{-\lambda_l \Delta t}), \quad t > \bar{t} \tag{26}$$

As an example the predicted contributions of ^{11}C, ^{15}O and ^{10}C decay rates per second detected in the $\simeq 3.5\,$s long pauses of the beam delivery and in time windows Δt of the same duration after the end of a proton irradiation are depicted on the left side of figure 5–6. The resulting total count rate estimate is compared to the measured coincidence rate on the right side of the figure. Again the fairly good agreement over the entire time interval with average deviation below 2 % supports the consistency and reliability of the approach. It can be noticed that in this study no spatial dependent correction of the *relative* isotope production rates has been considered, because of the quite comparable spatial distribution of the ^{11}C and ^{15}O positron emitters of interest produced by proton irradiation.

5.3.2.3 Calculation of β^+-activity distributions induced by proton irradiation

With respect to the first simulation study presented in section 5.2, improved calculation models had to be investigated in order to achieve a more accurate description of the proton induced positron emitter production for a more realistic comparison of measured and calculated β^+-activity depth profiles. The previous approach was entirely based on the FLUKA Monte Carlo code. However, the available comparison between the predictions of the internal models of the program and the experimental partial cross sections for proton interaction on carbon shows an underestimation (up to 30 %) approximately below 70 MeV and an overestimation (again up to 30 %) above about 150 MeV for the main $^{12}C(p,pn)^{11}C$ reaction channel of interest for positron emitter production (figure 5–7). In the typical energy range of relevance for therapy the two opposite trends can compensate on average and result in a fairly good prediction of the total ^{11}C production. This is supported by the rather good agreement between calculations based on FLUKA and off-line PET measurements [Oel96] discussed in [Par00]. Nevertheless, the different dependence of the predicted reaction cross section on the energy affects the slope of the calculated isotope distribution along the proton path. Similar uncertainties of the FLUKA internal models can be furthermore expected for positron emitter production from other reaction channels involving targets different than carbon. The accuracy of generalised intra-nuclear cascade models for generation of light residuals is intrinsically limited, despite the considerably advanced implementation in FLUKA including preequilibrium processes and Fermi Break-up for
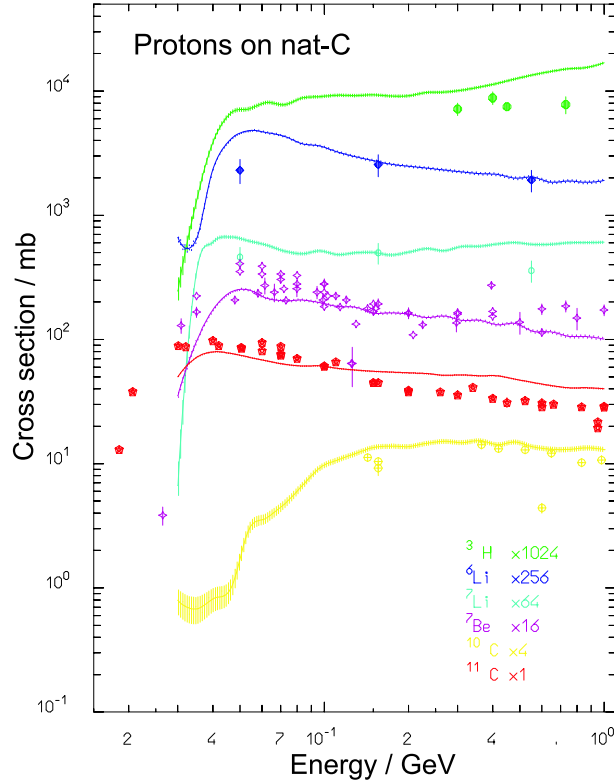
Figure 5–7: *Comparison of the excitation functions predicted by the FLUKA internal models (solid lines) [Fer96] with experimental data (points) [Eph67, Ilj91] for the production of different isotopes by proton bombardment of natural carbon (courtesy of A. Ferrari, CERN).*

light nuclei [Fer96, Fer97]. In order to overcome the limitations of nuclear modelling, a more refined approach tailored to the PET application has been developed, which takes into account available experimental cross sections. Only $^{12}\text{C}(p,pn)^{11}\text{C}$ and $^{16}\text{O}(p,pn)^{15}\text{O}$ interactions have been considered. These are the main reaction channels for the production of the two most abundant positron emitters determining the shape of the β^+-activity profiles measured in the presented experiments, as also expected in typical $5 - 10\,\text{min}$ in-vivo acquisitions during or shortly after a therapeutic session [Vyn93]. This approximation is particularly meaningful for the mostly considered case of PMMA targets, due to the absence of nitrogen as well as the higher content of carbon than oxygen. In this material the contribution to ^{11}C production from the second main $^{16}\text{O}(p,3p3n)^{11}\text{C}$ reaction channel was found to be less than $8\,\%$ according to the cross section values from [Alb62]. Moreover, no significant modification ($< 0.2\,\text{mm}$) was observed in the distal edge position of the total ^{11}C depth distribution when including this contribution, despite the higher energy threshold of the $^{16}\text{O}(p,3p3n)^{11}\text{C}$ reaction. Furthermore, positron emitter production from secondary particles different than protons was also estimated to be negligible, with the most significant contribution from neutrons limited to $1 - 2\,\%$.

The spatial distribution of ^{11}C and ^{15}O nuclei has been obtained by combining internally during run-time the energy dependent cross sections interpolated from the experimental data extracted from [Nuc00] (figure 5–8) with the energy and position dependent proton flux given by the FLUKA code. In figure 5–9 the resulting positron emitter depth profile is compared to the predictions entirely based on the internal models implemented in the two FLUKA versions from 1998 (used for the calculations presented in 5.2) and 1999. The data refer to the simulation of a $140\,\text{MeV}$ proton beam ($\pm\,0.1\,\%$ momentum spread, $10\,\text{mm}$ lateral
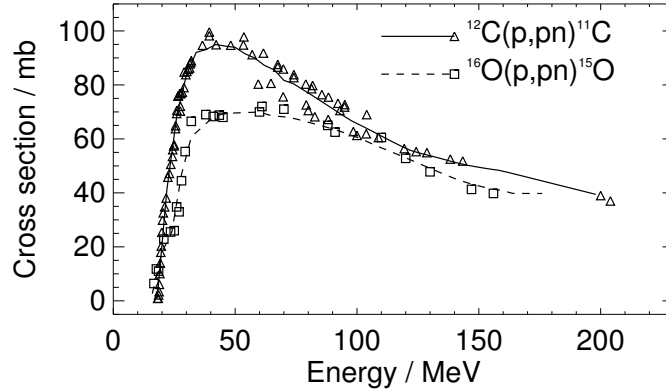
Figure 5–8: *Interpolated values (lines) from experimental cross sections (points) taken from [Aam52, Cra56, Cum63, Hin52, Mea66] and [Alb62, Kit90, Saj85, Val65] for the two main (p, pn) reaction channels leading to the production of ^{11}C and ^{15}O in proton interaction on carbon and oxygen, respectively. The data include the yield stemming from a (p, d) reaction energetically also possible.*

FWHM, no divergence, 10^6 primaries) stopped in PMMA. Clearly the new approach leads to a considerably steeper slope of the isotope production along the penetration depth. The improvement will become evident in section 5.3.3.2 after presentation of the β^+-activity depth profiles obtained from the reconstruction of the measured data. It must be however noticed that the new approach predicts a lower amount of ^{11}C and ^{15}O isotopes with a global reduction up to $\simeq 10 - 20\%$ in the $110 - 175$ MeV energy interval. The reason seems to be the neglection of reaction channels with minor probability in combination with uncertainties (from 5 % to 30 %) as well as discrepancies in the cross sections extrapolated from [Nuc00] and those predicted by the internal models of FLUKA. Nevertheless, both the old method and the new approach lead to a quantitative prediction rather close to the corresponding amount of positron emitters extracted from the experimental data and normalised to the same number of simulated projectiles, as shown in table 5–2. Furthermore, the new method provides a more satisfactory agreement with the measured data with respect to the ^{11}C to ^{15}O production ratio.
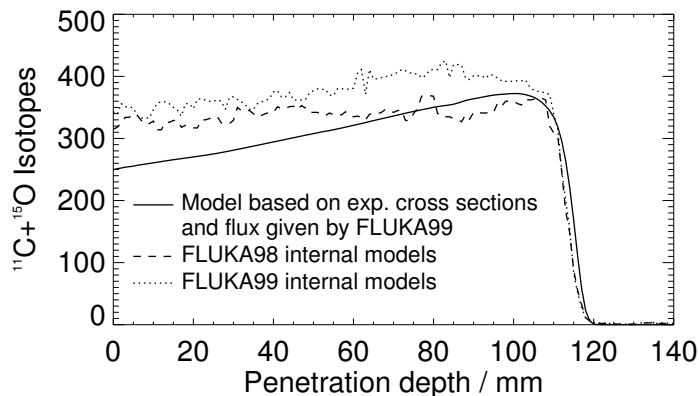
**Figure 5–9:** *Projection onto the beam axis of the ^{11}C+^{15}O production calculated using the new approach with experimental cross sections in comparison to the internal models implemented in FLUKA98 and FLUKA99, respectively, for 10^6 primary protons of 140 MeV initial energy stopped in PMMA.*

Table 5–2: *Ratios between the predicted and the experimentally deduced ^{11}C and ^{15}O isotope production in PMMA. The predictions were obtained by means of FLUKA99 simulations using the new approach with experimental cross sections (r_{exp}) in comparison to the internal models (r_{int}). The absolute isotope production deduced from the measured PET data (section 5.3.2.2) was normalised to the same number of simulated primary projectiles.*

E / MeV	^{11}C		^{15}O	
	r_{exp}	r_{int}	r_{exp}	r_{int}
110	0.9 ± 0.2	0.9 ± 0.3	0.9 ± 0.3	1.3 ± 0.5
140	0.8 ± 0.2	0.9 ± 0.2	0.8 ± 0.3	1.2 ± 0.4
175	0.8 ± 0.3	0.9 ± 0.3	0.8 ± 0.4	1.2 ± 0.6

It should be mentioned that a recent publication of ICRU [ICR00] has proposed different cross sections values (figure 5–10), extensively based on calculations generated by the Los Alamos GNASH model code [You92, Cha99a, Cha99b]. These values have been also addressed as the most reliable source of information in [Bee03]. However, [ICR00] itself recommends to prefer experimental data, whenever available, for PET studies. A comparison of the separate ^{11}C and ^{15}O depth profiles generated by FLUKA when using the two different cross section data sets from [Nuc00] and [ICR00] is illustrated in figure 5–11. After presentation of the reconstructed measured data the preference for the selected approach using the experimental data from [Nuc00] will become evident. Furthermore, the values published by ICRU could not reproduce several trends observed in the measured PET data, as it will be explicitly pointed out in the text. Nevertheless, there is a complete agreement with the conclusions of [Bee03] on the still ongoing need to develop a library of more recent and accurate cross section data for proton induced reactions on the elements of human tissue in the energy range of relevance for therapy. A work on this issue is currently in progress [IAE97]. This knowledge should be further validated by means of PET experiments in pure phantoms.

The spatial distributions of positron emitters predicted according to the described method have been convolved with a Gaussian point spread function of 7 or 5 mm FWHM for comparison with the measured β^+-activity distributions obtained from backprojection or MLEM iterative reconstruction of the acquired
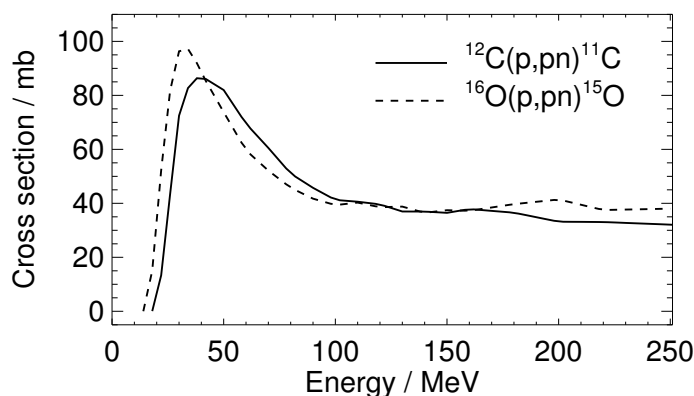
Figure 5–10: *Cross sections values for ^{11}C (solid) and ^{15}O (dashed) production in (p, pn) interaction on carbon and oxygen targets, respectively, recently published in [ICR00].*
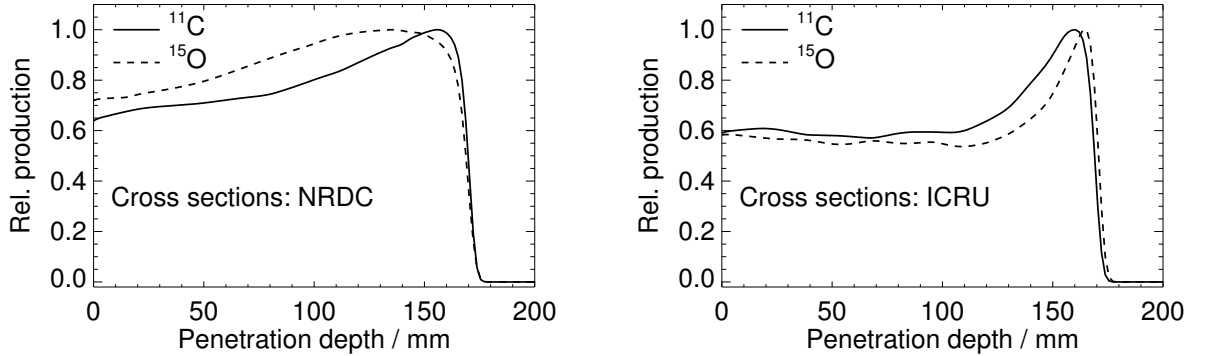
Figure 5–11: *Relative depth distributions of ^{11}C (solid) and ^{15}O (dashed) isotopes calculated by means of FLUKA using cross sections extrapolated from the Nuclear Reaction Data Center (NRDC) [Nuc00] and the ICRU [ICR00] for a mono-energetic proton irradiation of a thick PMMA target at 173.13 MeV initial energy.*

data, respectively. Such an approximation accounts for blurring effects due to the image formation (positron and photon propagation) and data processing on the basis of measurements with positron emitting point sources. Although this approach does not include the explicit propagation of the positrons emitted in the β^+-decays as well as the transport of the annihilation γ-rays for the particular activity sources induced by each specific phantom irradiation, a rather good agreement with the measured data was observed, as shown in section 5.3.3. In all the simulations the beam momentum spread was fixed to $\pm 0.1\%$, according to the synchrotron specifications. In the most delicate investigations on activity depth profiles in relation to the feasibility of PET for proton range monitoring, the $\simeq 2$ mm water equivalent material in the beam line was taken into account by means of a corresponding range reduction. A sub-millimetre accuracy of such correction is however beyond the purpose of this study. When no detailed information was available, a lateral beam profile of 10 mm FWHM and no divergence were assumed. In this case only β^+-activity depth profiles projected onto the central beam axis were considered. In the second run of experiments the better beam quality in combination with a more accurate knowledge of the beam parameters allowed a more realistic beam characterization in the simulations. In this way expected PET images directly comparable with the reconstructed measured data could be predicted. Simulations of scanned fields were also possible on the basis of the FLUKA user-oriented capabilities [Fas02]. In this special case of extended fields the dynamic time course of the irradiation has been also taken into account. This allowed runtime calculations of the fraction of isotopes decayed within the time interval between production and end of the PET acquisition for a better comparison with the measured data. Dose distributions were additionally calculated by means of FLUKA either in cylindrical detectors of 5 mm (10 mm for $E > 180$ MeV) radius and 1 mm depth along the central beam axis or in the same voxel geometry of the PET images for a more straightforward comparison in the case of a sufficient knowledge of the beam parameters.

5.3.3 Results

5.3.3.1 Comparison of proton and carbon ion induced β^+-activity

The β^+-activity production rate induced by proton irradiation has been quantitatively estimated for mono-energetic pencil-like beams stopped in PMMA. Details on the considered irradiation with in-beam PET acquisition are given in table 5–3. The corresponding spatial distributions of the imaged β^+-activity are depicted in figure 5–12. The *absolute* ^{11}C, ^{15}O and ^{10}C isotope production rates during particle extraction
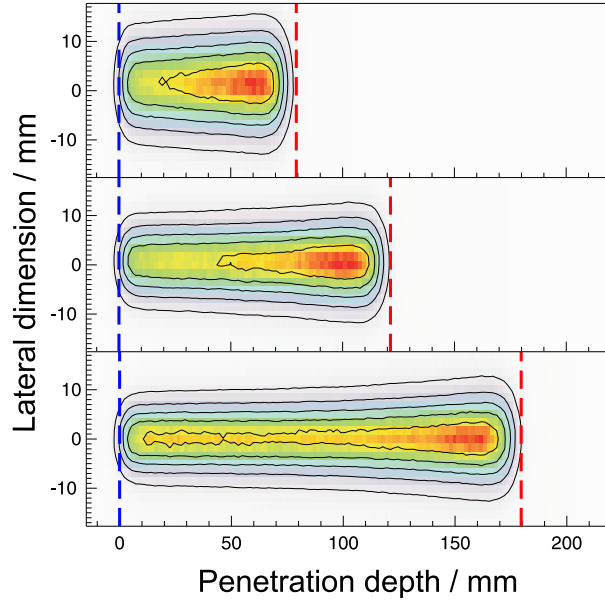
Figure 5–12: *Spatial distributions of the β^+-activity induced by proton beams of 110 MeV (top), 140 MeV (middle) and 175 MeV (bottom) in a PMMA phantom. The left blue lines mark the front face of the target whereas the right red lines indicate the proton range.*

have been determined according to the calculation models described in section 5.3.2.2. For comparison with the carbon ion case, the same analysis has been extended to in-beam PET data acquired during carbon ion irradiation of PMMA phantoms. These measurements had been previously performed in the same experimental set-up with comparable irradiation parameters at energies corresponding to similar penetration depths as in the proton experiment (table 5–4). The estimates of the *relative* isotope production rates and resulting *relative* β^+-activity production rates together with the correction factors $\mathcal{C}$ required for *absolute* quantification are listed in table 5–5. From these values the ratio r of the *absolute* β^+-activity rates produced by proton and carbon ion bombardment of PMMA targets at the same dose level and projectile range has been obtained as:

$$r = 18\ \frac{\mathrm{d}A_p}{\mathrm{d}t}\left(\frac{\mathrm{d}A_{^{12}\mathrm{C}}}{\mathrm{d}t}\right)^{-1}\frac{\mathcal{C}_{^{12}\mathrm{C}}}{\mathcal{C}_p}\frac{I_{^{12}\mathrm{C}}}{I_p}\frac{R_{^{12}\mathrm{C}}}{R_p} \tag{27}$$

where I indicates the beam intensity in particles per second ($I = I_s/t_s$). The factor 18 compensates the lower energy loss of protons in comparison to carbon ions at energies corresponding to the same penetration depth. In dependence on the stopping power calculation model this factor is estimated to lie between 18

Table 5–3: *Parameters of the irradiation and of the PET acquisition (identifier ID, energy E, range R from [ICR93], total number $\mathcal{T}$ of extracted spills, average beam intensity I_s and spill duration t_s, irradiation time t_{ir} including the extraction pauses, measuring time t_{mea} and total amount N_{ev} of valid coincidences detected).*

ID	E / MeV	R / cm	$\mathcal{T}$	I_s / $p\,\mathrm{spill}^{-1}$	t_s / s	t_{ir} / s	t_{mea} / s	N_{ev}
(i)	110	7.9	121	$(1.4 \pm 0.1)\cdot 10^8$	2.123 ± 0.020	595.06 ± 0.01	1958	2734909
(ii)	110	7.9	140	$(2.1 \pm 0.2)\cdot 10^8$	2.125 ± 0.010	688.64 ± 0.01	1616	3844950
(iii)	140	12.1	119	$(2.1 \pm 0.2)\cdot 10^8$	2.129 ± 0.030	587.22 ± 0.01	1848	5357535
(iv)	175	17.9	114	$(1.0 \pm 0.1)\cdot 10^9$	2.228 ± 0.090	592.30 ± 0.01	1777	30348227

72

Table 5–4: *Parameters of the analysed carbon ion irradiation with in-beam PET acquisition. For explanation of the symbols cf. table 5–3.*

ID	E / AMeV	R / cm	$\mathcal{T}$	I_s / ^{12}C spill^{-1}	t_s / s	t_{ir} / s	t_{mea} / s	N_{ev}
(1)	204	7.6	50	$(1.2 \pm 0.1) \cdot 10^8$	2.188 ± 0.006	275.58 ± 0.01	1443	4376057
(2)	212.12	8.1	50	$(2.0 \pm 0.1) \cdot 10^8$	2.169 ± 0.009	222.91 ± 0.01	399	4844180
(3)	212.12	8.1	50	$(1.00 \pm 0.02) \cdot 10^7$	0.798 ± 0.030	271.39 ± 0.01	1443	311818
(4)	259.5	11.4	50	$(1.2 \pm 0.1) \cdot 10^8$	2.189 ± 0.019	275.53 ± 0.01	1380	6538242
(5)	306	15.0	30	$(1.2 \pm 0.1) \cdot 10^8$	2.185 ± 0.008	164.01 ± 0.01	1288	4516059
(6)	343.46	18.1	39	$(2.5 \pm 0.1) \cdot 10^8$	2.180 ± 0.009	173.50 ± 0.01	347	8064358

and 21. The lowest value has been used in order to be cautious in the prediction. Following this choice an average value of (3.2 ± 0.4) has been found for r, whereas no evident dependence on the initial beam energy has been assessed.

The observed activity gain for a proton compared to carbon ion irradiation at the same physical dose and range is in agreement with the expectation of a minimum factor of about 2 predicted in the initial simulation study presented in section 5.2. The ratio should further increase in real therapeutic applications since the relative biological effectiveness of carbon ions is considerably higher than that of protons [Wam99, Kra99]. An additional enhancement of the proton induced activity may be also foreseen for PET measurements in typical $5 - 10$ minutes acquisition times during a patient treatment, dominated by the contribution of ^{15}O decays. Such an expectation is supported by the observed higher ^{15}O to ^{11}C production rate ratio in the same target for proton in comparison to carbon ion irradiation (cf. table 5–5) in combination with the larger relative abundance of oxygen in tissue than in PMMA (e.g. 65 % oxygen against 18 % carbon in human body according to [Ose65]).

The reliability of the *relative* amounts of proton induced positron emitters quoted in table 5–5 is rather well supported by the comparison with activation measurements performed in Brookhaven [Ben75]. In this experiment the authors irradiated for a short period $(30\,\mu\mathrm{s})$ three samples of PMMA of $1\,\mathrm{cm}^3$ dimension using protons of 200 MeV. The decay curves acquired starting within one minute after the irradiation end were fitted by means of a function resembling equation (18). The decay constants of ^{11}C and ^{15}O were set

Table 5–5: *Relative isotope production rates P with corresponding uncertainties Δ and relative β^+-activity production rates dA/dt deduced from the measured PET events for proton and carbon ion irradiation of PMMA phantoms. Division of the relative values by the correction factors $\mathcal{C}$ produces absolute estimates.*

Proj.	E / AMeV	ID	$\mathcal{C}$ $\times 10^{-3}$	$P_{^{11}\mathrm{C}}$ / s^{-1}	Δ / %	$P_{^{15}\mathrm{O}}$ / s^{-1}	Δ / %	$P_{^{10}\mathrm{C}}$ / s^{-1}	Δ / %	dA/dt / Bq s^{-1}
p	110	(i)	8.3 ± 0.4	12726	10	4342	15	321	35	43 ± 8
p	110	(ii)	8.2 ± 0.4	17984	10	6546	15	723	30	73 ± 14
^{12}C	204	(1)	7.3 ± 0.4	39607	8	7664	15	2984	20	173 ± 29
^{12}C	212.12	(2)	7.9 ± 0.3	76525	10	15419	12	5778	40	339 ± 95
^{12}C	212.12	(3)	7.9 ± 0.3	10099	4	1909	15	754	30	44 ± 10
p	140	(iii)	7.8 ± 0.3	26120	5	9440	10	1138	15	109 ± 12
^{12}C	259.5	(4)	7.3 ± 0.4	58611	5	12325	10	4590	20	268 ± 41
p	175	(iv)	7.2 ± 0.3	150670	10	51209	15	5518	35	575 ± 120
^{12}C	306	(5)	6.6 ± 0.3	66485	5	14806	15	5303	15	312 ± 43
^{12}C	343.36	(6)	6.9 ± 0.3	157213	10	39816	5	12052	20	749 ± 107

by the authors to $(29.47\,\text{min})^{-1}$ and $(2.98\,\text{min})^{-1}$, respectively. The third one was left as a free parameter accounting for a background component afterwards identified with ^{10}C on the basis of the fitted half-life of $0.3\,\text{min}$. From the analysis the authors obtained an average value of (3.4 ± 0.2) for the ratio $\dot{N}_{^{15}\text{O}}/\dot{N}_{^{11}\text{C}}$ of the ^{15}O and ^{11}C decay rates at the end of the irradiation. This estimate refers to a proton beam not stopped in the thin target. However, a comparison with the ^{15}O to ^{11}C activity ratio averaged on all the penetration depth in the presented in-beam PET experiment is still meaningful, because of the comparable energy dependence of the cross sections for the ^{12}C$(p,pn)^{11}$C and ^{16}O$(p,pn)^{15}$O reaction channels (cf. figure 5–8). Neglecting the decay within the extremely short irradiation time τ of $30\,\mu$s, the expected ^{15}O to ^{11}C decay rate ratio was deduced from the proton induced isotope production rates given in table 5–5 as:

$$\frac{\dot{N}_{^{15}\text{O}}}{\dot{N}_{^{11}\text{C}}} = \frac{(2.98)^{-1}}{(29.47)^{-1}} \frac{P_{^{15}\text{O}}\,\tau}{P_{^{11}\text{C}}\,\tau} \tag{28}$$

The resulting values of (3.5 ± 0.9), (3.6 ± 0.5) and (3.4 ± 0.8) for the 110, 140 and 175 MeV proton irradiation, respectively, are in good agreement with the work of [Ben75]. The same approach has been also applied to the estimate of the initial ^{10}C to ^{15}O decay rate ratio, using for consistency the $(\ln 2/0.3)\,\text{min}^{-1}$ value adopted in [Ben75] for the decay constant of ^{10}C. This latter comparison is however more affected by the different experimental conditions. In fact the qualitatively different energy dependence of the cross sections in combination with the higher energy threshold for ^{10}C with respect to ^{15}O generation in proton interaction on carbon and oxygen, respectively (cf. figure 5–7 and figure 5–8), leads to the reduction of the ^{10}C to ^{15}O production ratio along the penetration depth in thick PMMA targets. This can explain the lower $\dot{N}_{^{10}\text{C}}/\dot{N}_{^{15}\text{O}}$ mean values of (0.6 ± 0.3), (0.8 ± 0.2) and (0.7 ± 0.4) deduced from the PET measurements at 110, 140 and 175 MeV initial proton energies in comparison to the average ratio of 1.6 obtained at 200 MeV in [Ben75]. Furthermore, the accuracy of ^{10}C identification from time analysis of activity decay curves dominated by ^{15}O and ^{11}C contributions has unavoidable limitations in this work as well as in [Ben75]. Hence, the presented comparison is still satisfactory and indeed supports the reliability of the *relative* isotope production rates deduced from the proton experiment. Finally, it should be also reminded the rather good correspondence shown in table 5–2 for the *absolute* estimate of ^{11}C isotope production deduced from the measured PET data in comparison to the FLUKA predictions. The latter have been found in the same order of magnitude of experimental values extracted from [Oel96], as pointed out in [Par00].

5.3.3.2 Proton induced β^+-activity depth distributions

The depth distribution of positron emitting nuclei activated by proton irradiation is the most crucial quantity for therapy monitoring since it carries the most valuable information on the longitudinal localisation of the beam and of the dose delivery. In particular it determines the possibility of in-vivo range monitoring. This is of utmost importance in delicate irradiation fields in close vicinity to critical organs. As in the carbon ion case, the precision of proton range calculations in treatment planning is conditioned by the unavoidable limitations in the use of CT calibration curves, especially in presence of tissue inhomogeneities in the beam path. Average uncertainties of $1-3\,\text{mm}$ in typical treatment situations have been reported [Scha98]. Therefore, the potential benefit of PET for this critical issue has been the subject of the most extensive experimental investigations. In the following measured and predicted β^+-activity depth profiles induced by proton irradiation of homogeneous targets are presented and compared, starting from mono-energetic pencil-like beams up to the more realistic case of SOBP and scanned (2D) fields. The corresponding achievable resolution for range monitoring is separately addressed in a dedicated section. Finally, the impact of dynamic effects due to different ^{11}C/^{15}O ratio as well as a mono-energetic irradiation of an inhomogeneous target with tissue equivalent inserts are described and discussed.
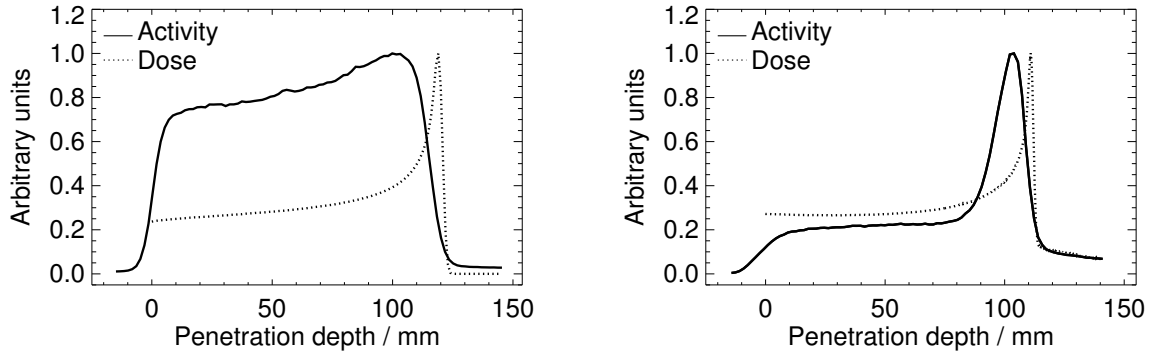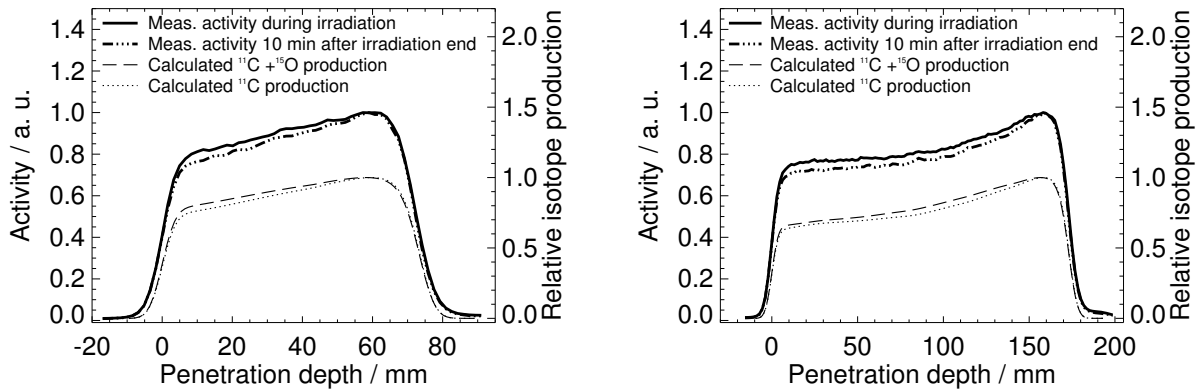
Figure 5–13: *Measured β^+-activity depth profiles (solid line) for proton (left) and carbon ion (right) irradiation of PMMA targets at 140 MeV and 259.5 AMeV initial energy, respectively. The dotted line shows the calculated relative dose distributions.*

Non-scanned mono-energetic irradiation

The depth distribution of the imaged positron radioactivity induced by a 140 MeV pencil-like proton beam is compared in figure 5–13 to the one produced by a carbon ion irradiation of similar penetration depth. The corresponding dose distributions calculated by means of the FLUKA and POSGEN codes in the proton and the carbon ion case, respectively, are additionally displayed. The much poorer spatial correlation between the β^+-activity and the dose depth profiles in the proton case is evident. Due to the lack of projectile fragments no maximum of positron radioactivity is formed at the end of the primary proton range (figure 5–13, left) in contrast to the carbon ion case (figure 5–13, right). Furthermore, the proton induced activation of the target nuclei of the irradiated medium vanishes in the last few millimetres of the primary particle path (figure 5–13, left) as expected, because of the energy thresholds of the nuclear reactions. However, there is still a unique relation between the location of the β^+-activity distal fall-off and the position of the Bragg-peak as well as the primary proton range. In order to assess the feasibility of PET monitoring based on the comparison between measured and predicted positron radioactivity distributions, the reconstructed depth profiles of β^+-activity have been compared to those calculated on the basis of the approach described in section 5.3.2.3. A rather good agreement was observed, as shown in figure 5–14. First investigations on
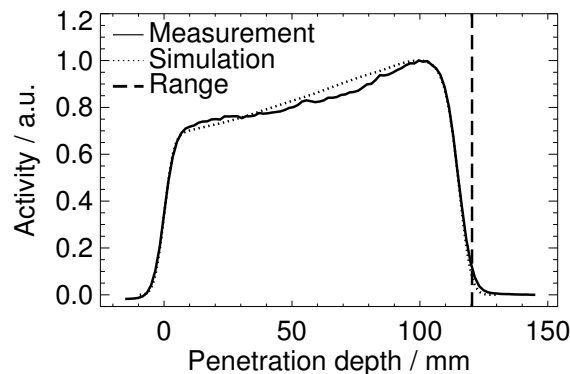
Figure 5–14: *Measured (solid line) and predicted (dotted line) β^+-activity profile along the penetration depth for a 140 MeV proton beam stopped in PMMA. The expected range from [ICR93], corrected for the material in the beam path as the simulated data (cf. section 5.3.2.3), is shown by the dashed line.*

Figure 5–15: *The influence of the different (p, pn) excitation functions for ^{12}C and ^{16}O targets on the β^+-activity depth profiles induced in PMMA by protons at initial energies of 110 MeV (left) and 175 MeV (right). The thick solid and dashed-dotted lines show profiles of β^+-activity measured by means of PET during the 10 min of irradiation and later than 10 min after stopping the beam delivery, respectively. The dashed and dotted lines (referring to the right axis scale) depict the calculations including or ruling out the ^{15}O contribution, respectively.*

the influence of the ^{11}C to ^{15}O ratio on the β^+-activity distributions were also performed by reconstructing only two subsets of the acquired data: one for coincidences detected during the 10 minutes of irradiation and the other for the events recorded later than 10 minutes after finishing the irradiation. According to this selection the first data set mainly contains decays from ^{15}O and ^{11}C, whereas the contribution from ^{15}O is drastically reduced in the second one. The comparison with predicted positron emitter distributions containing ^{15}O or not, respectively, showed again a fairly good agreement, as illustrated in figure 5–15. The larger discrepancy between measurement and prediction occurs for the highest beam energy in the entrance channel and is ascribed to the poor knowledge of cross sections in this energy range (cf. figure 5–8). In both measurements and calculations the presence or absence of ^{15}O mostly influences the proximal slope of the β^+-activity depth profiles. Despite the about $3.5 - 3.8$ MeV higher energy threshold of the main (p, pn) reaction channel on ^{12}C in comparison to ^{16}O targets according to [Vyn93, Oel96, Bee03] and the used experimental data from [Nuc00], only minor deviations of less than 0.25 mm were observed for the position of the 50% level of the distal fall-off. The latter was found at about $5 - 6$ mm lower penetration depth than the primary proton range, in consistency with previous off-line phantom investigations performed with PET scanners of comparable $5 - 8$ mm FWHM spatial resolution for mono-energetic proton irradiation in a similar $62 - 110$ MeV energy range [Vyn93, Oel96]. Although effects due to the $^{11}C/^{15}O$ ratio will be more extensively addressed in a dedicated section, the capability of the model calculation to reproduce the experimental trend should be emphasised (cf. separation in the proximal part of the calculated isotope depth distributions in figure 5–15). The same would not be true when using the cross section values extracted from [ICR00], as evident from the separate ^{11}C and ^{15}O depth profiles illustrated in figure 5–11, showing an almost identical relative production in the entrance channel for an irradiation at a similar energy as in figure 5–15, right.

Non-scanned SOBP irradiation

Non-scanned (1D) SOBP dose distributions have been dynamically formed by repainting a proper sequence of mono-energetic pencil-like proton beams. At each repaint the energies were delivered in increasing order, as done for patient treatments in carbon ion therapy at GSI. Figure 5–16 shows the β^+-activity depth profile measured for an irradiation field built by 11 energy steps ranging between 156.06 MeV and 171.62 MeV and corresponding to 3 mm range separation in water. Clearly the superimposition of several pencil-like beams
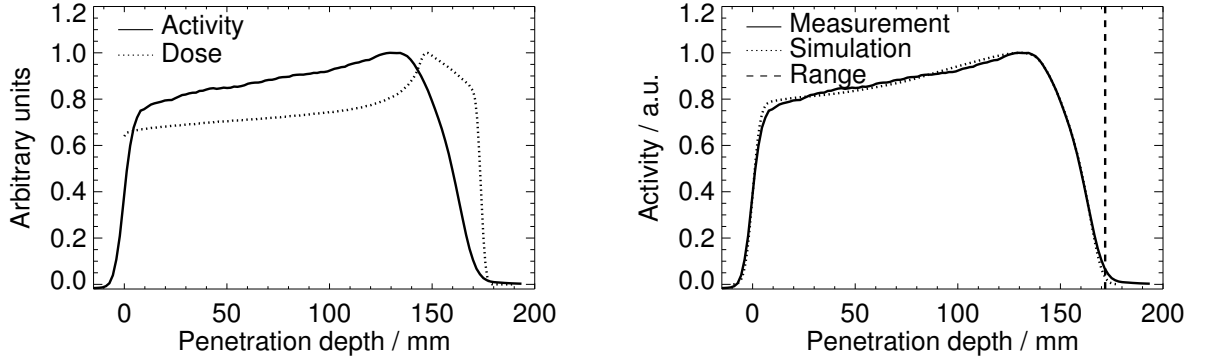
Figure 5–16: *Measured β^+-activity depth profile (solid line) for a 1D SOBP field formed by 11 mono-energetic pencil-like beams of initial energies within the 156.06 – 171.62 MeV interval stopped in PMMA. The dotted lines show the predicted dose (left) and positron emitter (right) depth distributions.*

results in a much smoother fall-off of the positron emitter depth profiles in comparison to the previously analysed mono-energetic case. The effect is furthermore enhanced by the underweighting of the highest energy contributions, indicated by the decreasing distal slope of the dose in the SOBP region (figure 5–16, left). However, the considered distribution is close to realistic treatment situations according to the treatment planning techniques for multifield irradiation. Moreover, the smoothness of the β^+-activity distal shoulder strongly depends on the width of the SOBP region, only approximately 26 mm wide in the presented experiment. The implications on the possibility of range monitoring will be addressed in a following dedicated section. However, it should be noticed the observed reasonable agreement with the prediction (figure 5–16, right).

*Scanned mono-energetic and SOBP fields*

Two-dimensional mono-energetic and SOBP irradiation of (maximum) energy of 171.62 MeV were delivered by means of the raster scanning system moved at lateral steps of 4 mm from -20 mm to 20 mm with respect to the isocentre (figure 5–3 and table 5–6). The corresponding 2D dose distributions are shown in figure 5–17. The measured PET images are compared in figure 5–18 to those predicted including the dynamic effects of the beam delivery in the calculation. A reasonable agreement is observed, especially with respect to the lateral extension of the irradiated fields. However, the results are affected by the not yet optimal experimental conditions for scanned beams. In fact the proton intensity provided by the GSI synchrotron is in general low and the beam delivery control and raster scan system are optimised for operation with carbon ions.

Table 5–6: *Parameters of the beam delivery and PET acquisition (beam energy E, maximum range R, number of repaints $\mathcal{P}$ times the number of energy steps $\mathcal{E}$ for each repaint, number of primary protons N_p, irradiation time t_{ir}, measuring time t_{mea} and amount of detected coincidences N_{ev}) for the 2D mono-energetic (first row) and SOBP irradiation (second row). Each energy step was delivered to 11 lateral scan positions at 4 mm separation.*

| E / MeV	R / cm	$\mathcal{P} \times \mathcal{E}$	N_p	t_{ir} / s	t_{mea} / s	N_{ev}
171.62	17.35	10×1	$1.1 \cdot 10^{10}$	307.65 ± 0.01	1312	2298396
156.06 − 171.62	17.35	3×11	$9.3 \cdot 10^{9}$	434.20 ± 0.01	1383	1926558
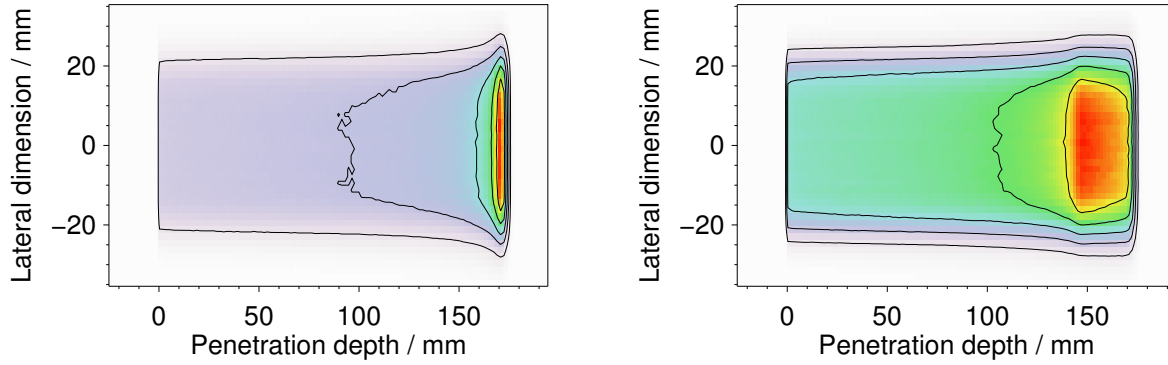
Figure 5–17: *Calculated dose distributions for the 2D mono-energetic (left) and SOBP (right) irradiation of PMMA phantoms at (maximum) energy of 171.62 MeV.*
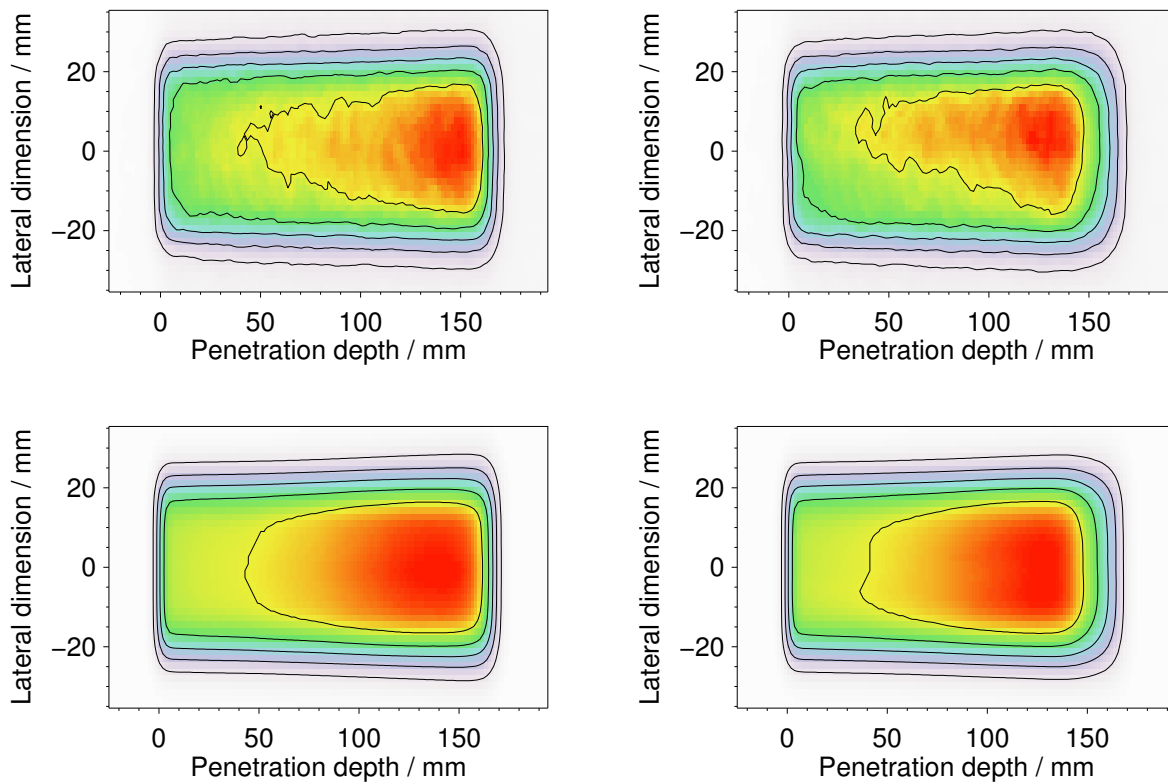
Figure 5–18: *Measured PET images (top) and expected spatial distributions of detected decays from the produced β^+-emitters (bottom) for the 2D mono-energetic (left) and SOBP (right) irradiation of PMMA.*

During the experimental run a compromise had to be found for the amount of particles applied to each scan position, which determines the scanning speed at the given low beam intensity. The number of deliverable protons per scan position was however limited by the sensitivity of the beam monitor, especially for the detection of the up to one order of magnitude reduced amount of low energy protons with respect to the beams of maximum energy forming the SOBP field. As a first consequence of these experimental constraints, the position accuracy of the beam delivery could not be optimal [Nau03]. This affected in particular the SOBP irradiation, resulting in the observed pronounced lateral asymmetry of the measured β^+-activity
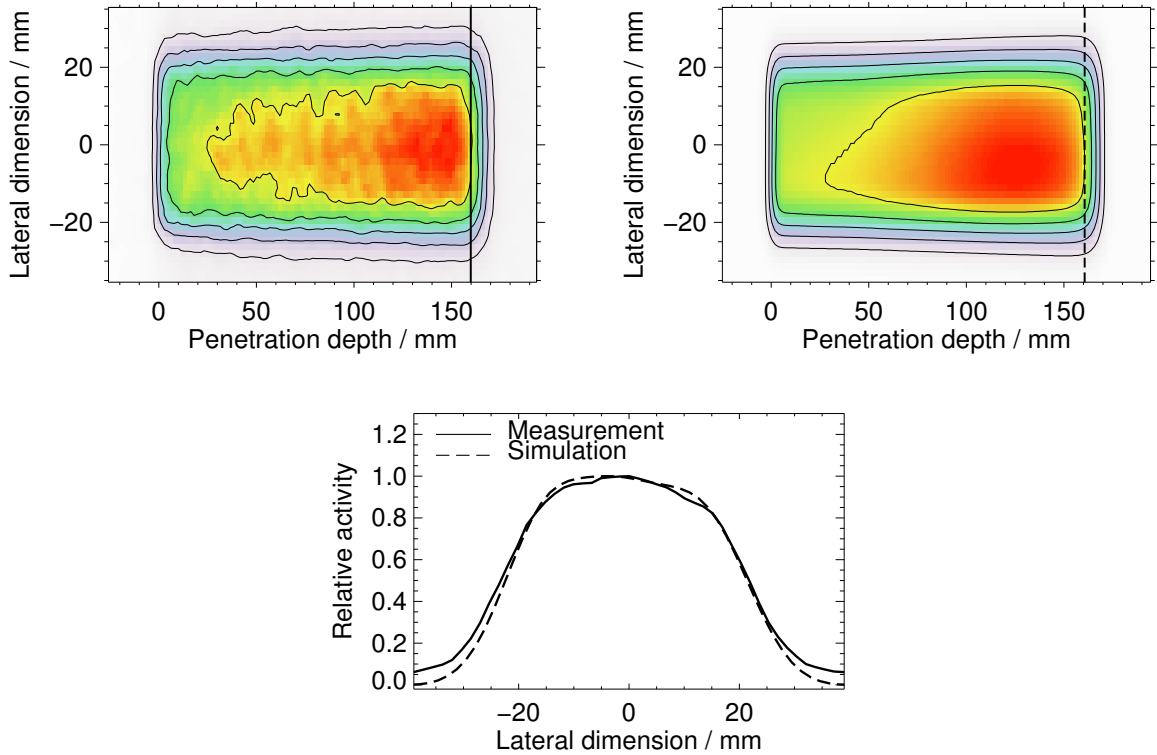
Figure 5–19: *Top: PET image reconstructed from the data exclusively measured during the $\simeq$ 300 s delivery of the mono-energetic scanned field (left) in comparison to the predicted spatial distribution of the amount of detected decays from ^{11}C and ^{15}O (right). Bottom: Lateral profile of the measured (solid) and predicted (dashed) β^+-distribution along the corresponding region marked in the upper figures.*

distribution visible in figure 5–18 (top, right). Therefore, the following analysis will be concentrated on the mono-energetic case, less affected by the suboptimal beam delivery (figure 5–18, left). In addition to the problem of the position inaccuracy, the scanning speed was much lower than in the conventional carbon ion case. About 30 s were necessary for the completion of the very distal 11 scan positions to be filled by $1 \cdot 10^8$ protons each at every repaint in both of the mono-energetic and SOBP case. Despite the same amount of produced positron emitters, the longer time interval introduces larger differences in the number of detectable decays, especially from short-lived isotopes formed in the first and last scan positions, respectively. The effect of this time dependence on the measured β^+-activity becomes observable for acquisitions stopped shortly after the beam delivery. This is illustrated by the reconstruction of a subset of data measured during the mono-energetic irradiation, ruling out the decays after the irradiation end (figure 5–19). The measured lateral profile shown in figure 5–19, bottom, indicates a slightly higher activity signal for the first irradiated scan positions, corresponding to negative values starting from -20 mm. The same trend was rather well reproduced also by the prediction taking into account the registered time course of the irradiation as well as the reduced time window of the PET acquisition. However, the observed slight lateral asymmetry pertains only to the intensity of the β^+-activity, while not affecting the fall-off position of the positron radioactivity distal edge related to the maximum proton range.

The depth profile of the β^+-activity induced by the scanned mono-energetic irradiation along the central beam axis is compared to that produced by a non-scanned pencil-like beam at the same initial energy in figure 5–20. Larger discrepancies between the one-dimensional and two-dimensional field occur only in the
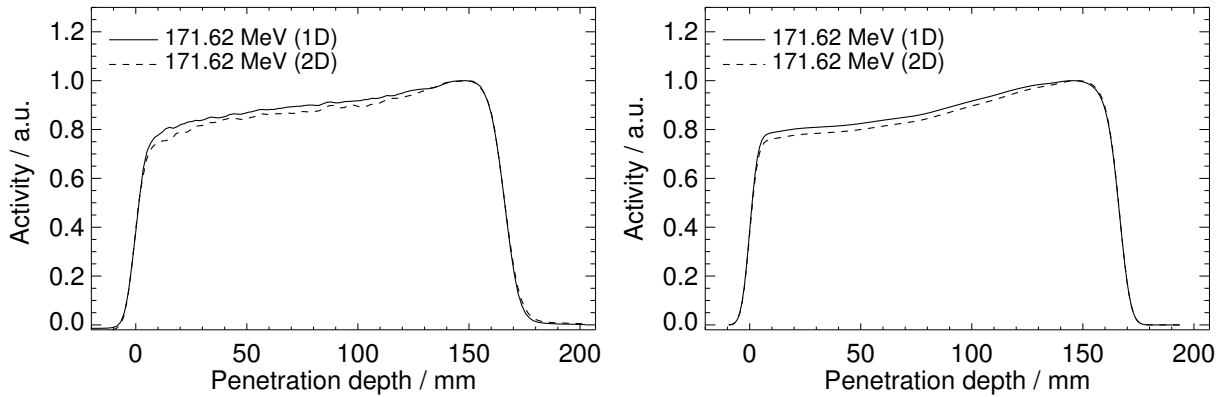
Figure 5–20: *Measured (left) and predicted (right) β^+-activity depth profiles along the central beam axis for a 1D and 2D mono-energetic proton irradiation of a PMMA target at initial energy of 171.62 MeV.*

proximal slope of the depth distributions along the central beam axis. In fact, for one-dimensional fields the cross section increase along the penetration depth is somehow compensated by the reduction of particles along the central beam axis due to lateral scattering. In the inner part of scanned fields particles scattered away from the central beam axis are replaced by contributions coming from the adjacent pencil-like beams. This compensation results in a slightly steeper increase of the β^+-activity distribution along the penetration depth, as shown in figure 5–20. Apart from the rather good correspondence between measurement and prediction, it should be pointed out that the distal edges of the β^+-activity depth profiles induced by the one- and two-dimensional irradiation fields are almost identical (figure 5–20). Therefore, all the range considerations addressed in the next section for one-dimensional mono-energetic and SOBP irradiation can be also extended to the case of multi-dimensional scanned fields.

The resolving power of PET for proton range monitoring in homogeneous phantoms

The achievable accuracy of PET for proton range monitoring has been investigated by means of non-scanned (1D) mono-energetic as well as SOBP exposures of PMMA phantoms at energy steps resulting in range differences of about 0.9 mm. This corresponds approximately to 1 mm separation in water, which is the finest grid used at GSI for depth adjustment of the Bragg-peak position within the tumour in carbon ion therapy. The range information has to be extracted from the distal edge of the proton induced positron radioactivity. Hence, the data analysis has been particularly focussed on the position of the 50 % level of the distal fall-off (addressed in the following as $d_{50\%}$) and the study of the first derivative (in space) of the β^+-activity depth profiles. For data with a sufficient signal to noise ratio, the latter approach provides a precise information on the localisation of the β^+-activity distal edge. This is particular evident for the steeper fall-off induced by mono-energetic irradiation, as illustrated in figure 5–21. Furthermore, the independence of the results on the reconstruction algorithms has been also carefully proven, as briefly addressed in the following section.

i) The mono-energetic case

The β^+-activity depth profiles obtained after backprojection as well as MLEM tomographic reconstruction of the PET events measured in the first of the two sets of mono-energetic irradiation listed in table 5–7 are shown in figure 5–22. In comparison to the simpler backprojection approach the iterative reconstruction produces, as expected, β^+-activity distributions of steeper rising and falling edges. The inclusion of scatter corrections mostly lowers the activity level in the entrance channel. However, the distal fall-offs of the distributions are clearly resolved independently on the used reconstruction algorithm and in spite of
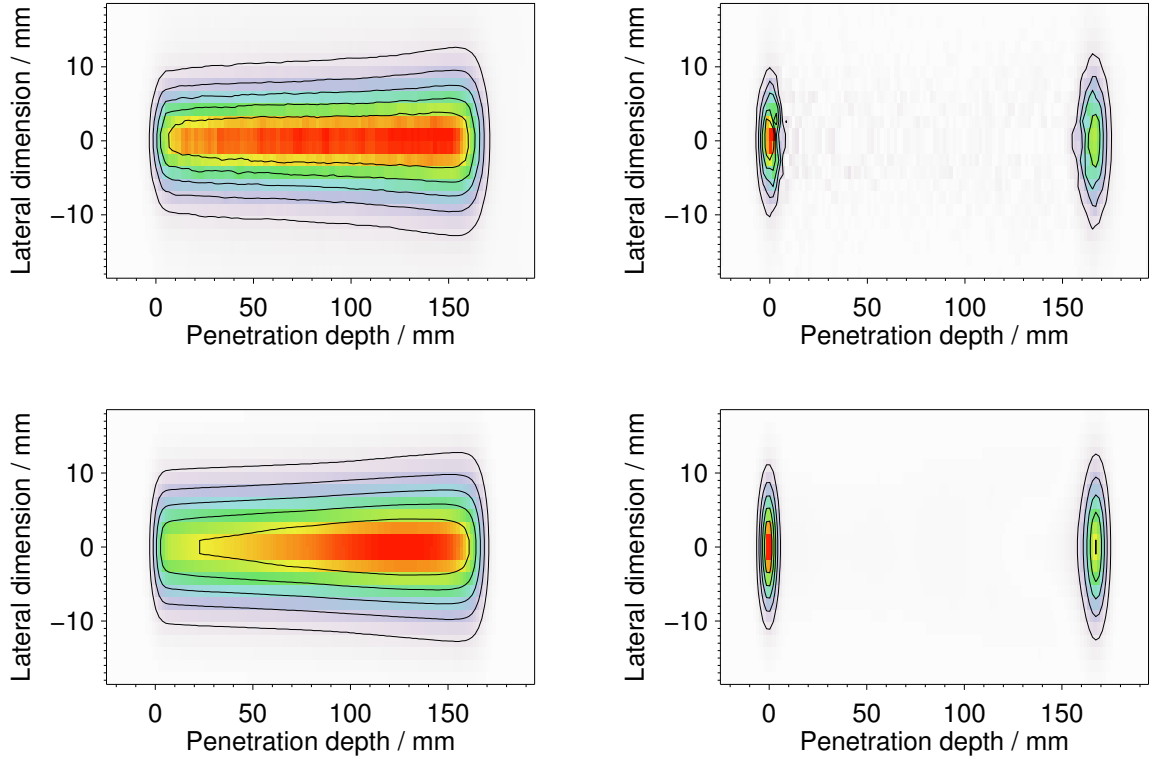
Figure 5–21: *Measured (top) and predicted (bottom) PET images (left) and corresponding absolute values of the first derivative (right) of the spatial distributions induced by a pencil-like beam of 171.62 MeV initial energy stopped in PMMA.*

the moderate spatial resolution of the in-beam positron camera installed at GSI. Hence, only backprojected profiles will be considered in the following. The distinction of adjacent contributions becomes particularly evident when plotting the derivative of the depth distributions, found in good agreement with the expectations (figure 5–23). The average separation between contiguous positions of the 50 % distal fall-offs as well as of the peaks of the derivatives was found to be (0.9 ± 0.3) mm for both lower and higher energy data sets listed in table 5–7. This value is in good agreement with the expected range differences of 0.9 mm (cf. table 5–7). Hence, this phantom experiment demonstrates the potential of PET for millimetre range monitoring. In

Table 5–7: *Parameters of the beam delivery and PET acquisition for the 1D mono-energetic irradiation. For explanation of the symbols cf. table 5–3.*

E / MeV	R / cm	$\mathcal{T}$	I_s / $p\,\mathrm{spill}^{-1}$	t_s / s	t_{ir} / s	t_{mea} / s	N_{ev}
171.62	17.35	120	$(1.9 \pm 0.2) \cdot 10^8$	1.095 ± 0.018	548.43 ± 0.01	1949	5731951
172.13	17.44	120	$(2.2 \pm 0.2) \cdot 10^8$	1.140 ± 0.023	548.37 ± 0.01	1813	5975083
172.63	17.53	120	$(2.1 \pm 0.2) \cdot 10^8$	1.124 ± 0.019	548.42 ± 0.01	1824	5785082
173.13	17.62	118	$(2.6 \pm 0.2) \cdot 10^8$	1.170 ± 0.019	548.96 ± 0.01	1744	7061593
156.06	14.69	120	$(9.4 \pm 0.1) \cdot 10^7$	1.13 ± 0.03	531.42 ± 0.01	1870	2330723
156.60	14.78	120	$(1.0 \pm 0.1) \cdot 10^8$	1.13 ± 0.04	531.37 ± 0.01	1833	2517791
157.13	14.87	120	$(8.3 \pm 0.1) \cdot 10^7$	1.09 ± 0.04	531.16 ± 0.01	1887	2138937
157.66	14.96	120	$(1.0 \pm 0.1) \cdot 10^8$	1.129 ± 0.025	531.28 ± 0.01	1874	2610920
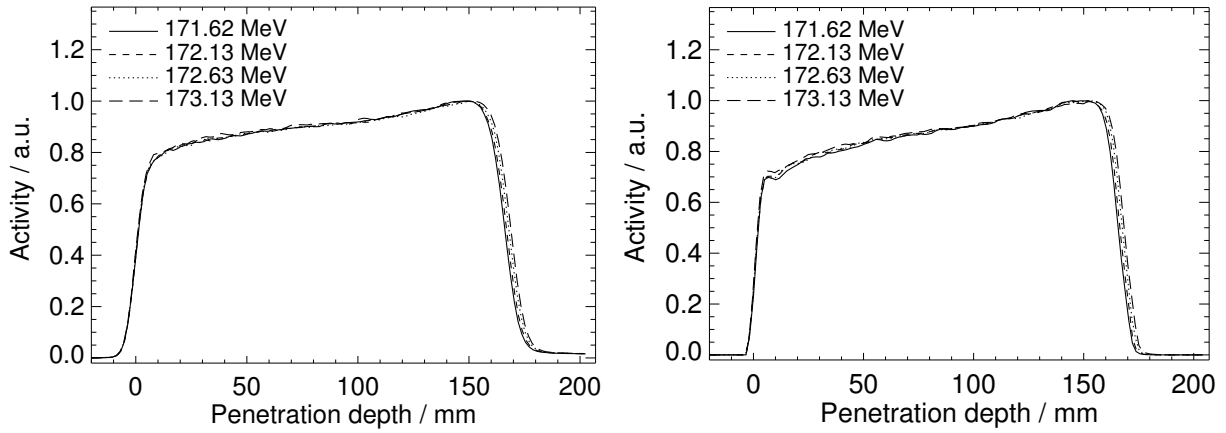
Figure 5–22: *Depth profiles of β^+-activity obtained after backprojection (left) and MLEM reconstruction with scatter corrections (right) for proton beams stopped in PMMA at ranges differing less than $1\,mm$.*

the following, the important factors influencing the achievement of such potential in real clinical situations will be addressed. These include the influence of the counting statistics as well as the consideration of more realistic non-mono-energetic irradiation fields and the impact of different target fragments in dependence on the time course of the irradiation and PET acquisition in combination with the elemental composition (stoichiometry) of the irradiated target.

The sensitivity of the PET method to the counting statistics for proton range monitoring was studied by analysing several subsets of the list mode data acquired for the $171.62 - 173.13\,$MeV irradiation given in table 5–7. The degradation of the statistical significance of the range resolvability for data sets corresponding to a reduced amount of detected events is illustrated by the depth profiles of figure 5–24, corresponding to the data acquired during the delivery of the first 5 and 50 spills of the irradiation, respectively. In the data analysis, very noisy and highly fluctuating profiles resulting from the low statistics of the measured PET events (cf. figure 5–24, left) were internally smoothed with a box car average for the search of the activity distal maximum necessary for the $d_{50\%}$ determination. Despite such a dedicated procedure, the significance of the estimate is unavoidably influenced by the signal to noise ratio of the considered data sets.
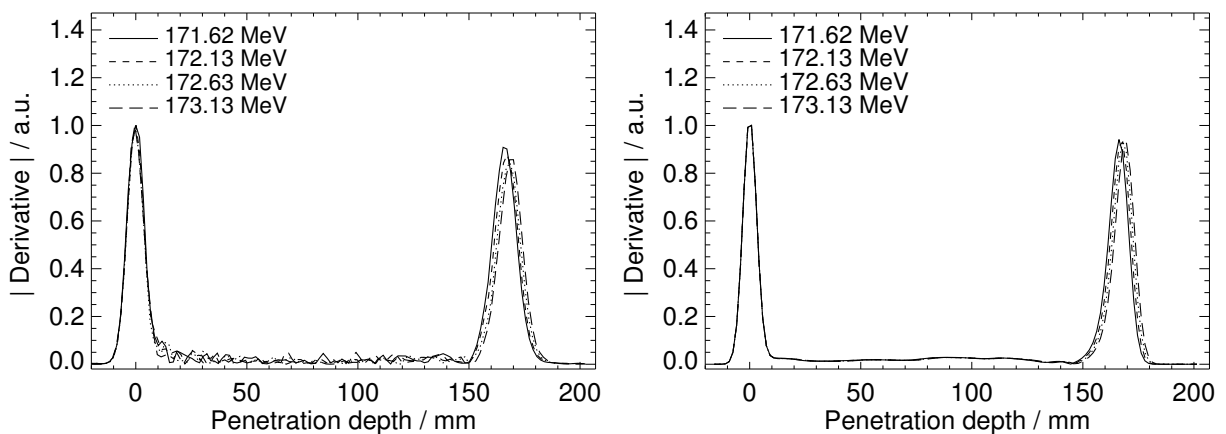
Figure 5–23: *Absolute value of the derivatives of the measured (left) and predicted (right) β^+-activity depth profiles induced by the four mono-energetic proton beams at $171.62 - 173.13$ MeV initial energy.*
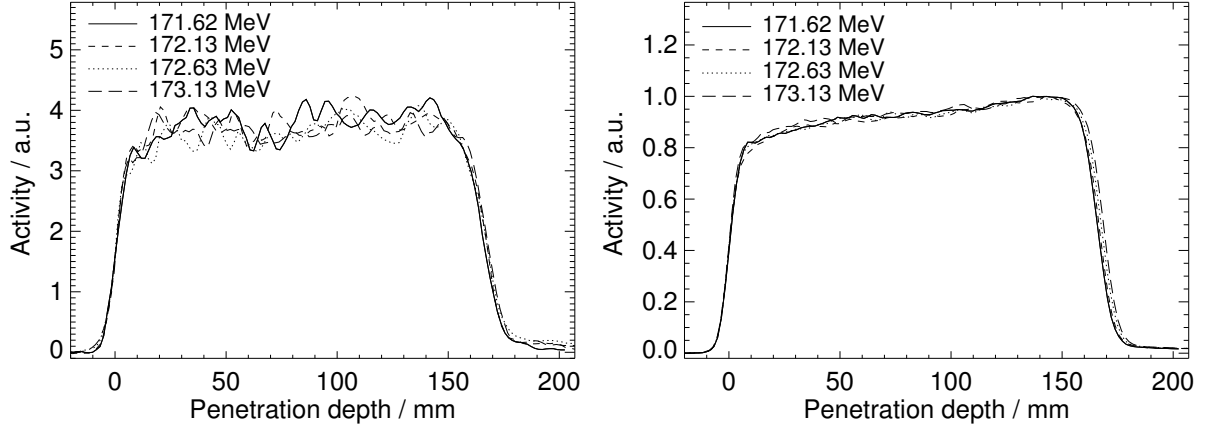
Figure 5–24: *Comparison of β^+-activity depth profiles backprojected from PET events measured during the beam pauses between the first 5 (left) and 50 (right) spills for the $171.62 - 173.13$ MeV proton irradiation.*

This is indicated in table 5–8 by the higher uncertainties of the $d_{50\%}$ values for those profiles reconstructed from the few events measured during only about $18\,\mathrm{s}$ total pause duration between the first 5 beam pulses. Increasing the statistics considerably improves the accuracy of the $50\,\%$ fall-off position identification, with uncertainties falling well below the average separation of the distal profiles corresponding to adjacent energy

Table 5–8: *Position of the $50\,\%$ distal fall-off $d_{50\%}$ of the β^+-activity profiles reconstructed from different subsets of the data recorded during the delivery of the first 5, 50 and 120 (118) spills as well as over the entire PET acquisition for the $171.62 - 173.13$ MeV proton irradiation. Increasing numbers of delivered spills correspond to the estimated maximum Bragg-peak dose values D_{pk} additionally given.*

E / MeV	$\mathcal{T}$	D_{pk} / Gy	t_{mea} / s	N_{ev}	$d_{50\%}$ / mm
171.62	5	1.4	23.02 ± 0.01	17539	164.8 ± 0.9
	50	14	229.97 ± 0.01	579708	165.7 ± 0.3
	120	33	548.43 ± 0.01	2139829	166.0 ± 0.2
	120	33	1949.07 ± 0.01	5731951	166.0 ± 0.2
172.13	5	1.6	22.93 ± 0.01	14365	165.8 ± 0.9
	50	16	229.93 ± 0.01	628654	166.5 ± 0.3
	120	38	548.37 ± 0.01	2308781	166.8 ± 0.2
	120	38	1812.63 ± 0.01	5975083	166.8 ± 0.2
172.63	5	1.5	23.01 ± 0.01	13088	166.2 ± 0.9
	50	15	229.84 ± 0.01	585329	167.5 ± 0.3
	120	36	548.42 ± 0.01	2215589	167.8 ± 0.2
	120	36	1823.66 ± 0.01	5785082	167.9 ± 0.2
173.13	5	1.8	23.00 ± 0.01	16161	167.4 ± 0.9
	50	18	230.15 ± 0.01	713097	168.5 ± 0.3
	118	43	548.96 ± 0.01	2718882	168.7 ± 0.2
	118	43	1743.85 ± 0.01	7061593	168.8 ± 0.2

steps. Referring to table 5–8 it should be noticed that the chosen larger subsets of data correspond to increasing levels of the applied dose. However, the delivered dose is not the only factor influencing the PET counting statistics. The measuring time is in fact the other critical parameter determining the amount of detectable decays from the positron emitters created at a given dose. On the basis of the production rate estimates *relative* to the limited angle positron camera in use at GSI for a similar 175 MeV PMMA irradiation (cf. table 5–5), the amount of events $N_{\rm ev}$ detected in a typical acquisition time of 5 minutes at a typical therapeutic dose of 3 Gy is estimated to be about $(3.5 - 4.0) \cdot 10^5$ coincidences. Hence, the comparison with the values reported in table 5–8 for the data sets corresponding to the delivery of the first 50 spills suggests a relatively low uncertainty of the corresponding $d_{50\%}$ estimation. Moreover, the estimated counting statistics could be further improved in future application of PET to proton therapy monitoring. An increase is expected for a new generation in-beam PET scanner of higher detection efficiency due to a larger solid angle coverage as well as an optimal data acquisition (cf. conclusions of chapter 4). In addition, different fractionation schemes might lead to a higher applied dose per treatment fraction. Finally, a further activity increase in typical $5 - 10$ minutes acquisition times is also foreseen due to the typically larger production of ^{15}O in real tissue with respect to PMMA. Therefore, all these considerations on the counting statistics still support the potential millimetre precision of PET for proton range monitoring in more realistic clinical applications.

From the data reported in table 5–8 for different subsets of the same PET acquisition at a given beam energy it should be finally pointed out the variation of the $d_{50\%}$ value itself beyond the discussed variation of the error due to the different counting statistics. The observed systematic changes of the distal fall-off positions for depth profiles reconstructed from different subsets of the same irradiation are ascribed to the dynamic process of the β^+-activity build-up and decay during acquisition. This mostly results in different ratios of ^{11}C to ^{15}O decays (cf. figure 5–6, left) in the subsets of events measured in the different time windows of the same list mode data. The consequence of this effect on the possibility of range monitoring will be more deeply addressed in the dedicated section following the presentation of the results for the more realistic case of SOBP irradiation.

ii) The SOBP case

Four extended dose distributions of maximum range differing less than 1 mm in PMMA were formed by a sequence of 11 mono-energetic pencil-like beams with increasing energies in the intervals of $156.06 - 171.62$ MeV, $156.60 - 172.13$ MeV, $157.13 - 172.63$ MeV and $157.66 - 173.13$ MeV, respectively (table 5–9). The chosen spacing of the 11 contiguous energy steps corresponded to 3 mm range separation in water. The SOBP sequences were repeated 10 times. Despite the discussed smoother fall-off of the β^+-activity depth distributions in the SOBP case, the distal edges of the profiles could be still resolved (figure 5–25). This supports the feasibility of range monitoring by means of PET also in more realistic extended treatment fields, provided that enough statistical significance is gained. For the last issue PET distributions formed after the

Table 5–9: *Parameters of the irradiation and of the PET measurement for the 1D SOBP experiments. For explanation of the symbols cf. table 5–6.*

| $E_{\rm min} - E_{\rm max}$ / MeV	R / cm	$\mathcal{P} \times \mathcal{E}$	N_p	$t_{\rm ir}$ / s	$t_{\rm mea}$ / s	$N_{\rm ev}$
$156.06 - 171.62$	17.35	10×11	$1.4 \cdot 10^{10}$	793.17 ± 0.01	1726	3201783
$156.60 - 172.13$	17.44	10×11	$1.4 \cdot 10^{10}$	757.40 ± 0.01	1713	3207279
$157.13 - 172.63$	17.53	10×11	$1.4 \cdot 10^{10}$	712.74 ± 0.01	1714	3226331
$157.66 - 173.13$	17.62	10×11	$1.4 \cdot 10^{10}$	765.86 ± 0.01	1668	3198891
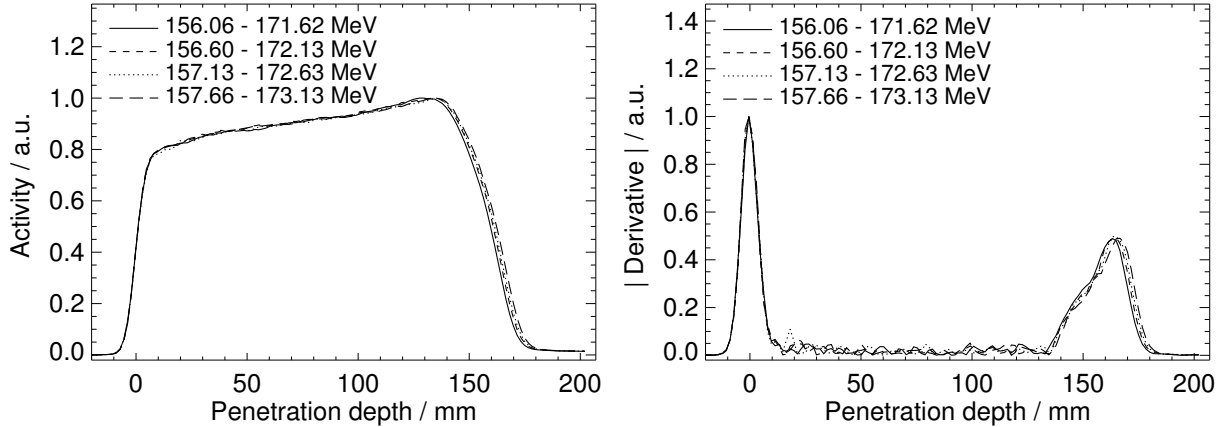
Figure 5–25: *Depth distributions of β^+-activity (left) and corresponding absolute derivative (right) for 1D SOBP irradiation of PMMA targets at maximum penetration depths differing less than 1 mm.*

delivery of complete SOBP fields at different dose levels and different amounts of measured events could be compared because of the selected repainting technique. The depth profiles backprojected from approximately $1.2 \cdot 10^5$ coincidence events detected during the first $\simeq 150\,\mathrm{s}$ of the irradiation corresponding to the delivery of 2 repaints (i.e. maximum dose of about $2.2\,\mathrm{Gy}$) are shown in figure 5–26. For this data set of lower statistics an average distal edge separation of $(1.0 \pm 0.8)\,\mathrm{mm}$ was found against the $(0.9 \pm 0.4)\,\mathrm{mm}$ value for the profiles obtained from the entire acquisition. This confirms the increasing accuracy and reliability of PET for millimetre range monitoring when increasing the image counting statistics, as already discussed in the mono-energetic case. The comparison of the average distal edge separation of $(0.9 \pm 0.4)\,\mathrm{mm}$ with the value of $(0.9 \pm 0.3)\,\mathrm{mm}$ obtained in the mono-energetic case (cf. previous section) for data sets of comparable high statistics indicates only a minor degradation in the accuracy of the $50\,\%$ fall-off position identification for SOBP fields. Hence, all statistics considerations reported in the previous section can be extended to the more realistic case of non-mono-energetic irradiation fields. The slightly higher uncertainty of the $50\,\%$ fall-off position for SOBP fields arises from the smoother distal slope of the β^+-activity depth profile, resulting also in a backwards shift of about $6.5\,\mathrm{mm}$ for the $d_{50\%}$ value in the considered experiment with respect to the mono-energetic case (figure 5–27, left). Moreover, the $d_{50\%}$ value itself and its related error is influenced by the width of the SOBP, which affects the smoothness of the distal fall-off of the β^+-activity distribution.
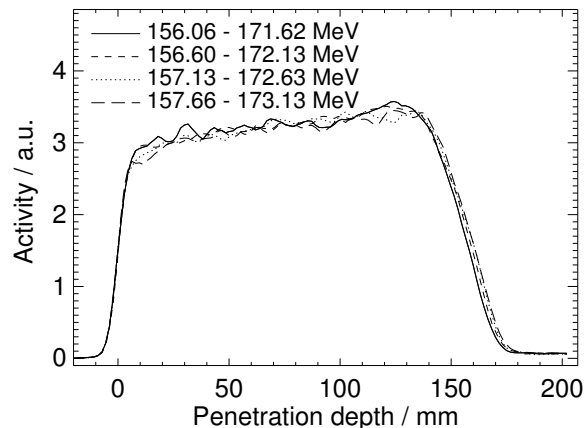

Figure 5–26: *Depth distributions of β^+-activity reconstructed from the subset of data measured during the delivery of the first 2 repaints of the 4 SOBP irradiation at maximum ranges differing less than 1 mm.*
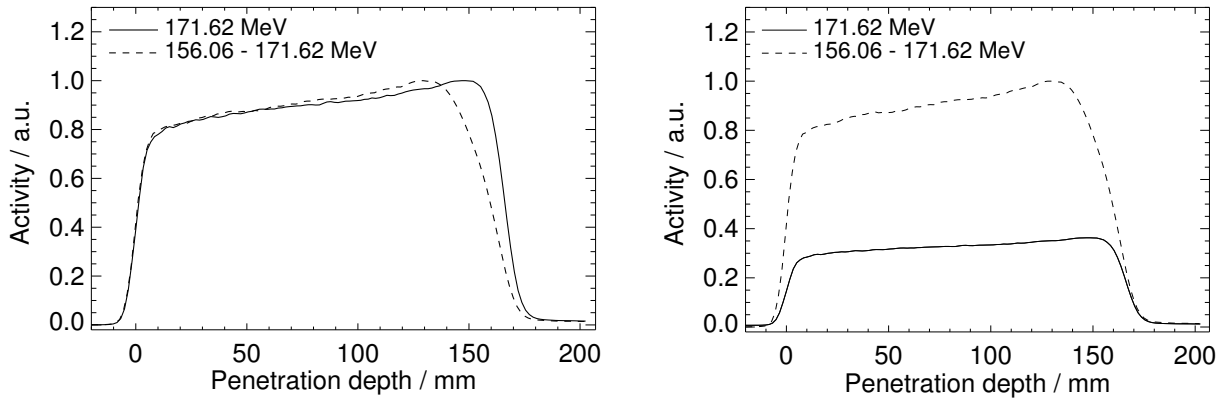
Figure 5–27: *Depth distribution of β^+-activity measured for the $156.06 - 171.62\,MeV$ SOBP irradiation (dashed line) in comparison to that acquired for the pencil-like beam contribution of highest energy (solid line). The two profiles were normalised either to the same maximum (left) or to the $\simeq 35\,\%$ ratio between the amount of highest energy protons with respect to the total projectiles building the SOBP (right).*

Hence, the $d_{50\%}$ quantity is a worse estimator for extracting information on the maximum proton range in the case of extended treatment fields. The very distal slope of the distribution is a more reliable quantity for this purpose. This is shown in figure 5–27 (right) for the comparison of the measured SOBP profile with the one induced by the most energetic beam, properly normalised to its relative contribution to the extended irradiation field. An even more effective representation is provided by the derivative (figure 5–28), clearly exhibiting in the distal peak a superposition of several Gaussian shapes of increasing amplitudes at increasing depths (i.e. energies) corresponding to the contributions of the mono-energetic beams forming the SOBP field. It follows that the very distal slope of the total β^+-activity (figure 5–27, right) and corresponding derivative (figure 5–28) depth distribution is determined by the highest energy component and can be resolved for data of sufficient statistics. This is in agreement with the expectations discussed in [Par02]. Since a reasonable energy step spacing was used for the build-up of the SOBP irradiation imaged in this experiment, similar considerations are expected to apply also to more realistic extended treatment fields. Hence, these results support the feasible extraction of information on the maximum proton range from the very distal edge of the total β^+-activity distribution by means of PET.
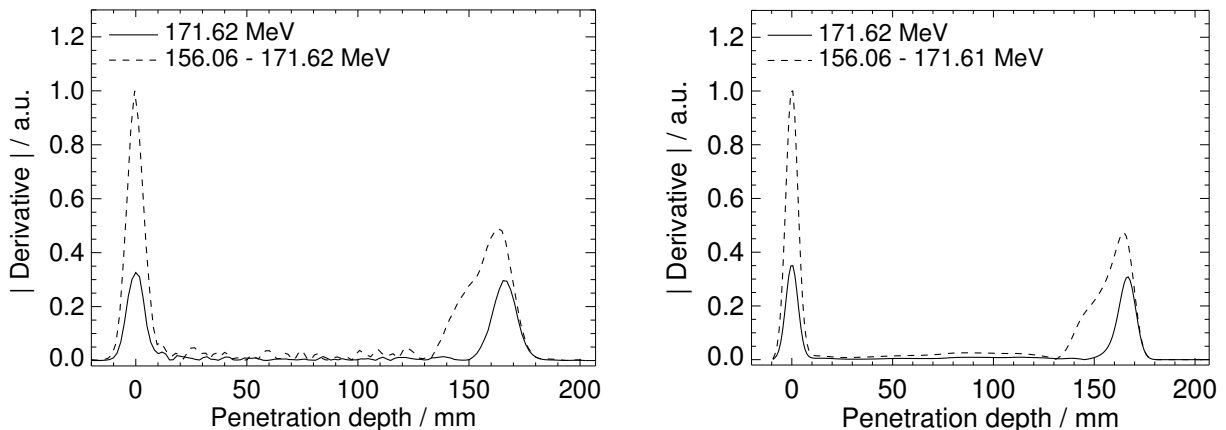
Figure 5–28: *Measured (left) and predicted (right) absolute derivative of the β^+-activity depth profiles induced by a SOBP irradiation (dashed line) in comparison to the highest energy contribution (solid line).*

The influence of the ^{11}C to ^{15}O production and decay ratio on the feasibility of proton range monitoring

The study of dynamic effects due to different ratios of detected events mainly originating from ^{11}C and ^{15}O decays has been restricted to mono-energetic irradiation without beam scanning, which allows the use of the mathematical formalismus described in section 5.3.2.2. The data presented in table 5–8 already pointed out an increase of the 50 % fall-off position for β^+-activity profiles reconstructed from larger subsets of the same PET acquisition corresponding to longer measuring time intervals. Following equations (25) and (26) increasing values of 0.28, 0.38, 0.55 and 1.7 were assigned to the mean ^{11}C to ^{15}O decay ratio for all the considered data sets measured during the delivery of the first 5, 50 and 120 (118) spills as well as over the entire PET acquisition, respectively. This analysis might be however affected by statistics effects due to the increasing number of coincidences in the chosen acquisition windows. In order to rule out the dependence on the counting statistics, several subsets of the same acquisition were selected, each corresponding to the same amount of detected events but different ^{11}C to ^{15}O decay ratios. However, a wide range of ^{11}C to ^{15}O decay ratios could be accessed only when considering subsets of low ($\simeq 1.6 \cdot 10^4$) statistics. In fact, small ^{11}C/^{15}O decay ratios are possible only for few events registered at the beginning of the irradiation. Since the statistics determines the accuracy of the fall-off position identification (cf. table 5–8), additional subsets of higher statistics were also included in the study in order to increase its significance. The results confirmed an influence of the ^{11}C to ^{15}O decay ratio on the β^+-activity distal edge independently on the used reconstruction algorithm. An example is shown in figure 5–29 for the analysis of the PET acquisition induced by the 173.13 MeV irradiation given in table 5–8. The statistics of the considered subsets of the same list mode data acquisition is reflected by the error bars of the $d_{50\%}$ values (triangles) extracted from the backprojected β^+-activity depth profiles. The position of the 50 % distal fall-off is found to be systematically reduced for low ^{11}C/^{15}O decay ratios in spite of the almost 4 MeV lower energy threshold for production (cf. section 5.2.2) as well as the almost 1 MeV higher maximum energy of the emitted positron for ^{15}O with respect to ^{11}C. The effect can be explained by the higher energy of the cross section maximum for the
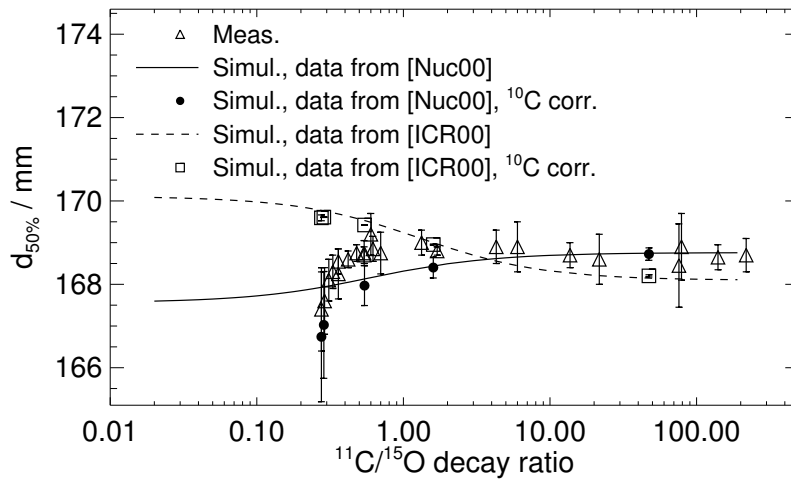
Figure 5–29: *Position of the 50 % distal fall-off of the β^+-activity depth profiles reconstructed from several subsets of the same PET acquisition corresponding to different ^{11}C/^{15}O decay ratios (triangles) in comparison to expectations based on calculations using experimental cross sections from [Nuc00] (solid) and [ICR00] (dashed) for a 173.13 MeV proton irradiation of a PMMA target. Filled circles and open squares refer to the same calculations corrected for the ^{10}C contribution (cf. text).*
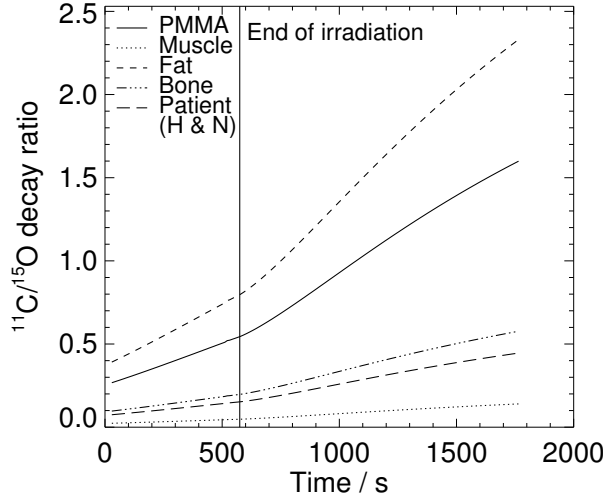
Figure 5–30: *Solid: Estimation of the time-integrated $^{11}C/^{15}O$ decay ratio for the events measured by the positron camera over the entire acquisition time for the 173.13 MeV proton irradiation of a thick PMMA phantom. Dotted, dashed, dotted-dashed lines: Extension to other materials of therapeutic interest and to a typical head and neck (H&N) patient obtained from the normalisation of the estimated isotope production rates in PMMA to the different carbon to oxygen nuclei abundance taking into account only the (p, pn) reaction channels.*

$^{16}O(p, pn)^{15}O$ in comparison to the $^{12}C(p, pn)^{11}C$ reaction channel, in consistency with the experimental data from [Nuc00] used for the calculation (figure 5–8). A similar trend is in fact also reproduced by the fall-off of the profiles obtained from the superposition of the predicted ^{11}C and ^{15}O depth distributions (figure 5–11, left) properly normalised to the given decay ratio. The discrepancy between the measured and predicted data at the lower $^{11}C/^{15}O$ decay ratios can be attributed to the ^{10}C contribution, which is not negligible for short acquisitions at the very beginning of the irradiation (cf. figure 5–6, left). This effect was investigated by including in the prediction the ^{10}C distribution obtained from the FLUKA internal models (cf. figure 5–2) and normalised to the $^{10}C/^{15}O$ decay ratio deduced from the experimental data. The resulting data points (black filled circles) at increasing $^{11}C/^{15}O$ decay ratio depicted in figure 5–29 were estimated to correspond to a decreasing $^{10}C/^{15}O$ decay ratio of 0.71, 0.59, 0.19, 0.14 and 0, respectively. Despite the rather large uncertainties of the fall-off position identification from measured and predicted β^+-activity profiles at small $^{11}C/^{15}O$ decay ratios and correspondingly large $^{10}C/^{15}O$ values, the ^{10}C correction indeed provides a better agreement. On the contrary, the lower penetration depth of ^{15}O target activation indicated by the $d_{50\%}$ reduction at low $^{11}C/^{15}O$ decay ratios in the PET measurements (cf. figure 5–29) would not be explained by the cross section values proposed in [ICR00] (cf. figure 5–11, right). This is illustrated by the calculations reported in figure 5–29 independently whether including (squares) or not (dashed line) the correction for the ^{10}C contribution.

The observed sensitivity of the β^+-activity distal edge to the ^{11}C to ^{15}O decay ratio implies a dependence on the time course of the irradiation and the in-beam PET acquisition. In order to address this issue, the time-integrated $^{11}C/^{15}O$ decay ratio has been estimated for the given time structure of the 173.13 MeV PMMA irradiation, very much resembling that in use for carbon ion treatment at GSI. The result, found to be independent on the beam intensity, is displayed by the solid line in figure 5–30. The corresponding $d_{50\%}$ variations can be extrapolated from figure 5–29. For a rough comparison the time dependence of the $^{11}C/^{15}O$ decay ratios in other materials of therapeutic relevance was approximately estimated by normalising the

isotope production rate in PMMA to the corresponding carbon to oxygen abundance (figure 5–30). Values for fat (adipose tissue), bone (compact) and muscle (striated) were taken from [ICR93]. The average composition of real tissue (patient) was deduced from X-ray CT of head tumour patients irradiated at GSI by means of a segmentation and stoichiometric calibration according to [Schn00] of the Hounsfield numbers located within the treatment field. However, the corresponding $d_{50\%}$ variation for these material cannot be directly extrapolated from that reported in figure 5–29 for PMMA, due to the different stopping properties resulting in different residual ranges at energies below the threshold for positron emitter production. Furthermore, the presented analysis has focussed only on (p, pn) reaction channels on carbon and oxygen, which is a reasonable approximation for PMMA. However, for example in materials more rich in oxygen than carbon (e.g. muscle) the increasing role of the $^{16}O(p, 3p3n)^{11}C$ reaction channel should not be neglected. The resulting higher ^{11}C production would correspond to a steeper $^{11}C/^{15}O$ decay ratio increase during irradiation with respect to the given estimate. Nevertheless, this effect might be compensated by the reduced $d_{50\%}$ separation between ^{11}C and ^{15}O depth profiles which can be expected because of the higher energy of the cross section maximum as well as of the threshold for the $^{16}O(p, 3p3n)^{11}C$ reaction in comparison to the $^{12}C(p, pn)^{11}C$ channel [Alb62]. In addition, it has been already shown in the ^{10}C case that even minor reaction channels may have a time dependent and not negligible impact on the distal edge of the total β^{+}-activity distributions. Hence, all these considerations address once more the need of as much as possible accurate knowledge of the tissue stoichiometry in combination with detailed and experimentally validated description of cross sections for all the reaction channels leading to positron emitter production.

Millimetre accuracy for on-line range monitoring might still be achieved at least in regions of interest when properly selecting the time structure of the irradiation as well as the PET acquisition window. The criterion would be to minimise $d_{50\%}$ variations in dependence on the estimated unavoidable sources of uncertainties, maintaining at the same time a reasonable counting statistics. For beam delivery systems with dynamic energy variation (e.g. from the accelerator or dynamic range shifters) the increasing or decreasing order of the energy steps should be also concerned. In particular, a sequence of decreasing energies would maximise the $^{11}C/^{15}O$ decay ratio at the most critical distal edge, hence minimising the $d_{50\%}$ uncertainties. However, the benefit of such selection in real clinical cases should be carefully investigated taking into account also the effect of a longer time interval on perfusion and washout processes after the β^{+}-activity formation at the distal edge. Obviously, the $^{11}C/^{15}O$ problem does not affect off-line imaging starting few minutes after the irradiation end. This is however at the expense of a loss of counting statistics, affecting the accuracy of the 50 % fall-off position identification at comparable acquisition times. A further drawback of off-line techniques is the higher sensitivity to blurring effects due to biological pathways washing out the produced isotopes and to possible movement of the patient with respect to the treatment position. Finally, off-line detection precludes the possibility to differentiate tissues of similar density but different stoichiometric composition, as addressed in the next section.

Mono-energetic proton irradiation of an inhomogeneous target

A one-dimensional (non-scanned) mono-energetic irradiation of an inhomogeneous phantom has been performed in order to investigate the sensitivity of the proton induced positron radioactivity to different tissue density values and stoichiometry. This determines the feasibility of PET for proton range monitoring in tissue heterogeneities as well as for detection of possible field misalignments or local anatomical modifications during fractionated therapy. A pencil-like beam of 156.06 MeV was extracted over 120 spills for a total irradiation time of (530.49 ± 0.01) s. PET data were acquired over a total 1321 s long acquisition time. The material penetrated by the beam (cf. figure 5–31) is summarised in table 5–10. The corresponding composition is given in table 5–11. It follows that apart from the lateral lung/PE gradient and the small
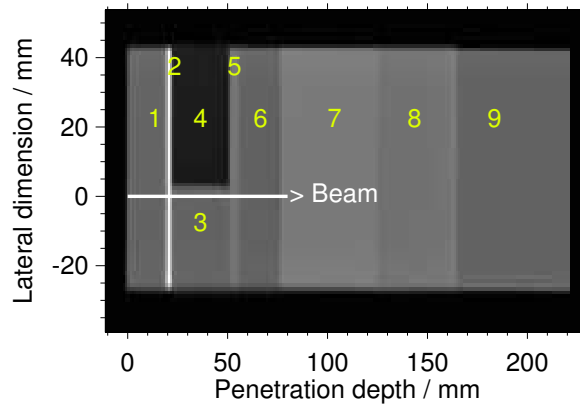
Figure 5–31: *X-ray CT of the inhomogeneous target in the imaged mid plane of the positron camera in the experimental configuration. The enumeration refers to the different inserts described in table 5–10. The arrow shows the beam position and direction.*

Table 5–10: *Constituents of the irradiated inhomogeneous phantom. The numbers 3 and 4 correspond to a lateral gradient in the plane parallel to the two positron camera heads, with $[-28, 2]$ mm PE and $[2, 42]$ mm lung equivalent with respect to the beam axis (cf. figure 5–31).*

Number	Material	Thickness / mm
1	Polyethylene (PE)	20
2	Bone equivalent	2
3	Polyethylene (PE)	29
4	Lung equivalent	29
5	Muscle equivalent	5
6	Polyethylene (PE)	20
7	Polymethyl methacrylate (PMMA)	50
8	Muscle equivalent	40
9	Polyethylene (PE)	55

Table 5–11: *Composition (fraction by weight) and density of the materials assembled in the inhomogeneous phantom [ICR93, Has96, Hinz03]. Some uncertainties in the stoichiometry of the tissue equivalent materials have to be taken into account because of a lack of an unequivocal source of information.*

| Medium	H / %	C / %	N / %	O / %	Mg / %	Si / %	Cl / %	Ca / %	ρ / $\mathrm{g\,cm^{-3}}$
PE	14.37	85.63	–	–	–	–	–	–	0.93
PMMA	8.05	59.99	–	31.96	–	–	–	–	1.18
Bone eq.	3.10	31.26	0.99	37.57	–	–	0.05	27.03	1.89
Muscle eq.	8.41	67.97	2.27	18.87	–	–	0.13	2.35	1.00
Lung eq.	8.36	60.41	1.67	17.33	11.36	0.72	0.15	–	0.30
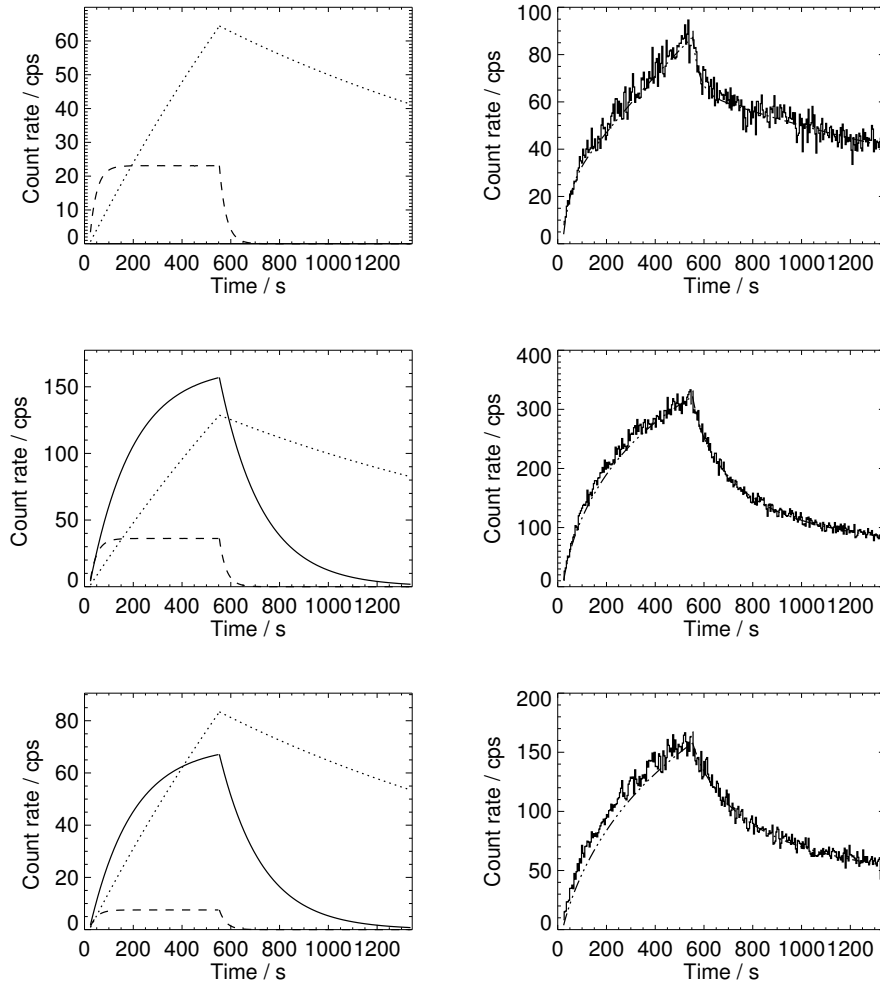
Figure 5–32: *Estimated count rate (cps) contribution from ^{15}O (left, solid), ^{11}C (left, dotted) and ^{10}C (left, dashed) and resulting total decay rate (right, dashed-dotted) compared to the measured count rate (right, solid) from proton induced activation in ROI set in PE (top), PMMA (middle) and muscle equivalent (bottom).*

bone equivalent insert, only smooth density gradients but different stoichiometry especially with respect to the C/O composition were encountered by the beam, stopped shortly after the last muscle insert. The CT scan of the phantom shown in figure 5–31 was used for calculation of attenuation corrections for PET imaging [Pön03b]. In order to estimate the ^{11}C, ^{15}O and ^{10}C production rates in the different materials on the basis of the measured data the models described in 5.3.2.2 were applied to subsets of PET events detected in lines of response unambiguously intersecting properly set regions of interest [Hinz00]. Results of this investigation are shown in figure 5–32 for PE (first insert), PMMA and muscle equivalent (last insert). The worse agreement in the last material probably originates from the neglection of contributions from other positron emitters, e.g. ^{13}N. However, due to the low statistics the fitting procedure turned out to be unstable when attempting to include more parameters accounting for other isotopes. Predictions of the positron emitter distributions were based on both of the FLUKA internal models, keeping into account all possible reaction channels, as well as the approach described in section 5.3.2.3, focussed only on (p, pn) interaction on carbon and oxygen nuclei. Due to the lack of information on the stopping properties of the tissue equivalent materials, the necessary density effect parameters and ionisation potentials were derived from [Ste84]. Hence, minor inaccuracies in the position of the predicted activity distal edge can be ascribed to this approximation. The resulting positron emitter distributions are shown in figure 5–33. Despite the lower amount of isotopes predicted by the dedicated approach (cf. section 5.3.2.3), a similar trend with dominant role of ^{11}C
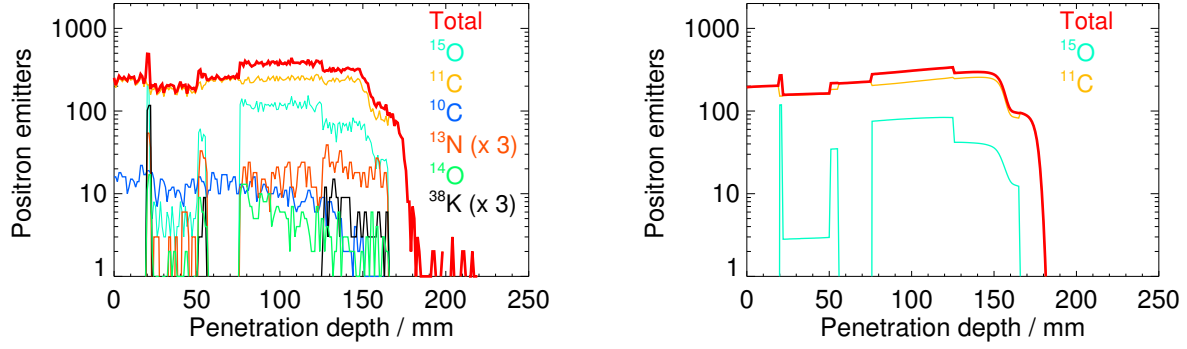
Figure 5–33: *Positron emitter production in the inhomogeneous phantom calculated by means of FLUKA internal models (left) and the approach described in section 5.3.2.3 (right). To reduce statistical fluctuations a median filter over 2 bins (each 1 mm wide) was applied to the internal model predictions for the minor production of isotopes different than ^{15}O and ^{11}C in the left panel.*
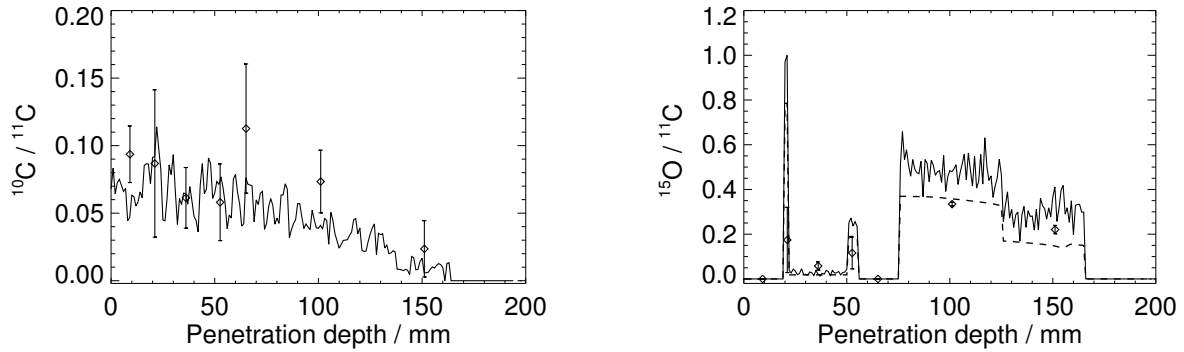

Figure 5–34: *Depth variation of the $^{10}C/^{11}C$ (left) and $^{15}O/^{11}C$ (right) production deduced from the PET data (points) and predicted by the FLUKA internal models (solid) and the dedicated approach (dashed, right).*

and ^{15}O was observed. The predicted $^{15}O/^{11}C$ and $^{10}C/^{11}C$ production values were also compared to the corresponding isotope production ratios deduced from the measured PET data, as shown in figure 5–34. In particular, the predictions from the dedicated approach are found in rather good agreement with the experimental data, except that in the last muscle insert. Since this latter region corresponds to the distal part of the proton penetration, the reason for the disagreement can be an underestimate of the used experimental cross sections for the $^{16}O(p,pn)^{15}O$ reaction at the lower energies close to the energy threshold. This is suggested by the more recent measurements of [Kit90] in comparison to the chosen interpolated cross section values (figure 5–8). Furthermore, the ^{15}O estimation from the time analysis of the measured decay curves can be also overestimated in muscle, due to the neglection of other short-lived components (e.g. ^{14}O, ^{13}N) in the fitting parameters. Nevertheless, considering the uncertainties in the stoichiometric composition of the tissue equivalent mixtures and the unavoidable limitations for identification of pure isotope production rates in different materials from the measured coincidence lines, an overall fairly reasonable agreement was found.

The sensitivity of the proton induced activation to the inhomogeneous target structure has been investigated in relation to the main ^{11}C to ^{15}O decay ratio. For this purpose PET images were reconstructed from subsets of $2.5 \cdot 10^5$, $2.2 \cdot 10^5$ and $2.2 \cdot 10^6$ events registered during the delivery of the first 50 spills, the decay starting 10 minutes after the irradiation end as well as the complete PET acquisition, respectively. This selection corresponds to an estimated ^{11}C to ^{15}O decay ratio in PMMA of 0.4, 27.1 and 1.4, respectively. The 2D PET images are compared in figure 5–35 to the predictions calculated by means of the dedicated
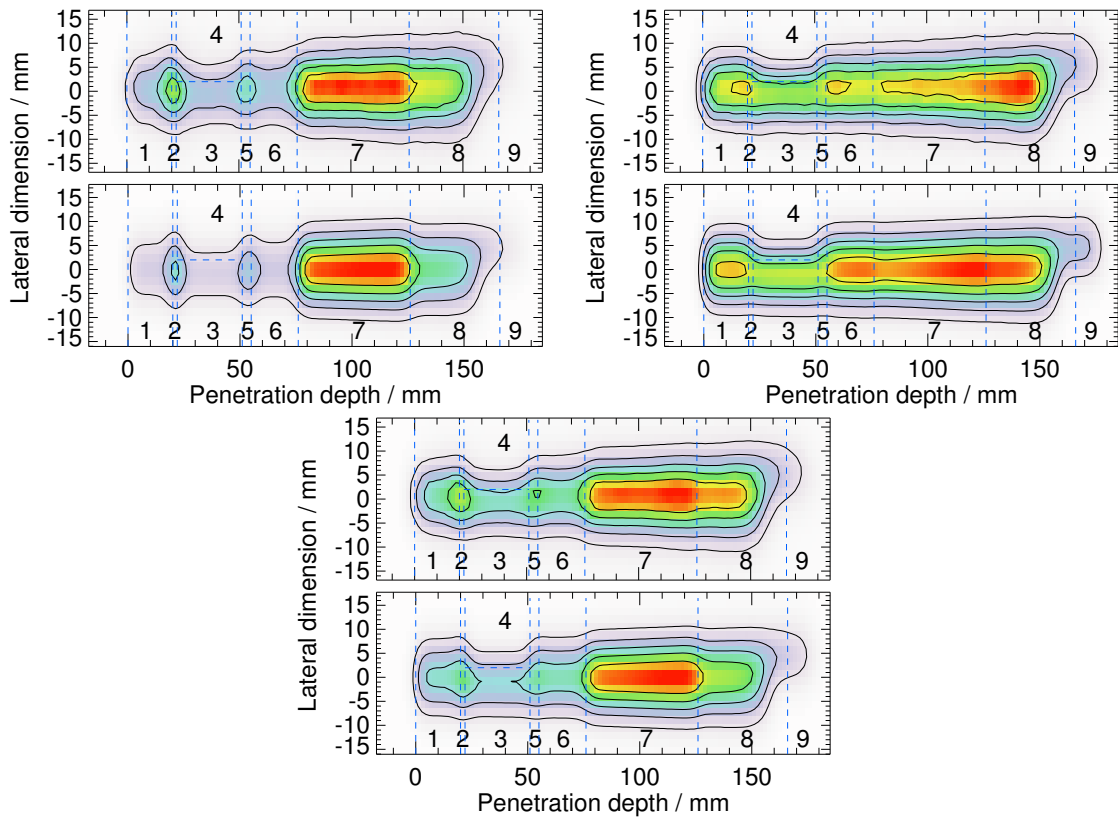
Figure 5–35: *Measured (upper) and predicted (lower) PET images during the delivery of the first 50 spills (top, left), starting 10 minutes after the end of the irradiation (top, right) as well as over the complete measurement (bottom). The dashed blue lines delimit the different materials of the composite phantom.*
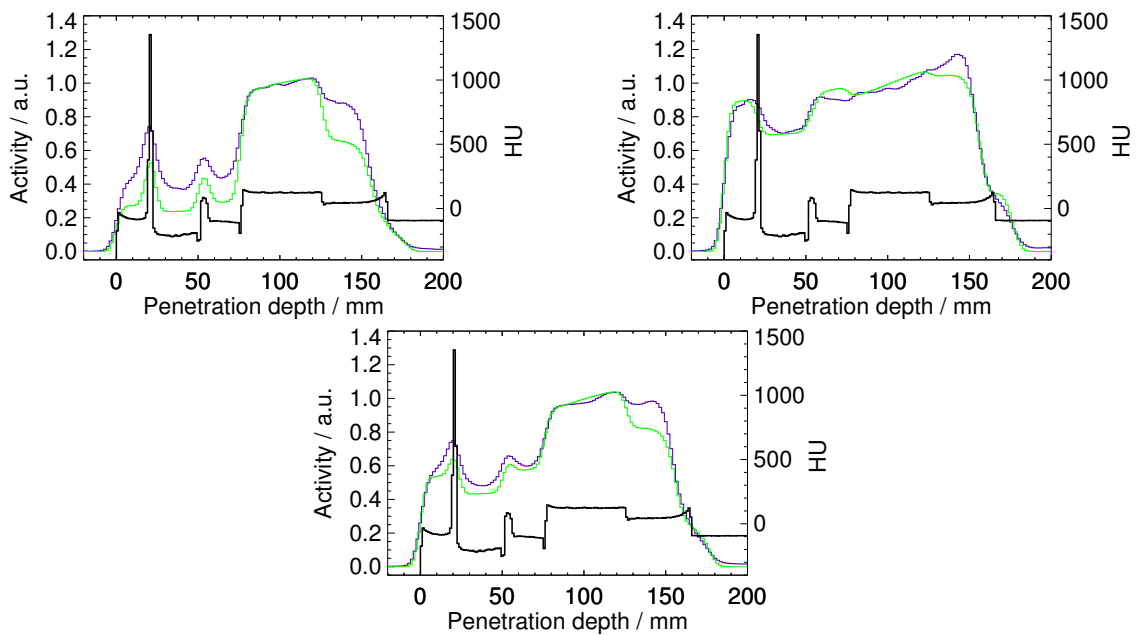

Figure 5–36: *Measured (blue) and predicted (green) β^+-activity depth profiles for the same data-set presented in figure 5–35. The black line, referring to the right axis scale, additionally shows the depth profile of the Hounsfield units from the available CT.*

approach and normalised to the estimated ^{11}C to ^{15}O decay ratio in PMMA. The corresponding depth profiles are shown in figure 5–36. Despite the discussed worse agreement in the last muscle insert as well as the neglection of minor positron emitters (e.g. ^{10}C, ^{13}N, ^{14}O and ^{38}K), mostly affecting the acquisition during the first 50 spills due to the half-lives, a similar trend between measurement and expectation was observed. In particular, the sharp lateral density gradient results in the visible range spike nicely reproduced in both of the measurement and simulation (figure 5–35). Structures of similar density but different C/O concentration can be differentiated only at low ^{11}C to ^{15}O decay ratios, as indicated by the smoother activity variation at the borders between PE, PMMA and muscle on the right side with respect to the left side of figure 5–36, top. This points out once more the sensitivity of the proton induced positron radioactivity to the time structure of the irradiation and of the PET acquisition. With respect to the latter issue, on-line monitoring offers the advantage to detect short-lived isotopes, hence improving the image contrast of different tissues. In addition to the range considerations reported in the previous section, these results strongly suggest the selection of proper time windows in off-line analysis, aiming either to achieve high precision in range monitoring or allow distinction of tissues of similar density but different elemental composition.

5.3.3.3 Proton induced β^+-activity lateral distributions

The lateral distribution of the proton induced positron radioactivity conveys information on the transversal localisation of the beam and of the dose delivery for in-vivo verification of the lateral position of the irradiation field. This issue can be of particular importance for portals passing adjacent to radiosensitive structures. Protons exhibit more pronounced lateral scattering in comparison to heavier ions. Furthermore, the description of the beam lateral broadening has often limited accuracy in conventional treatment planning systems based on analytical models, especially in presence of transversal heterogeneities. Hence, on-line monitoring of the amount of laterally scattered dose to critical organs can be also a crucial issue in real therapeutic irradiation.

The width of the lateral profiles of the β^+-activity induced in PMMA by pencil-like proton beams at initial energy of 110, 140 and 175 MeV is plotted along the penetration depth on the left side of figure 5–37. The sketched FWHM is mostly determined by the lateral dimension of the beam. Further smaller contributions come from the spatial resolution of the imaging system in addition to the slight fluctuations of
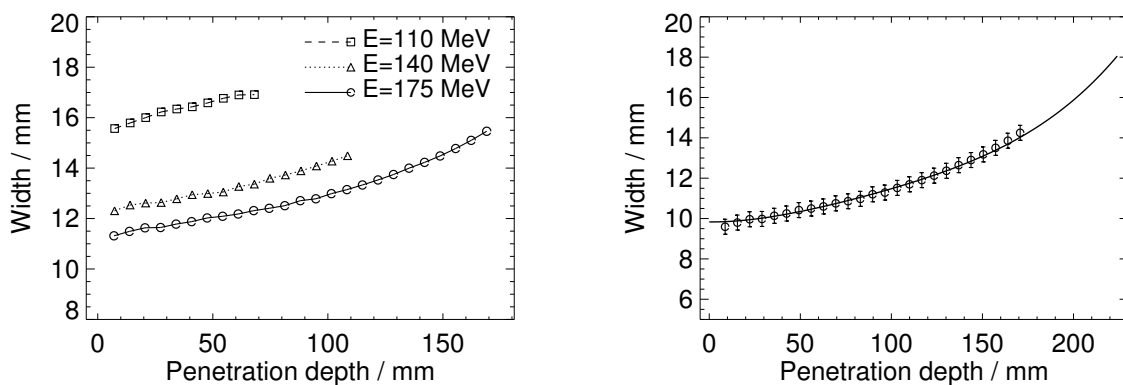
Figure 5–37: *Left: Width (FWHM) of the lateral β^+-activity profiles along the penetration depth for three proton irradiation of PMMA targets. Right: Lateral broadening of the β^+-activity induced by the 175 MeV proton beam, corrected for the system spatial resolution (points), in comparison to calculations [Hab94] of the lateral spread of an energetic proton beam (solid line).*

Figure 5–38: *PMMA phantom with air gaps for insertion of radiographic emulsions.*

the beam position for the considered irradiation from the first experimental run. The lateral broadening of the β^+-activity distribution produced by the 175 MeV proton beam was found in rather good agreement with calculations [Hab94] of the beam spread due to increasing lateral scattering along the proton penetration (figure 5–37, right). However, despite such a good correspondence a further experimental validation has been desirable due to the uncertainties in the experimental conditions (e.g. the lack of information on the real beam spot size and position) and the approximations behind the calculation from [Hab94].

In order to overcome constraints from the experimental conditions, an alternative to pure activation experiments of PMMA phantoms had to be found. The aim was to assess the spatial correlation between the lateral distribution of the proton induced positron radioactivity and the irradiation field independently on the beam quality and the limited knowledge of the beam parameters. For this purpose a special $10 \times 10 \times 27.3\,\mathrm{cm}^3$ PMMA phantom with 10 slits of 0.2 cm width at 2.5 cm separation along the long edge was designed. This geometry allows insertion of photographic emulsions (silver bromide Kodak X-Omat V films of 0.18 mm thickness in a 0.25 mm thick package) for the independent measurement of the lateral beam dimension simultaneously to the in-beam PET acquisition (figure 5–38). In the experiment mono-energetic pencil-like beams of 214.53 and 190.37 MeV initial energy were either partially or completely stopped in the stacked phantom. Details are given in table 5–12. The radiographic emulsions were removed immediately after the end of the irradiation, in order to prevent their exposure to the γ-radiation coming from the activated target as well as reduce the attenuating medium within the positron camera FOV during the remaining time of the PET measurement. Long acquisition times as well as adequate decay time between successive irradiation with the same phantom were necessary in order to gain sufficient counting statistics and limit the contamination of residual target activation in the PET images. For data analysis the films were developed shortly after exposure with the Kodak M35 machine. The optical density was read out using a FIPS Plus (PTW Freiburg) laser scanner operated at an intermediate resolution of 0.4 mm. Attenuation corrections for PET imaging were calculated on the basis of the phantom geometry, neglecting the presence of the film in the short fraction of acquisition during irradiation. The lateral width of the backprojected as well as iteratively reconstructed β^+-activity distributions was estimated in the inner part of the PMMA slabs, in order to avoid the influence from possible reconstruction artifacts in proximity of the phantom slits. Simulations were additionally performed according to the calculation models described in 5.3.2.3. Due to a lack of accurate information on the lateral dimension of the beam, the prediction was obtained for a value of 10 mm

Table 5–12: *Parameters of the irradiation (identifier, energy, number of extracted spills, total number of protons and irradiation time) and of the PET measurement (duration and amount of detected coincidences) for the experiment with the PMMA phantom stacked with X-ray films. The roman numbers distinguish successive irradiation at the same initial energy. The time difference between the start of a new irradiation and the end of the previous one within the same experimental run is additionally given by Δt_{pre}.*

ID	E / MeV	$\mathcal{T}$	N_p	t_{ir} / s	t_{mea} / s	N_{ev}	Δt_{pre} / min
(I)	214.53	10	$(4.9 \pm 0.9) \cdot 10^9$	42.59 ± 0.01	897	1255895	–
(II)	214.53	10	$(4.9 \pm 0.9) \cdot 10^9$	42.58 ± 0.01	388	1105725	14
(III)	214.53	10	$(4.9 \pm 0.9) \cdot 10^9$	42.57 ± 0.01	390	1386853	6
(IV)	214.53	10	$(4.9 \pm 0.9) \cdot 10^9$	42.57 ± 0.01	300	1360907	6
(I)	190.37	4	$(1.2 \pm 0.2) \cdot 10^9$	14.70 ± 0.01	3099	428682	–
(II)	190.37	8	$(3.0 \pm 0.4) \cdot 10^9$	32.53 ± 0.01	1498	850836	51

lateral FWHM. The necessary information on the composition and stopping properties of the photographic emulsions were taken from [ICR93] and [Ste84]. However, the insertion of the films mostly affects the particle range while playing only a minor role on the lateral spread of the beam.

The irradiation parameters were chosen in order to rule out possible influence of the dose dependent response of the films on the lateral broadening of the optical density in depth beyond the investigated effect due to the beam lateral scattering. The two beam energies allowed to acquire data at different variation of the dose exposure of the films along the penetration depth avoiding the highest dose values of the Bragg-peak (see figure 5–39). In addition, the relatively low amount (with respect to the previous phantom experiments) of protons delivered to the target was selected in order to prevent the saturation of the radiographic emulsions. Preliminary test irradiation showed only minor deviations below 6 % of the relative lateral broadening in depth of the optical density of films placed at different penetration depths (1st, 9th and 10th slit) and exposed to 2, 5 and 10 spills (i.e. to a dose varying by a maximum factor of 5) at 214.53 MeV with similar irradiation parameters as in table 5–12, respectively. Furthermore, also the experimental curves reported in [Spi01] suggest a film response still in the approximately linear regime well below saturation for the applied dose
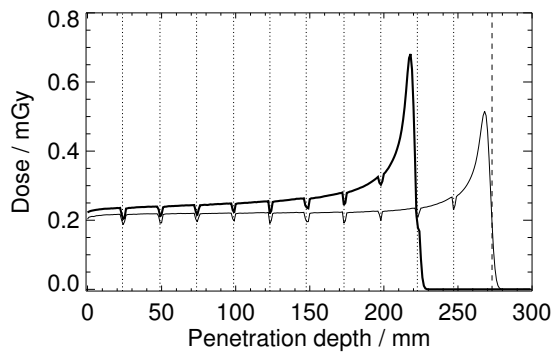

Figure 5–39: *Calculated dose depth distribution for 10^6 protons at $190.37\,MeV$ (thick line) and $214.53\,MeV$ (thin line) stopped in a thick target resembling the stacked phantom. The dotted lines mark the slit positions. The dashed line shows the exit face of the real target.*
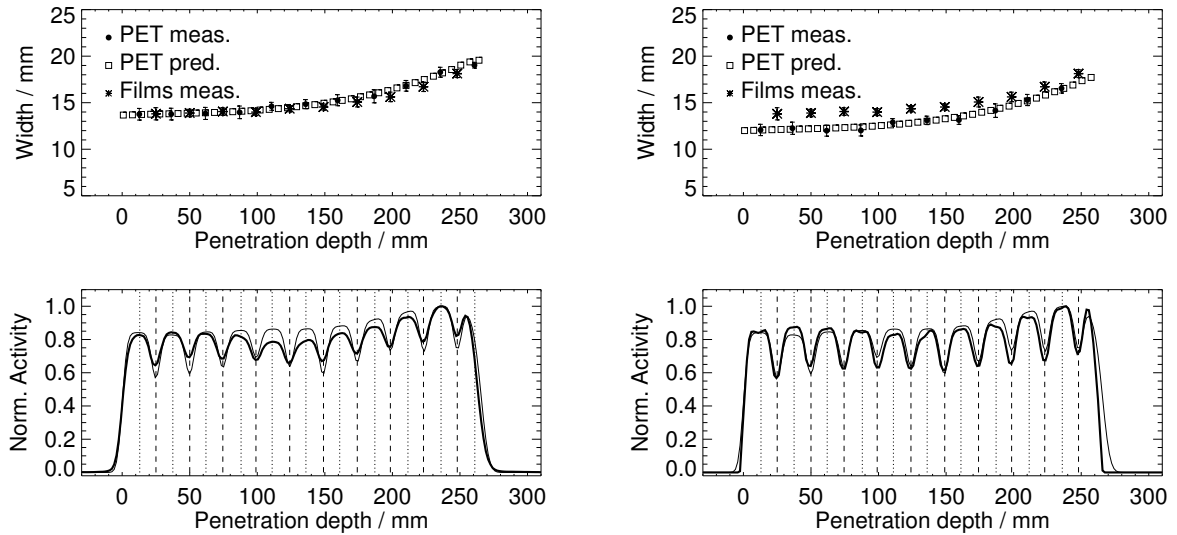
Figure 5–40: *Top: Lateral broadening (FWHM) of the measured (left: backprojection, right: iterative reconstruction) and predicted β^+-activity in comparison to the optical density of the exposed radiographic emulsions for the 214.53 MeV (I) irradiation. Bottom: Corresponding depth profiles of the measured (thick) and predicted (narrow) PET distributions. The dotted and dashed lines mark the position at which the data points (top) of the measured PET and film lateral distributions have been estimated, respectively.*

values estimated to be within $1 - 2\,\mathrm{Gy}$.

The broadening of the width (FWHM) of the measured β^+-activity and optical density lateral distributions along the penetration depth is compared in figure 5–40 and 5–41 for the 214.53 MeV (I) and 190.37 MeV (II) irradiation, respectively. It can be noticed that the average lateral width of the distributions in general differs due to the different system response, dependent on the used image reconstruction algorithm and on the dose for the PET and film measurement, respectively. Therefore, in the data analysis the broadening in
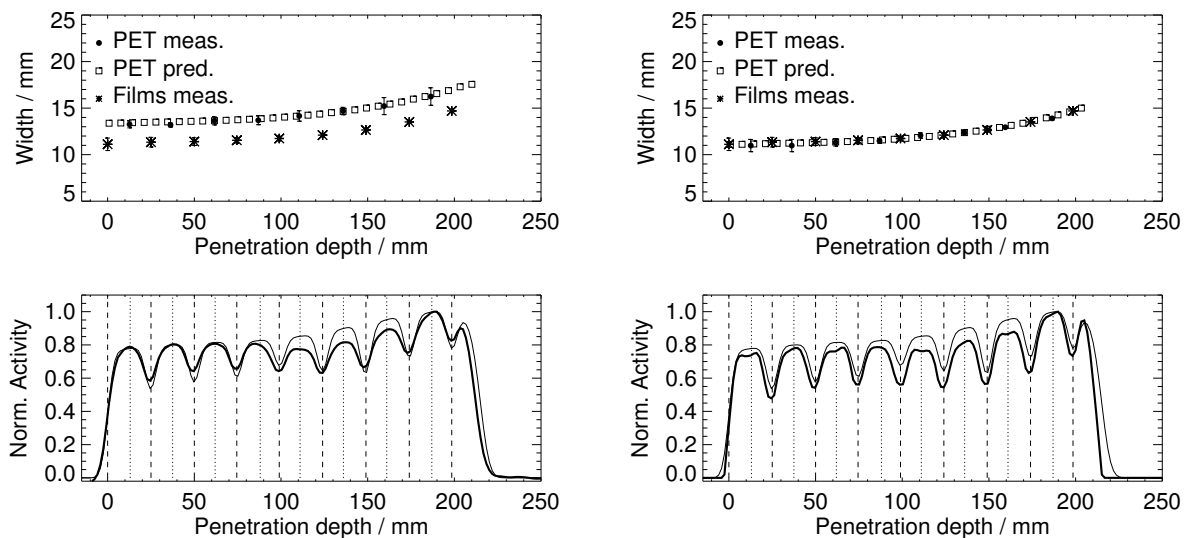
Figure 5–41: *Same comparison of figure 5–40 for the 190.37 MeV (II) irradiation. An additional film in the entrance of the phantom was used for compensation of the lower penetration of the beam in the target.*

97
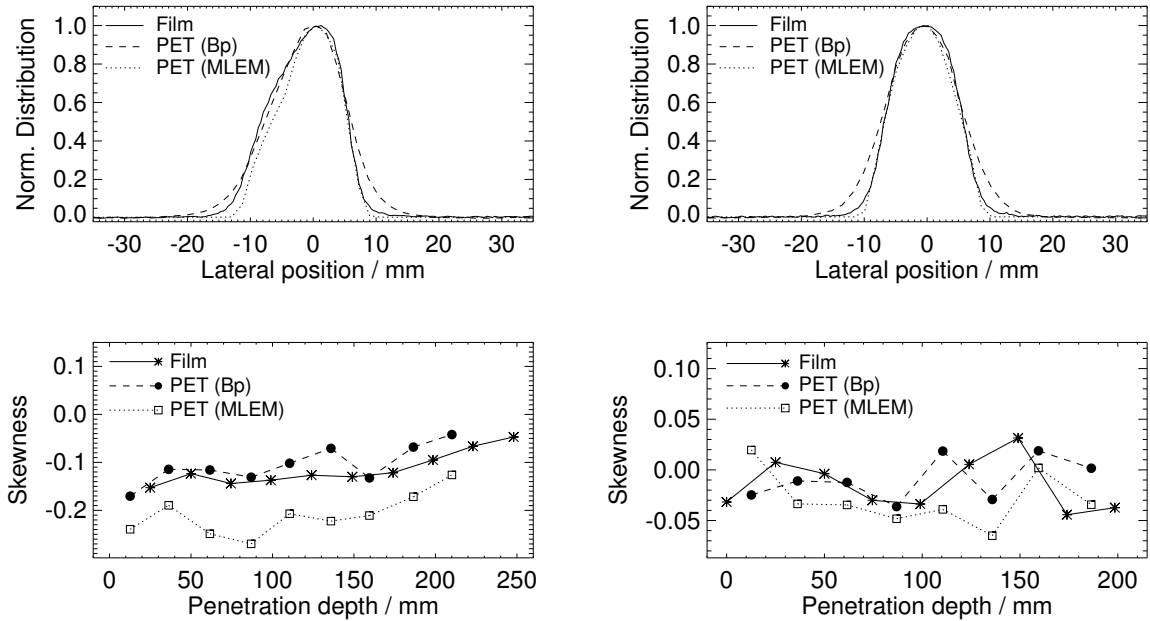
Figure 5–42: *Top: Lateral profiles of the optical density and backprojected (bp) as well as iteratively reconstructed (MLEM) positron radioactivity distributions measured at 25 and 12.5 mm penetration depth, respectively, for the 214.53 MeV (I, left) and 190.37 MeV (II, right) irradiation. Bottom: Skewness of the lateral distributions along the penetration depth for the two irradiation (cf. top).*

depth of the measured β^+-activity and optical density lateral distributions was compared after adjustement to the same mean FWHM by means of a maximum shift of about 2 mm, eliminating the constant offset due to the different response. Good agreement between PET and film measurements with maximum differences of 0.40 mm and 0.15 mm standard deviations was found for the two irradiation, respectively. The lateral spread of the measured β^+-activity was furthermore observed in good agreement with the prediction, already adjusted to the the same average FWHM of the measured activity with a maximum shift of 1.5 mm in figures 5–40 and 5–41. Differences below 0.2 mm standard deviation were observed between PET measurements and calculations.

The slightly worse experimental results for the 214.53 MeV irradiation reflect the larger uncertainties in the FWHM estimation for the asymmetric profiles originating from the suboptimal beam focussing stability in that experimental run. This is illustrated on the top of figure 5–42, showing the measured β^+-activity and optical density lateral profiles corresponding to the FWHM data points for the first PMMA slot and film slit of figure 5–40 and 5–41. The asymmetry of the beam shape in the 214.53 MeV irradiation is visible in both of the film and PET signals, the latter independently on the used reconstruction algorithm. A good correspondence was furthermore observed for the skewness of the lateral profiles along the penetration depth (figure 5–42, bottom). In summary, β^+-activity and optical density distributions as well as PET measurements and predictions were found in general good agreement with sub-millimetre standard deviations. Hence, these results strongly support the feasibility of positron emission tomography for millimetre verification of the lateral position of the irradiation field and of the dose delivery.

5.4   Conclusions

The presented feasibility study based on simulations and extensive phantom experiments carried out at GSI Darmstadt strongly supports the positive impact of in-beam PET on quality assurance of proton therapy. In comparison to carbon ion irradiation at the same range and applied physical dose an increase of the proton induced β^+-activity signal by a factor of about 3 has been quantified. This indicates the detectability of a usable signal during a therapeutic session even by an in-beam PET scanner of low detection efficiency ($< 3\%$) as the device installed at GSI. A good correspondence between measured and predicted depth and lateral β^+-activity distributions could be achieved. The lateral distribution of the proton induced β^+-activity was found in millimetre agreement with the independent film measurement of the dose lateral distribution. This suggests the reliability of PET for accurate verification of the lateral position of the irradiation field and dose delivery. The activation study of an inhomogeneous phantom has also supported the usefulness of PET for assessment of local tissue modifications or field misalignments leading to strong density gradients in the beam path during fractionated therapy. Moreover, depending on the time course of the irradiation and acquisition, in-beam PET monitoring can allow differentiation of tissues of similar density but different stoichiometry. For the most challenging issue of range monitoring, millimetre resolution has been demonstrated in mono-energetic as well as SOBP irradiation of homogeneous PMMA phantoms without and with beam scanning. However, the extension of such precision to real clinical cases requires a detailed knowledge of the tissue stoichiometry and of all reaction channels leading to the production of positron emitters. In addition, the imaging process has to be more carefully modelled, e.g. including the explicit propagation of the positrons and annihilation photons and applying the same reconstruction algorithm, for a more realistic prediction of PET images to be compared with the measured ones. The presented $^{11}C/^{15}O$ ratio analysis has also pointed out the sensitivity of the β^+-activity distal edge to the time structure of the irradiation and of the PET acquisition for accurate range monitoring. Hence, the optimum conditions minimising the unavoidable sources of uncertainties should be investigated. Such an analysis should involve the irradiation strategies especially for dynamic dose delivery systems in combination with the effects due to biological pathways washing out the produced positron emitters. The latter problem has not been addressed in the performed phantom experiments. Nevertheless, the presented results already suggest that an appropriate off-line analysis of in-beam PET acquisitions taken with tomographs of moderate spatial resolution should allow millimetre range monitoring even in clinical applications at least in regions of interest, especially for low perfused tissues.

6 Summary

The physical advantages of light ions in combination with technological advances like intensity controlled raster scanning offer a unique tool for high precision radiotherapy. This is particularly applied to delicate clinical situations of inoperable tumours growing in close proximity to critical organs. The potential benefit of such a high selectivity of ion beam therapy demands the complex and strictly conformal dose delivery to be monitored in-situ and non-invasively in three dimensions. In contrast to conventional photon radiation, light ions exhibit a well defined range which determines the position of the maximum dose delivery in the inhomogeneous tumour target. This requires a monitoring technology along the ion trajectory offering millimetre precision. Additionally, accurate control of the lateral position of the irradiation field within the patient can be a crucial issue for the frequent case of portals passing adjacent to organs at risk. At present, positron emission tomography (PET) represents the only feasible method fulfilling these requirements. For this purpose a dedicated in-beam positron camera has been completely integrated into the experimental heavy ion treatment site at the Gesellschaft für Schwerionenforschung (GSI) Darmstadt. This allows to measure the minor amount of β^+-activity produced in nuclear reactions between the projectiles and the target nuclei of the tissue simultaneously to the tumour irradiation. The emitted signal is correlated but not directly proportional to the spatial pattern of the delivered dose. Hence, therapy control is achieved by comparing the measured β^+-activity distribution with a prediction based on the treatment plan and the specific time course of the particular irradiation.

The routine monitoring of fractionated carbon ion therapy for more than 200 head and neck tumour patients treated at GSI since December 1997 has indicated the capability of the PET method *(i)* to validate the physical beam models used in treatment planning, *(ii)* to verify the whole chain from the planning to the application of the treatment independently on the beam delivery hardware and software as well as *(iii)* to detect unpredictable deviations in the maximum ion range. The reasons for the latter accidental deviations have been identified in minor positioning errors or local modifications of the patient anatomy with respect to the density information deduced from the planning X-ray computed tomograms (CT). Following the promising clinical results achieved so far at the experimental treatment facility at GSI, the in-beam PET methodology will also be established at the planned ion beam tumour therapy facility in Heidelberg, which will be capable to treat about 1000 patients per year.

This thesis has contributed to the achievement of in-beam PET as a promising clinical monitoring technique. In response to a pressing medical demand, this work has provided a tool for quantification of local dose deviations in case of observed discrepancies between the measured and expected PET images. The implemented interactive approach described in chapter 3 is in clinical use since 2001. It provides the radio-oncologist with a valuable feedback which may allow a prompt reaction in the strategy of the therapy prior to the delivery of the successive treatment fraction in case of significant deviations between planned and actually applied dose.

In order to allow an improved performance of the next generation in-beam PET scanner to be installed at the hospital-based Heidelberg facility, basic investigations on the reason for the increased noise of the PET data acquired during particle extraction from the GSI synchrotron have been carried out in this work. This problem currently prevents the use of coincidences registered during the beam bursts for image reconstruction, hence further constricting the already intrinsically extremely poor counting statistics of PET imaging for tumour therapy monitoring. The experimental investigations presented in chapter 4 show evidence that the reason is the failure of the standard random correction techniques implemented in positron emission tomographs designed for radiotracer imaging. These apply to situations where the γ-ray background can be assumed to be stationary on the microscopic time scale. However, at a particle accelerator like the

synchrotron of GSI a non-stationary background radiation caused by interactions induced by the beam has been demonstrated during particle extraction. This has been proven to be correlated in time with the measured microstructure of the extracted carbon ion beam. Hence, the results obtained in this work provide the basis for a novel data acquisition technology tailored to the non conventional application of in-beam PET imaging at accelerator facilities delivering therapeutic radiation pulsed on the sub-microsecond time scale [Eng04b], [Cre04].

Since the new generation tomograph will be implemented at a beam line capable to deliver the entire variety of ions planned at the Heidelberg facility (*p*, He, C, O), this work has finally investigated the possible extension of in-beam PET to the monitoring of the lightest and worldwide most frequently used protons. Novel information with respect to previous investigations from the literature result from *(i)* the experimental availability of the unique in-beam tomographic positron camera installed at GSI as well as *(ii)* the comparison with the already clinically implemented carbon ion case. The phantom experiments presented in chapter 5 have confirmed the predicted increase of the proton induced β^+-activity signal by a factor of about 3 with respect to carbon ion irradiation at the same range and applied dose. This proves the possible detection of a usable signal during a therapeutic proton application even by a limited angle in-beam PET scanner of low detection efficiency as the one installed at GSI. Furthermore, the increase of counting statistics is expected to improve the sensitivity of the PET method for detection and quantification of deviations between prescribed and actually delivered dose. Moreover, millimetre accuracy for verification of the lateral field position and for the most challenging issue of range monitoring has been demonstrated in non-scanned and scanned mono-energetic as well as extended spread-out Bragg-peak (SOBP) proton irradiation of polymethyl methacrylate (PMMA) targets. The additional irradiation of an inhomogeneous phantom with tissue equivalent inserts in combination with further dynamic analysis has also supported the possible extension of such millimetre precision to real clinical cases, at least in regions of interest and especially for low perfused tissues. Furthermore, the developed modelling, capable to reproduce all the experimental investigations rather well, is going to be extended to other ion species [Fie04] in order to provide a general and versatile tool for the establishment of the PET methodology at the future clinical operation of the Heidelberg facility.

References

[Aam52] R. L. Aamodt, V. Peterson and R. Phillips, $^{12}C(p,pn)^{11}C$ cross section from threshold to 340 MeV, Phys. Rev. 88 (1952) 739

[Ago03] S. Agostinelli and GEANT4 Collaboration, GEANT4 – a simulation toolkit, Nucl. Instr. Meth. A 506 (2003) 250

[Ahl80] S. P. Ahlen, Theoretical and experimental aspects of the energy loss of relativistic heavily ionizing particles, Rev. Mod. Phys. 52 (1980) 121

[Alb62] G. Albouy, J. P. Cohen, M. Gusakow, N. Poffe, H. Sergolle and L. Valentin, Spallation de l'oxygene par des protons de 20 a 150 MeV, Phys. Lett. 2 (1962) 306

[Alp98] E. L. Alpen, Radiation biophysics, Second Edition, Academic Press, San Diego - London - Boston - New York - Sidney - Tokyo - Toronto, 1998

[Ant02] L. E. Antonuk, Electronic portal imaging devices: a review and historical perspective of contemporary technologies and research, Phys. Med. Biol. 47 (2002) R31

[Bar63] W. H. Barkas, In: Nuclear Research Emulsions, Vol. I, Academic Press, New York - London, 1963, 371

[Bee03] J. Beebe-Wang, P. Vaska, F. A. Dilmanian, S. G. Peggs and D. J. Schlyer, Simulation of proton therapy treatment verification via PET imaging of induced positron emitters, Conference Records IEEE Med. Imag. Conf., Portland, OR, USA, Oct. $19 - 25$, 2003

[Bel89] M. Belli, R. Cherubini, S. Finotto, G. Moschini, O. Sapora, G. Simone and M. A. Tabocchini, RBE-LET relationship for the survival of V79 cells irradiated with low-energy protons, Int. J. Radiat. Biol. 55 (1989) 93

[Ben75] G. W. Bennett, A. C. Goldberg, G. S. Levine, J. Guthy, J. Balsamo and J. O. Archambeau, Beam localization via ^{15}O activation in proton-radiation therapy, Nucl. Instr. Meth. 125 (1975) 333

[Ben78] G. W. Bennett, J. O. Archambeau, B. E. Archambeau, J. I. Meltzer and C. L. Wingate, Visualization and transport of positron emission from proton activation in vivo, Science 200 (1978) 1151

[Bend98] B. Bendriem and D. W. Townsend (eds), The theory and practice of 3D PET, Kluwer Academic Publishers, Dordrecht - Boston - London, 1998

[Bet30] H. A. Bethe, Zur Theorie des Durchgangs schneller Korpuskularstrahlung durch Materie, Ann. Phys. 5 (1930) 325

[Betz72] H. D. Betz, Charge states and charge-changing cross sections of fast heavy ions penetrating through gaseous and solid media, Rev. Mod. Phys. 44 (1972) 465

[Bia99] M. Biaggi, F. Ballarini, W. Burkard, E. Egger, A. Ferrari and A. Ottolenghi, Physical and biophysical characteristics of a fully modulated 72 MeV therapeutic proton beam: model predictions and experimental data, Nucl. Instr. Meth. B 159 (1999) 89

[Bla94] E. A. Blakely, Current issues in low and high-LET medical radiobiology, Proc. 1st Int. Symposium on Hadrontherapy, Como, Italy, Oct. $18 - 21$, 1993, In: U. Amaldi, B. Larsson (eds), Hadrontherapy in Oncology, Excerpta Medica, Int. Congr. Series 1077, Elsevier Science 1994, 693

[Blo33] F. Bloch, *Zur Bremsung rasch bewegter Teilchen beim Durchgang durch die Materie*, Ann. Phys. 16 (1933) 285

[Boh15] N. Bohr, *The penetration of atomic particles through matter*, Phil. Mag. 30 (1915) 581

[Bra50] H. L. Bradt and B. Peters, *The heavy nuclei of the primary cosmic radiation*, Phys. Rev. 77 (1950) 54

[Brag04] W. H. Bragg and R. Kleeman, *On the ionization curves of radium*, Phil. Mag. 8 (1904) 726

[Cas86] M. E. Casey and R. Nutt, *A multicrystal two dimensional BGO detector system for positron emission tomography*, IEEE Trans. Nucl. Sci. 33 (1986) 460

[Cast94] J. R. Castro, *Heavy ion therapy: BEVALAC epoch*, Proc. 1st Int. Symposium on Hadrontherapy, Como, Italy, Oct. $18-21$, 1993, In: U. Amaldi, B. Larsson (eds), Hadrontherapy in Oncology, Excerpta Medica, Int. Congr. Series 1077, Elsevier Science 1994, 208

[Cha99a] M. B. Chadwick, P. G. Young, S. Chiba, S. Frankle, G. M. Hale, H. G. Hughes, A. J. Koning, R. C. Little, R. E. Mac Farlane, R. E. Prael and L. S. Waters, *Cross section evaluations to 150 MeV for accelerator-driven systems and implementation in MNCPX*, Nucl. Sci. Eng. 131 (1999) 293

[Cha99b] M. B. Chadwick, D. T. L. Jones, G. J. Arendse, A. A. Cowley, W. A. Richter, J. J. Lawrie, R. T. Newman, J. V. Pilcher, F. D. Smit, G. F. Steyn, J. W. Koen and J. A. Stander, *Nuclear interaction cross sections for proton radiotherapy*, Nucl. Phys. A 654 (1999) 1051c

[Che79] G. T. Y. Chen, R. P. Singh, J. R. Castro, J. T. Lyman and J. M. Quivey, *Treatment planning for heavy ion radiotherapy*, Int. J. Rad. Oncol. Biol. Phys. 5 (1979) 1809

[Cho77] Z. H. Cho and M. R. Farukhi, *Bismuth germanate as a potential scintillation detector in positron cameras*, J. Nucl. Med. 18 (1977) 840

[Chu93] W. T. Chu, B. A. Ludewigt and T. R. Renner, *Instrumentation for treatment of cancer using proton and light-ion beams*, Rev. Sci. Instrum. 64 (1993) 2055

[Cou94] G. Coutrakon, J. Hubbard, J. Johanning, G. Maudsley, T. Slaton and P. Morton, *A performance study of the Loma Linda proton medical accelerator*, Proc. 1st Int. Symposium on Hadrontherapy, Como, Italy, Oct. $18-21$, 1993, In: U. Amaldi, B. Larsson (eds), Hadrontherapy in Oncology, Excerpta Medica, Int. Congr. Series 1077, Elsevier Science 1994, 282

[Cra56] W. E. Crandall, G. P. Millburn, R. V. Pyle and W. Birnbaum, $^{12}C(x,xn)^{11}C$ and $^{27}Al(x,x2pn)^{24}Na$ cross sections at high energies, Phys. Rev. 101 (1956) 329

[Cre01a] P. Crespo, J. Debus, W. Enghardt, Th. Haberer, O. Jäkel, M. Krämer and G. Kraft for the Heavy ion Therapy Collaboration, *Tumour therapy with carbon ion beams*, Physica Medica XVII Suppl. 4 (2001) 1

[Cre01b] P. Crespo, K. Lauckner and W. Enghardt, *The combination of an in-beam PET scanner with a rotating beam delivery for ion tumour therapy*, Forschungszentrum Rossendorf, Wiss. Tech. Ber. FZR-319 (2001) 100

[Cre04] P. Crespo, T. Barthel, H. Frais-Kölbl, E. Griesmayer, K. Heidel, K. Parodi, J. Pawelke and W. Enghardt, *Suppression of random coincidences during in-beam PET measurements*, accepted for presentation at IEEE Nucl. Sci. Symp. and Med. Imag. Conf. 2004, Rome, Italy, Oct. 2004

[Cum63] J. B. Cumming, *Monitor Reactions For High Energy Proton Beams*, Ann. Rev. Nucl. Sci. 13 (1963) 261

[Deb00] J. Debus, T. Haberer, D. Schulz-Ertner, O. Jäkel, F. Wenz, W. Enghardt, W. Schlegel, G. Kraft and M. Wannenmacher, *Fractionated carbon ion irradiation of skull base tumours at GSI. First clinical results and future perspectives*, Strahlenther. Onkol. 176 (2000) 211

[Del94] A. Del Guerra, G. Di Domenico, M. Gambaccini and M. Marziani, *A Monte Carlo simulation of the possible use of positron emission tomography in proton radiotherapy*, Nucl. Instr. Meth. A 345 (1994) 379

[Eic00] H. Eickhoff, *Private communication*, GSI Darmstadt, February 2000

[Eic01] H. Eickhoff, *Private communication*, GSI Darmstadt, November 2001

[Eng99a] W. Enghardt, J. Debus, T. Haberer, B. G. Hasch, R. Hinz, O. Jäkel, M. Krämer, K. Lauckner and J. Pawelke, *The application of PET to quality assurance of heavy-ion tumor therapy*, Strahlenther. Onkol. 175 (1999) 33

[Eng99b] W. Enghardt, J. Debus, T. Haberer, B. G. Hasch, R. Hinz, O. Jäkel, M. Krämer, K. Lauckner, J. Pawelke and F. Pönisch, *Positron emission tomography for quality assurance of cancer therapy with light ion beams*, Nucl. Phys. A 654 (1999) 1047c

[Eng99c] W. Enghardt, J. Debus, T. Haberer, B. G. Hasch, R. Hinz, O. Jäkel, M. Krämer, K. Lauckner, J. Pawelke and F. Pönisch, *The routine PET monitoring of tumour therapy with ^{12}C ions*, Forschungszentrum Rossendorf, Wiss. Tech. Ber. FZR-271 (1999) 89

[Eng00] W. Enghardt, R. Hinz, K. Lauckner, J. Pawelke, F. Pönisch and B. G. Hasch, *In-situ positron emission tomography for dose localisation at the tumour therapy with ^{12}C*, GSI Scientific Report 1999, GSI 2000-1 (2000) 164

[Eng01] W. Enghardt, K. Parodi, J. Pawelke, F. Pönisch, M. Sobiella, P. Crespo, T. Haberer, C. Kausch, K. Lauckner and D. Schardt, *Positron emission tomography (PET) for ion therapy quality assurance*, GSI Scientific Report 2000, GSI 2001-1 (2001) 161

[Eng04a] W. Enghardt, P. Crespo, F. Fiedler, R. Hinz, K. Parodi, J. Pawelke and F. Pönisch, *Charged hadron tumour therapy monitoring by means of PET*, Nucl. Instr. Meth. A 525 (2004) 284

[Eng04b] W. Enghardt, P. Crespo, K. Parodi and J. Pawelke, *Verfahren zur Korrektur der beim Monitoring der strahlentherapeutischen Behandlung mittels in-beam PET erhaltenen Messwerte*, Patentanmeldung 10 2004 009 784.4, Deutsches Patentamt München, Feb. 28, 2004

[Eph67] M. Epherre and E. Gradsztajn, *Calcul de la spallation de ^{12}C et ^{16}O par des protons de 70 à 200 MeV*, J. Physique 28 (1967) 745

[Ess00] H. G. Essel and N. Kurz, *The general purpose data acquisition system MBS*, IEEE Trans. Nucl. Sci., 47 (2000) 337

[Fas01a] A. Fassò, A. Ferrari and P. R. Sala, *Electron-photon transport in FLUKA: status*, Proc. Monte Carlo 2000 Conference, Lisbon, October 23 − 26, 2000, A. Kling, F. Barao, M. Nakagawa, L. Tavora, P. Vaz (eds), Springer-Verlag, Berlin, 2001, 159

[Fas01b] A. Fassò, A. Ferrari and P. R. Sala, *FLUKA: Status and Prospective for Hadronic Applications*, Proc. Monte Carlo 2000 Conference, Lisbon, October $23-26$, 2000, A. Kling, F. Barao, M. Nakagawa, L. Tavora, P. Vaz (eds), Springer-Verlag, Berlin, 2001, 955

[Fas02] A. Fassò, A. Ferrari, J. Ranft and P. Sala, *FLUKA manual*, webpage *http://www.fluka.org*, 2002

[Fer96] A. Ferrari and P. Sala, *The physics of high energy reactions*, Proc. of the Workshop on Nuclear Reaction Data and Nuclear Reactors Physics, Design and Safety, Trieste, Italy, 15 April - 17 May, 1996

[Fer97] A. Ferrari, and P. R. Sala, *Intermediate and high energy models in FLUKA: improvements, benchmarks and applications*, Proc. Int. Conf. on Nuclear Data for Science and Technology, NDST-97, Trieste, Italy, $19-24$ May, 1997, In: G. Reffo, A. Ventura and C. Grandi (eds), Italian Phys. Soc., Bologna, Vol. 59, Part I (1997) 247

[Fie04] F. Fiedler, K. Parodi and W. Enghardt, *In-beam PET for radiotherapy with helium beams: model predictions*, Forschungszentrum Rossendorf, Wiss. Tech. Ber. FZR-401 (2004) 68

[For98] P. Forck, A. Peters, T. Hoffmann, U. Meyer, H. Reeg and W. Vodel, *Micro-structure of resonant extracted SIS-beams*, GSI Scientific Report 1997, GSI 98-1 (1998) 166

[Gad94] G. Gademann, *Socioeconomic aspects of hadrontherapy*, Proc. 1st Int. Symposium on Hadrontherapy, Como, Italy, October $18-21$, 1993, In: U. Amaldi, B. Larsson (eds), Hadrontherapy in Oncology, Excerpta Medica, Int. Congr. Series 1077, Elsevier Science 1994, 59

[Gre75] D. E. Greiner, P. J. Lindstrom, H. H. Heckman, B. Cork and F. S. Bieser, *Momentum distributions of isotopes produced by fragmentation of relativistic ^{12}C and ^{16}O projectiles*, Phys. Rev. Lett. 35 (1975) 152

[Gro98] K. D. Gross and M. Pavlovic (eds), *Proposal for a dedicated ion beam facility for cancer therapy*, GSI Darmstadt, 1998

[Gun04] K. Gunzert-Marx, *Nachweis leichter Fragmente aus Schwerionenreaktionen mit einem BaF_2-Teleskop-Detektor*, Ph.D. Thesis, Darmstadt University of Technology, GSI Diss. 2004-02, 2004

[Hab93] Th. Haberer, W. Becher, D. Schardt and G. Kraft, *Magnetic scanning system for heavy ion therapy*, Nucl. Instr. Meth. A 330 (1993) 296

[Hab94] Th. Haberer, *Entwicklung eines magnetischen Strahlführungssystems zur tumorkonformen Strahlentherapie mit schweren geladenen Teilchen*, Ph.D. Thesis, GSI Report 94-09, 1994

[Hab00] Th. Haberer, *Private communication*, GSI Darmstadt, September 2000

[Hal94] E. J. Hall, *Radiobiology for the radiologist*, J. P. Lipincott Company, 1994

[Han81] K. M. Hanson, J. N. Bradbury, T. M. Cannon, R. L. Hutson, D. B. Laubacher, R. J. Macek, M. A. Paciotti and C. A. Taylor, *Computed tomography using proton energy loss*, Phys. Med. Biol. 26 (1981) 965

[Has96] B. G. Hasch, *Die physikalischen Grundlagen einer Verifikation des Bestrahlungsplanes in der Schwerionen-Tumortherapie mit der Positronen-Emissions-Tomographie*, Ph.D. Thesis, Dresden University of Technology, 1996

[Hau79] P. Hautojärvi, *Positrons in solids, topics in current physics*, Springer-Verlag, Heidelberg, Vol. 12, 1979

[Hee99] P. Heeg, G. Hartmann, O. Jäkel, C. Karger and G. Kraft, *Quality assurance at the heavy-ion therapy facility at GSI*, Strahlenther. Onkol. 175 (1999) 36

[Hig75] V. L. Highland, *Some practical remarks on nuclear scattering*, Nucl. Instr. Meth. 129 (1975) 497. Erratum appeared in Nucl. Instr. Meth. 161 (1979) 171

[Hin52] N. M. Hintz and N. F. Ramsey, *Excitation functions to 100 MeV*, Phys. Rev. 88 (1952) 19

[Hinz00] R. Hinz, *Beiträge zur Einführung der Positronen-Emissions-Tomographie bei der Schwerionen-Tumortherapie*, Dr.-Ing. Thesis, Dresden University of Technology, 2000

[Hinz03] R. Hinz, *Private communication*, Hammersmith Hospital, London, 2003

[Hüf85] J. Hüfner, *Heavy fragments produced in proton-nucleus and nucleus-nucleus collisions at relativistic energies*, Phys. Rep. 125 (1985) 129

[IAE97] International Atomic Energy Agency, *Development of reference charged-particle cross sections data for medical radioisotope production*, INDC(NDS)-371, Summary Report of IAEA Research Coordination Meeting, Cape Town, South Africa, April 7 − 10, 1997

[ICR93] International Commission on Radiation Units and Measurements ICRU, *Stopping powers and ranges for protons and alpha particles*, Report 49, May 1993

[ICR00] International Commission on Radiation Units and Measurements ICRU, *Nuclear data for neutron and proton radiotherapy and for radiation protection*, Report 63, March 2000

[Ilj91] A. S. Iljinov, V. G. Semenov, M. P. Semenova, N. M. Sobolevsky, and L. V. Udovenko, *Production of radionuclides at intermediate energies*, Landolt-Börnstein, Springer-Verlag New Series, Vol. 13a, 1991

[Jaf02] D. A. Jaffray, J. H. Siewerdsen, J. W. Wong and A. A. Martinez, *Flat-panel cone-beam computed tomography for image-guided radiation therapy*, Int. J. Radiat. Oncol. Biol. Phys., 53 (2002) 1337

[Jäk01a] O. Jäkel, C. Jakob, D. Schardt, C. P. Karger and G. H. Hartmann, *Relation between carbon ion ranges and X-ray CT numbers*, Med. Phys. 28 (2001) 701

[Jäk01b] O. Jäkel, M. Krämer, C. P. Karger and J. Debus, *Treatment planning for heavy ion radiotherapy: clinical implementation and application*, Phys. Med. Biol. 46 (2001) 1101

[Jon86] W. F. Jones, M. E. Casey, L. G. Byars and S. G. Burgiss, *A VMEBUS based, real time sorter design for positron emission tomography*, IEEE Trans. Nucl. Sci. 33 (1986) 601

[Kan99] T. Kanai, M. Endo, S. Minohara, N. Miyahara, H. Koyama-ito, H. Tomura, N. Matsufuji, Y. Futami, A. Fukumura, T. Hiraoka, Y. Furusawa, K. Ando, M. Suzuki, F. Soga and K. Kawachi, *Biophysical characteristics of HIMAC clinical irradiation system for heavy-ion radiation therapy*, Int. J. Rad. Oncol. Biol. Phys. 44 (1999) 201

[Kana02] M. Kanazawa, A. Kitagawa, S. Kouda, T. Nishio, M. Torikoshi, K. Noda, T. Murakami, M. Suda, T. Tomitani, T. Kanai, Y. Futami, M. Shinbo, E. Urakabe and Y. Iseki, *Application of an RI-beam for cancer therapy: in-vivo verification of the ion-beam range by means of positron imaging*, Nucl. Phys. A 701 (2002) 244c

[Kar99] C. P. Karger, O. Jäkel and G. H. Hartmann, *A system for three-dimensional dosimetric verification of treatment plans in intensity-modulated radiotherapy with heavy ions*, Med. Phys. 26 (1999) 2125

[Kar02] C. P. Karger, O. Jäkel, P. Heeg and G. H. Hartmann, *Klinische Dosimetrie für schwere geladene Teilchen*, Z. Med. Phys. 12 (2002) 159

[Kau02] C. Kausch and W. Enghardt, *The evaluation of carbon ion therapy PET data within the time domain*, Forschungszentrum Rossendorf, Wiss. Tech. Ber. FZR-341 (2002) 102

[Kit90] S. W. Kitwanga, P. Leleux, P. Lipnik and J. Vanhorenbeeck, *Production of $^{14,15}O$, ^{18}F, and ^{19}Ne radioactive nuclei from (p,n) reactions up to 30 MeV*, Phys. Rev. C 42 (1990) 748

[Kou82] K. Kouris, N. M. Spyrou and D. F. Jackson, *Imaging with ionizing radiations*, Surrey University Press, Glasgow, 1982

[Kra97] G. Kraft, *Radiobiology of heavy charged particles*, In: U. Amaldi, B. Larsson and Y. Lemoigne (eds), Advances in Hadrontherapy, Excerpta Medica, Int. Congr. Series 1144, Elsevier 1997, 385

[Kra99] G. Kraft, *RBE and its interpretation*, Strahlenther. Onkol. 175 (1999) 44

[Kra00] G. Kraft, *Tumour therapy with heavy charged particles*, Prog. Part. Nucl. Phys. 45 (2000) 473

[Krä00a] M. Krämer, O. Jäkel, T. Haberer, G. Kraft, D. Schardt and U. Weber, *Treatment planning for heavy-ion radiotherapy: physical beam model and dose optimization*, Phys. Med. Biol. 45 (2000) 3299

[Krä00b] M. Krämer and M. Scholz, *Treatment planning for heavy-ion radiotherapy; calculation and optimization of biologically effective dose*, Phys. Med. Biol. 45 (2000) 3319

[Lai96] R. F. Laitano, M. Rosetti and M. Frisoni, *Effects of nuclear interactions on energy and stopping power in proton beam dosimetry*, Nucl. Instr. Meth. A 376 (1996) 466

[Lau99] K. Lauckner, *Entwicklung eines iterativen 3D Rekonstruktionsverfahrens für die Kontrolle der Tumorbehandlung mit Schwerionen mittels der Positronen-Emissions-Tomographie*, Dr.-Ing. Thesis, Dresden University of Technology, 1999

[Leo87] W. R. Leo, *Techniques for nuclear and particle physics experiments*, Springer-Verlag, Berlin, 1987

[Lin95] U. Linz, *Physical and biological rationale for using ions in therapy*, In: U. Linz (ed.), Ion Beams in Tumour Therapy, Chapman & Hall, London - Glasgow - Weinheim - New York - Tokyo - Melbourne - Madras, 1995, 15

[Lit93] D. W. Litzenberg, J. F. Bajema, F. D. Becchetti, J. A. Brown, R. S. Raymond, D. A. Roberts, J. Caraher, G. Hutchins, R. Ronningen, R. Smith and M. Abbott, *On-line monitoring and P.E.T. imaging of proton radiotherapy beams*, IEEE Trans. Nucl. Sci. 40 (1993) 954

[Lit99] D. W. Litzenberg, D. A. Roberts, M. Y. Lee, K. Pham, A. M. Vander Molen, R. Ronningen and F. D. Becchetti, *On-line monitoring of radiotherapy beams: experimental results with proton beams*, Med. Phys. 26 (1999) 992

[Lla84] J. Llacer, A. Chatterjee, E. L. Alpen, W. Saunders, S. Andreae and H. C. Jackson, *Imaging by injection of accelerated radioactive particle beams*, IEEE Trans. Med. Imag. 3 (1984) 80

[Lla88] J. Llacer, *Positron emission medical measurements with accelerated radioactive ion beams*, Nucl. Sci. Appl. 3 (1988) 111

[Mea66] D. F. Measday, *The $^{12}C(p,pn)^{11}C$ Reaction from 50 to 160 MeV*, Nucl. Phys. 78 (1966) 476

[Med97] J. Medin and P. Andreo, *Monte Carlo calculated stopping-power ratios, water/air, for clinical proton dosimetry (50 – 250 MeV)*, Phys. Med. Biol. 42 (1997) 89

[Mof75] D. R. Mofett, E. P. Colton, G. A. Concaildi, E. W. Hoffman, R. D. Klem, M. J. Knott, S. L. Kramer, R. L. Martin, E. F. Parker, A. R. Passi, P. F. Schultz, R. L. Stockley, R. E. Timm, L. S. Skaggs and V. W. Steward, *Initial test of a proton radiographic system*, IEEE Trans. Nucl. Sci. 22 (1975) 1749

[Mol48] G. Z. Molière, *Theorie der Streuung schneller geladener Teilchen. II. Mehrfach- und Vielfachstreuung*, Z. Naturforsch. 3a (1948) 78

[Mor00] P. Moritz, *Private Communication*, GSI Darmstadt, December 2000

[Nau03] J. Naumann, *Private Communication*, GSI Darmstadt, 2003

[New89] D. F. Newport, H. M. Dent, M. E. Casey and D. W. Bouldin, *Coincidence detection and selection in positron emission tomography using VLSI*, IEEE. Trans. Nucl. Sci. 36 (1989) 1052

[Nuc00] Nuclear Reaction Data Center network which is coordinated by the IAEA Nuclear Data Section, 2000, webpage *http://www.nndc.bnl.gov/nndc/exfor/*

[Oel96] U. Oelfke, G. K. Y. Lam and M. S. Atkins, *Proton dose monitoring with PET: quantitative studies in lucite*, Phys. Med. Biol. 41 (1996) 177

[Ols83] D. L. Olson, B. L. Berman, D. E. Greiner, H. H. Heckman, P. J. Lindstrom and H. J. Crawford, *Factorization of fragment-production cross sections in relativistic heavy-ion collisions*, Phys. Rev. C 28 (1983) 1602

[Ose65] B. E. Oser (ed.), *Hawks physiological chemistry*, McGraw-Hill, New York, 1965

[Paa93] A. M. J. Paans and J. M. Schippers, *Proton therapy in combination with PET as monitor: a feasibility study*, IEEE Trans. Nucl. Sci. 40 (1993) 1041

[Pag02] H. Paganetti, *Nuclear interactions in proton therapy: dose and relative biological effect distributions originating from primary and secondary particles*, Phys. Med. Biol. 47 (2002) 747

[Par00] K. Parodi and W. Enghardt, *Potential application of PET in quality assurance of proton therapy*, Phys. Med. Biol. 45 (2000) N151

[Par02] K. Parodi, W. Enghardt and T. Haberer, *In-beam PET measurements of β^+-radioactivity induced by proton beams*, Phys. Med. Biol. 47 (2002) 21

[Paw95] J. Pawelke, *Methodische Untersuchungen zum Einsatz der Positronen-Emissions-Tomographie in der Leichtionen-Tumortherapie*, Ph.D. Thesis, Dresden University of Technology, 1995

[Paw96] J. Pawelke, L. Byars, W. Enghardt, W. D. Fromm, H. Geissel, B. G. Hasch, K. Lauckner, P. Manfraß, D. Schardt and M. Sobiella, *The investigation of different cameras for in-beam PET imaging*, Phys. Med. Biol. 41 (1996) 279

[Paw97] J. Pawelke, W. Enghardt, Th. Haberer, B. G. Hasch, R. Hinz, M. Krämer, K. Lauckner and M. Sobiella, *In-beam PET imaging for the control of heavy-ion tumour therapy*, IEEE Trans. Nucl. Sci. 44 (1997) 1492

[Ped95] E. Pedroni, R. Bacher, H. Blattmann, T. Böhringer, A. Coray, A. Lomax, S. Lin, G. Munkel, S. Scheib, U. Schneider and A. Tourovsky, *The 200 MeV proton therapy project at the Paul Scherrer Institute: Conceptual design and practical realisation*, Med. Phys. 22 (1995) 37

[Pön99] F. Pönisch, W. Enghardt, R. Hinz, O. Jäkel and K. Lauckner, *The evaluation of PET-images obtained during ^{12}C radiotherapy*, Forschungszentrum Rossendorf, Wiss. Tech. Ber. FZR-271 (1999) 91

[Pön03a] F. Pönisch, *Optimierung der Positronen-Emissionen-Tomographie bei der Schwerionentherapie auf der Basis von Röntgentomogrammen*, Ph.D. Thesis, Dresden University of Technology, 2003

[Pön03b] F. Pönisch, W. Enghardt and K. Lauckner, *Attenuation and scatter correction for in-beam positron emission tomography monitoring of tumour irradiations with heavy ions*, Phys. Med. Biol. 48 (2003) 2419

[Rud66] G. Rudstam, *Systematics of spallation yields*, Z. Naturforsch. 21a (1966) 1027

[Saj85] M. Sajjad, R. M. Lambrecht and A. P. Wolf, *Cyclotron isotopes and radiopharmaceuticals. Investigation of some excitation functions for the preparation of ^{15}O, ^{13}N and ^{11}C*, Radiochim. Act. 38 (1985) 57

[Sch96] W. H. Scharf and O. A. Chomicki, *Medical accelerators in radiotherapy: past, present and future*, Physica Medica XII (1996) 199

[Scha98] B. Schaffner and E. Pedroni, *The precision of proton range calculations in proton radiotherapy treatment planning: experimental verification of the relation between CT-HU and proton stopping power*, Phys. Med. Biol. 43 (1998) 1579

[Schar01] D. Schardt, *Private communication*, GSI Darmstadt, December 2001

[She82] L. A. Shepp and Y. Vardi, *Maximum likelihood reconstruction for emission tomography*, IEEE Trans. Med. Imag. 1 (1982) 113

[Schn95] U. Schneider and E. Pedroni, *Proton radiography as a tool for quality control in proton therapy*, Med. Phys. 22 (1995) 353

[Schn00] W. Schneider, T. Bortfeld and W. Schlegel, *Correlation between CT numbers and tissue parameters needed for Monte Carlo simulations of clinical dose distributions*, Phys. Med. Biol. 45 (2000) 459

[Schw91] T. Schwab, *Transport von Schwerionen durch Materie innerhalb ionenoptischer Systeme*, Ph.D. Thesis, GSI Report 91-10, 1991

[Sih93] L. Sihver, C. H. Tsao, R. Silberberg, T. Kanai and A. F. Barghouty, *Total reaction and partial cross section calculation in proton-nucleus ($Z_t \leq 26$) and nucleus-nucleus reactions (Z_p and $Z_t \leq 26$)*, Phys. Rev. C 47 (1993) 1225

[Sil73] R. Silberberg and C. H. Tsao, *Partial cross-sections in high-energy nuclear reactions and astrophysical applications*, Astrophys. J. Suppl. 25 (1973) 315

[Sil98] R. Silberberg, C. H. Tsao and F. Barghouty, *Updated partial cross sections of proton-nucleus reactions*, Astrophys. J. 501 (1998) 911

[Sis01] J. Sisterson, *A Newsletter for those interested in proton, light ion and heavy charged particle radio-therapy*, Particles 28 (2001) 12

[Spi01] B. Spielberger, M. Scholz, M. Krämer and G. Kraft, *Experimental investigations of the response of films to heavy-ion irradiation*, Phys. Med. Biol. 46 (2001) 2889

[Ste84] R. M. Sternheimer, M. J. Berger and S. M. Seltzer, *Density effect for the ionization loss of charged particles in various substances*, Atomic Data and Nuclear Data Tables 30 (1984) 261

[Tob58] C. A. Tobias, J. H. Lawrence, J. L. Born, R. McCombs, J. E. Roberts, H. O. Anger, B. V. A. Low-Beer and C. Huggins, *Pituitary irradiation with high-energy proton beams; a preliminary report*, Cancer Res. 18 (1958) 121

[Tob71] C. A. Tobias, A. Chatterjee and A. R. Smith, *Radioactive fragmentation of N^{7+} ion beam observed in a beryllium target*, Phys. Lett. 37A (1971) 119

[Tob77] C. A. Tobias, E. V. Benton, M. P. Capp, A. Chatterjee, M. R. Cruty and R. P. Henke, *Particle radiography and autoactivation*, Int. J. Rad. Oncol. Biol. Phys. 3 (1977) 35

[Tom94] T. Tomitani, K. Yoshikawa, M. Kanazawa, Y. Wada and T. Kanai, *Preliminary measurements of autoactivation of ^{12}C beams with a commercially available PET*, in T. Kanai and E. Takada (eds), Proc. of NIRS International Seminar on the Application of Heavy Ion Accelerator to Radiation Therapy of Cancer in connection with XXI PTCOG Meeting, November $14 - 16$, 1994, NIRS-M-103 / HIMAC-008 (1994) 125

[Tom97] T. Tomitani, M. Kanazawa, K. Yoshikawa, T. Kanai, A. Fukumura, Y. Wada and I. Shinoda, *Effect of target fragmentation on the imaging of autoactivation of heavy ions*, J. Jpn. Soc. Ther. Radiol. Oncol., Vol. 9, Suppl. 2 and Proc. of the XXVII PTCOG Meeting (1997) 79

[Tsa98] C. H. Tsao, R. Silberberg and A. F. Barghouty, *Partial cross sections of nucleus-nucleus reactions*, Astrophys. J. 501 (1998) 920

[Val65] L. Valentin, *Reactions (p,n) et (p,pn) induites à moyenne énergie sur des noyaux légers*, Nucl. Phys. 62 (1965) 81

[Ver94] A. J. M. Vermoken and F. A. J. M. Schermer (eds), *Towards Coordination of Cancer Research in Europe*, Vol. 5 of Biomedical and Health Research, Amsterdam - Oxford - Washington DC - Tokyo, IOS PRESS, 1994

[Vos98] B. Voss, H. Junk and H. Stelzer, *The monitor system of the therapy project*, GSI Scientific Report 1997, GSI 1998-01 (1998) 187

[Vyn93] S. Vynckier, S. Derreumaux, F. Richard, A. Bol, C. Michel and A. Wambersie, *Is it possible to verify directly a proton-treatment plan using positron emission tomography?*, Radiother. Oncol. 26 (1993) 275

[Wam89] A. Wambersie, *The Future of high-LET radiation in cancer therapy*, In: P. Chauvel and A. Wambersie, Eulima Workshop on the potential value of light ion beam therapy, Pub. n. EUR 12165, Commission of the European Community, Brussels, 1989

[Wam99] A. Wambersie, *Reference RBE and clinical RBE: applications of these concepts in hadron therapy*, Strahlenther. Onkol. 175 (1999) 39

[Web01] S. Webb, *Intensity-Modulated Radiation Therapy*, Institute of Physics Publishing, Bristol, 2001

[Wie89] W. Wienhard, R. Wagner and W.-D. Heiss, *PET, Grundlagen und Andwendungen der Positronen-Emissions-Tomographie*, Springer-Verlag, Berlin, 1989

[Wil46] R. R. Wilson, *Radiological use of fast protons*, Radiol. 47 (1946) 487

[Yam01] S. Yamada, *The progress of HIMAC and particle therapy facilities in Japan*, Proc. of the Second Asian Particle Accelerator Conference, Beijing, China, 2001, 829

[You92] P. G. Young, E. D. Arthur and M. B. Chadwick, *Comprehensive nuclear model calculations: introduction to the theory and use of the GNASH code*, Technical Report LA-12343-MS, Los Alamos National Laboratory, NM, 1992

A Table of abbreviations

1D, 2D and 3D	:	One-, two- and three-**d**imensional
ADC	:	**A**nalog to **d**igital **c**onverter
AP	:	**A**ntero-**p**osterior
ATIMA	:	**At**omic **i**nteraction with **ma**tter (computer code)
BGO	:	Bismuth Germanate (**Bi**$_4$**Ge**$_3$**O**$_{12}$)
CAMAC	:	**C**omputer **a**ided **m**easurement **a**nd **c**ontrol
CERN	:	**C**onseil **E**uropéen pour la **R**echerche **N**ucléaire (Geneva, Switzerland)
CFD	:	**C**onstant **f**raction **d**iscriminator
CPU	:	**C**entral **p**rocessing **u**nit
CT	:	**C**omputerised **t**omography
CTI	:	**C**omputer **T**echnology **I**nc., Knoxville (USA)
D	:	**D**elayed coincidence
DB	:	**D**ata**b**ase
DKFZ	:	**D**eutsches **K**rebs**f**orschungs**z**entrum (Heidelberg, Germany)
DNA	:	**D**eoxyribo**n**ucleic **a**cid
DSO	:	**D**igital **s**torage **o**scillograph
ENLIGHT	:	**E**uropean **N**etwork for research in **Ligh**t ion **T**herapy
ESTRO	:	**E**uropean **S**ociety for **T**herapeutic **R**adiology and **O**ncology
FLUKA	:	**Flu**ktuierende **Ka**skade (particle physics Monte Carlo code)
FOV	:	**F**ield **o**f **v**iew
FWHM	:	**F**ull **w**idth at **h**alf **m**aximum
FZR	:	**F**orschungs**z**entrum **R**ossendorf, Dresden (Germany)
GSI	:	**G**esellschaft für **S**chwer**i**onenforschung Darmstadt (Germany)
GSO	:	Gadolinium Ortho-Silicate (**G**d$_2$**SiO**$_5$:Ce)
HCL	:	**H**arvard **C**yclotron **L**aboratory (USA)
HIMAC	:	**H**eavy **I**on **M**edical **A**ccelerator in **C**hiba (Japan)
HU	:	**H**ounsfield **u**nit
ICRU	:	**I**nternational **C**ommission on **R**adiation **U**nits and Measurements
IDL	:	**I**nteractive **D**ata **L**anguage
IMRT	:	**I**ntensity **m**odulated **r**adiotherapy
INC	:	**I**ntra-**n**uclear **c**ascade
LBL	:	**L**awrence **B**erkeley **L**aboratory (USA)
LLUMC	:	**L**oma **L**inda **U**niversity **M**edical **C**enter (USA)
LOR	:	**L**ine **o**f **r**esponse
MLEM	:	**M**aximum **L**ikelihood **e**stimation **m**aximisation
NIM	:	**N**uclear **i**nstrument **m**odule
NRDC	:	**N**uclear **R**eaction **D**ata **C**enter network
P	:	**P**rompt coincidence
PE	:	**P**oly**e**thylene (C$_2$H$_4$)$_n$
PET	:	**P**ositron **e**mission **t**omography
PMMA	:	**P**oly**m**ethyl **m**eth**a**crylate (C$_5$H$_8$O$_2$)$_n$
PMT	:	**P**hoto**m**ultiplier **t**ube
PSI	:	**P**aul **S**cherrer **I**nstitut (Switzerland)

R	:	**R**andom coincidence
RF	:	**R**adio**f**requency
ROI	:	**R**egion **o**f **i**nterest
SIS	:	**S**chwer**i**onen**s**ynchrotron at GSI Darmstadt
SOBP	:	**S**pread-**o**ut **B**ragg-**p**eak
T	:	**T**rue coincidence
TAC	:	**T**ime to **a**mplitude **c**onverter
TP	:	**T**reatment **P**lanning, **T**reatment **P**lan
TRiP	:	**TR**eatment plann**i**ng for **P**articles (computer code)

Versicherung

Hiermit versichere ich, dass ich die vorliegende Arbeit ohne unzulässige Hilfe Dritter und ohne Benutzung anderer als der angegebenen Hilfsmittel angefertigt habe; die aus fremden Quellen direkt oder indirekt übernommenen Gedanken sind als solche kenntlich gemacht. Die Arbeit wurde bisher weder in Inland noch im Ausland in gleicher oder ähnlicher Form einer anderen Prüfungsbehörde vorgelegt.

Dresden, den 06.07.2004

Erklärung

Die vorliegende Arbeit wurde am Institut für Kern- und Hadronenphysik des Forschungszentrum Rossendorf e.V. (FZR) angefertigt. Die wissenschaftliche Betreuung erfolgte durch Herrn Prof. Dr. E. Grosse seitens der Fachrichtung Physik der Technischen Universität Dresden und durch Herrn Dr. rer. nat. W. Enghardt seitens der Abteilung Strahlungsphysik des Institutes für Kern- und Hadronenphysik des FZR.
Die Promotionsordnung der Fakultät für Mathematik und Naturwissenschaften der Technischen Universität Dresden wird von mir anerkannt.

Dresden, den 06.07.2004

Acknowledgements